# Study of the Rare Hadronic Decays $D_s^\pm \to K^\pm\pi^0$, $D_s^\pm \to \pi^\pm K_S^0$ and $D_s^\pm \to \pi^\pm\pi^0$ at *BABAR*

Michael Borivoje Nikolich

Imperial College London.

A thesis to be submitted for the degree of
Doctor of Philosophy
of The University of London
and the Diploma of Imperial College.

December, 2005

# Abstract

$D_s$ mesons are fully reconstructed from four final states using approximately 229 fb$^{-1}$ of data delivered by the PEP-II $e^+e^-$ collider and collected by the *BABAR* experiment at the Stanford Linear Accelerator Centre during the period 1999 to 2004.

Measurements of the exclusive branching fractions (averaged over charge-conjugate decays), $\mathcal{B}$, of the decays $D_s^+ \to K^+\pi^0$, $D_s^+ \to \pi^+K^0$ and $D_s^+ \to \pi^+\pi^0$ relative to the reference mode $D_s^+ \to K^+\overline{K}^0$ are presented:

$$\frac{\mathcal{B}(D_s^+ \to K^+\pi^0)}{\mathcal{B}(D_s^+ \to K^+\overline{K}^0)} = (2.54 \pm 0.20\ (Stat.) \pm 0.14\ (Syst.)) \times 10^{-2}$$

$$\frac{\mathcal{B}(D_s^+ \to \pi^+K^0)}{\mathcal{B}(D_s^+ \to K^+\overline{K}^0)} = (8.28 \pm 0.38\ (Stat.) \pm 0.32\ (Syst.)) \times 10^{-2}$$

$$\frac{\mathcal{B}(D_s^+ \to \pi^+\pi^0)}{\mathcal{B}(D_s^+ \to K^+\overline{K}^0)} = (-0.25 \pm 0.24\ (Stat.) \pm 0.05\ (Syst.)) \times 10^{-2}$$

In the case of $D_s^+ \to \pi^+\pi^0$ where no signal is observed an upper limit on the branching ratio, with 90% confidence and a sensitivity of $0.32 \times 10^{-2}$, is obtained:

$$\frac{\mathcal{B}(D_s^+ \to \pi^+\pi^0)}{\mathcal{B}(D_s^+ \to K^+\overline{K}^0)} < 0.38 \times 10^{-2}$$

# Acknowledgements

So many people have contributed immensely to my life and work during the course of the past three years and I would like to take this opportunity to thank them.

Firstly, I cannot thank Paul Dauncey enough for all his excellent advice during the PhD. I could not have asked for a better supervisor.

I must also thank Dan Bowerman, for his advice, friendship and introducing me to life in Palo Alto.

Thanks also to Paul Dauncey, Julia Sedgbeer and Peter Dornan for giving me the opportunity to study at Imperial College.

I acknowledge PPARC for funding this research.

My time at IC and SLAC has been made all the more enjoyable by the friends I have made:

- Jamie, Ivo, Will, Wah, Rob, Gary and Geoff for all the excellent office banter,
- Ed, Ian, Steve, Jim, Dave, Carlos, Ally, Mitch, Matt and Paul for many memorable nights out in California,
- Tim and Phil for all their shenanigans.

Finally, and above all, I would like to thank and dedicate this thesis to Ruth for her endless love and support throughout this experience.

# Declaration

The physics analysis presented in chapters 3, 4 and 5 of this thesis was developed primarily by the author with help and advice from Daniel Bowerman, Paul Dauncey and the *BABAR* Charm Analysis Working Group.

The description of the *BABAR* detector in chapter 2 represents a combination of the author's knowledge acquired over a period of three years and the work of the various *BABAR* sub-detector working groups. All plots presented in this chapter have been produced by the relevant sub-detector working groups and not the author.

Throughout this document the author refers the reader to the relevant literature wherever work is described that was not carried out by the author. In particular it should be made clear that the author played no part in determining the systematic errors described in sections 4.7.3, 4.7.4 and 4.7.5.

# Contents

# List of Figures

# List of Tables

# Chapter 1

# Theoretical Background

## 1.1 Overview

The chapter begins with a description of the Standard Model of particle physics, with emphasis on the theoretical foundations used to formulate it. The analysis presented in this thesis is concerned with processes involving weak vertices, therefore a brief description of the weak interaction follows.

A discussion of charmed meson decays presents the difficulties concerning purely hadronic decays of heavy flavour mesons and concludes with a theoretical introduction to the physical processes of relevance to this thesis. This is followed by the most recent theoretical predictions for these processes and a brief summary of their current experimental status.

Finally, the production mechanisms of $D_s^*$ mesons at the *BABAR* experiment are outlined together with the decay characteristics of such mesons. The conclusions here lead to the introduction of a reference decay mode.

**Table** 1.1: Some properties of the fundamental forces in the Standard Model.

| Force | Mediator | Typical decay lifetime / s | Range / m |
|---|---|---|---|
| Strong nuclear | gluon | $10^{-23}$ | $\leqslant 10^{-15}$ |
| Weak nuclear | $W^{\pm}$, $Z^0$ | $10^{-8}$ | $10^{-18}$ |
| Electromagnetic | $\gamma$ | $10^{-20}$ | $\infty$ |

## 1.2 The Standard Model

### 1.2.1 Fundamental Particles and Forces

The Standard Model [1] of particle physics is a theory which describes the properties of, and interactions between, the elementary constituents of all matter in the universe. The elementary particles contained within the Standard Model are conventionally split into three groups: quarks, leptons and force mediators.

The fundamental forces of the Standard Model include the strong nuclear, weak nuclear and electromagnetic interactions. Gravity and its associated mediator, the graviton, are not usually included since its effects are not significant at the energies of particle accelerator experiments. Table 1.1 lists some properties of the Standard Model forces.

In elementary particle physics the particles are, by definition, pointlike (or at least too small to be measured) and are usually travelling with relativistic velocities. Therefore, a theory describing elementary particle behaviour must include the principles of relativity and quantum mechanics. Such a theory was developed primarily by Feynman, Schwinger and Tomonaga in the 1940s and 1950s to describe electromagnetic interactions: Quantum Field Theory (QFT) [2].

Classical mechanics describes point particles and allows the calculation of a particle's trajectory, $x(t)$. Classical field theory is concerned with calculating $n$ functions of space-time, $x_\mu$, and hence replaces the classical trajectory with the classical field, $\phi(x_\mu)$. In QFT the quantisation of the fields can be achieved through turning them into field operators, $\phi(x_\mu) \rightarrow \hat{\phi}(x_\mu)$, and imposing commutation relations. The operators can then be expanded in terms of the annihilation and creation operators, $\hat{a}^\dagger$ and $\hat{a}$. Observed particles are then interpreted as the discrete, quantised states created by these operators. The application of QFT to particle physics leads to the interpretation of a force between two particles as being the exchange of the force field's quanta (i.e. the mediator) between them. For example, the electromagnetic force between two participating charged particles is mediated by the emission and absorption of photons - the quanta of the electromagnetic interaction.

### 1.2.2 Gauge Theories

Strong, electromagnetic and weak interactions are described by the Standard Model in terms of gauge theories derived within the framework of Lagrangian field theory. The Lagrangians themselves are functions of the $\phi_i$ and their space-time derivatives, $\partial_\mu \phi_i$ where $\partial_\mu \equiv \frac{\partial}{\partial x^\mu}$. Lagrangian densities are chosen such that they remain invariant under global gauge transformations of the fields, $\phi \rightarrow e^{i\alpha}\phi$, where $\alpha$ is a continuous, real valued variable. A gauge theory requires that this holds locally, i.e. when the transformation is a function of $x_\mu$: $\phi \rightarrow e^{i\alpha(x_\mu)}\phi$. This requirement leads to the introduction of terms to the Lagrangian representing vector fields (the gauge bosons) and the interactions between otherwise free fields. All the fundamental interactions of the Standard Model are generated in this manner.

The motivation for gauge invariance is provided by Nöther's theorem relating symmetries and conservation laws. It states that for every observed symmetry there is an associated conserved quantity, and vice versa. For example, the laws of physics are invariant under translations in space-time which, according to Nöther's theorem, implies conservation of energy and momentum. Similarly, imposing a symmetry upon a Lagrangian will uncover an underlying conservation law.

Consider the example of Quantum Electrodynamics (QED). Beginning with the Dirac field equation governing the behaviour of a free spinor (spin-$\frac{1}{2}$) field $\psi$ of mass $m$,

$$i\gamma^\mu \partial_\mu \psi - m\psi = 0 \tag{1.1}$$

a Lagrangian (density) can be chosen such that equation 1.1 is recovered following the application of the generalised Euler-Lagrange equations for a given set of field components $\phi_i$,

$$\partial_\mu \left( \frac{\partial \mathcal{L}}{\partial(\partial_\mu \phi_i)} \right) = \frac{\partial \mathcal{L}}{\partial \phi_i}. \tag{1.2}$$

A Lagrangian that satisfies this requirement is the Dirac Lagrangian,

$$\mathcal{L} = i\overline{\psi}\gamma^\mu \partial_\mu \psi - m\overline{\psi}\psi. \tag{1.3}$$

It is trivial to see that the Dirac Lagrangian is invariant under a global gauge transformation of the field, $\psi \rightarrow e^{i\alpha}\psi$. $\mathcal{L}$ is said to adhere to $U(1)$ global gauge invariance, where $U(1)$ is the Abelian group of unitary $1 \times 1$ matrices formed by the continuous variable $\alpha$. Relating the result to Nöther's theorem; the identified $U(1)$ gauge symmetry leads to a conserved current in QED which is interpreted as the conservation of electric charge:

$$\partial_\mu j^\mu = 0 \tag{1.4}$$

where the current $j^\mu = -e\overline{\psi}\gamma^\mu\psi$.

Moving to the more general case of local $U(1)$ gauge invariance the transformations now become functions of space-time: $\alpha \rightarrow \alpha(x_\mu)$. Because of this, the Dirac Lagrangian is not invariant under a local transformation and $\mathcal{L}$ becomes,

$$\mathcal{L} \rightarrow \mathcal{L} + i\overline{\psi}\gamma^\mu\psi\partial_\mu\alpha \tag{1.5}$$

where $\partial^\mu \alpha$ is said to have broken the invariance of $\mathcal{L}$. The invariance of $\mathcal{L}$ can be enforced via the introduction of a derivative that transforms in the same manner as $\psi$, i.e. $D_\mu \psi \to e^{i\alpha} D_\mu \psi$. The covariant derivative, $D_\mu$, is chosen such that it cancels the unwanted term in equation 1.5 and is given by

$$D_\mu \equiv \partial_\mu - iqA_\mu \tag{1.6}$$

where $q$ is the electric charge of the Dirac particle and $A_\mu$ is a vector field (or gauge field) that has been introduced to satisfy invariance. Furthermore, $A_\mu$ is required to transform like

$$A_\mu \to A_\mu + \frac{1}{q}\partial_\mu \alpha. \tag{1.7}$$

By replacing $\partial_\mu$ in equation 1.3 with $D_\mu$ the invariance of $\mathcal{L}$ is restored. If $A_\mu$ is to be interpreted as the physical photon field then a further term must be included in $\mathcal{L}$ to represent the freely propagating photon. The Lagrangian for a free vector (spin-1) field can be written as

$$\mathcal{L}_V = -\frac{1}{4}F^{\mu\nu}F_{\mu\nu} + \frac{1}{2}m_A^2 A^\nu A_\nu \tag{1.8}$$

where the subscript $V$ denotes a vector field, $F_{\mu\nu} = \partial_\mu A_\nu - \partial_\nu A_\mu$ and $m_A$ is the mass of the gauge boson, the photon. The first term in equation 1.8 is invariant under local $U(1)$ gauge transformations, however the second is not. Invariance can be assured by setting $m_A = 0$, i.e. by requiring the photon to be massless. Therefore the Lagrangian for QED becomes:

$$\mathcal{L}_{QED} = \overline{\psi}(i\gamma^\mu \partial_\mu - m)\psi + q\overline{\psi}\gamma^\mu A_\mu \psi - \frac{1}{4}F^{\mu\nu}F_{\mu\nu}. \tag{1.9}$$

Therefore, imposing local gauge invariance on a freely propagating Dirac field leads to an interacting field theory for the electromagnetic interaction.

The same methods can be used to derive similar Lagrangians for the weak and strong nuclear interactions, i.e. through imposing a local gauge symmetry. Hence the propagators of these forces can be generated and the conserved quantities within the interactions can be identified. The theory laid out by Yang and Mills [3] shows how to extend local gauge invariance to include non-Abelian groups such as $SU(n)$ where $n > 1$. Quantum chromodynamics (QCD) is represented by the $SU(3)$ group where the number 3 arises from the number of quark colours in the theory. The QCD Lagrangian representing the strong interaction can be written as:

$$\mathcal{L}_{QCD} = \overline{q}(i\gamma^{\mu}\partial_{\mu} - m)q - g(\overline{q}\gamma^{\mu}T_a q)A^a_{\mu} - \frac{1}{4}F^a_{\mu\nu}F^{\mu\nu}_a \tag{1.10}$$

where $A^a_{\mu}$ ($a = 1, \ldots, 8$) are eight gauge fields (gluons), $T_a$ are the generators of the gauge fields, $q$ ($\overline{q}$) represents a (anti-)quark field, $g$ represents the coupling strength (colour charge, analogous to electric charge in QED), and $F^a_{\mu\nu}$ is the field strength tensor of the strong interaction given by

$$F^a_{\mu\nu} = \partial_{\mu}A^a_{\nu} - \partial_{\nu}A^a_{\mu} - gf_{abc}A^b_{\mu}A^c_{\nu} \tag{1.11}$$

where $f_{abc}$ are structure constants arising from the transformation of the gauge fields. As in the case of the QED Lagrangian, the gauge fields (eight gluons in this case) of QCD are required to be massless. The last term in equation 1.11 introduces self-coupling of the QCD gauge fields. These gluon self-interations are due to the fact that the gluons themselves carry colour charge. This feature arises from the non-Abelian nature of the $SU(3)$ gauge group and is not present in QED because the photons do not carry electric charge.

Although not a unification in the strictest sense (there are still two coupling contants and hence two forces), the electroweak theory developed by Glashow, Weinberg and Salam [4–6] (GWS) describes the electromagnetic and weak interations in an $SU(2) \times U(1)_Y$ representation, where $Y$ denotes hypercharge to differentiate it from the $U(1)$ group of QED. Applying gauge theory to the electroweak interaction is not as straightforward as in QED or QCD because the mediators of the weak force are not massless. In addition to destroying the symmetry, the introduction of mass terms by hand into the electroweak Lagrangian renders the theory unrenormalisable.

The method used to impart mass to the fermions and $W$ and $Z^0$ bosons, while retaining the renormalisability and hence predictive abilities of the theory, is known as the Higgs mechanism [7], and it employs the concept of spontaneous symmetry breaking. A direct result of the Higgs mechanism is the introduction of at least one new, massive scalar (spin-0) particle called the Higgs boson. These methods will not be discussed any further here because their details are not relevant to this thesis, however the conclusions of their application are important. They allow the Standard Model of particle interactions to be formulated as a gauge theory representing the $SU(3)\times SU(2)\times U(1)_Y$ gauge group. The minimal Standard Model (SM) Lagrangian is then written as:

$$\mathcal{L}_{SM} = \mathcal{L}_{SU(3)} + \mathcal{L}_{SU(2)} + \mathcal{L}_{U(1)_Y}. \tag{1.12}$$

It has been shown by 't Hooft [8] that the spontaneously broken gauge theory of GWS is renormalisable; that is, process amplitudes do not diverge in the limit of infinite momentum transfer, and finite predictions can be made from the theory. Consequently, experimental high energy physics is able to systematically test the theory to an ever increasing accuracy.

### 1.2.3 The Weak Interaction

In the case of the leptonic weak vertex, couplings across the three generations of lepton doublets,

$$\begin{pmatrix} \nu_e \\ e \end{pmatrix}, \qquad \begin{pmatrix} \nu_\mu \\ \mu \end{pmatrix}, \qquad \begin{pmatrix} \nu_\tau \\ \tau \end{pmatrix},$$

are forbidden by the conservation of electron, muon and tau lepton number. For example, the vertex $\mu^- \to \nu_e + W^-$ is not allowed by this law. However, it should be noted that this is only true in the case of massless neutrinos. Experiments have observed neutrino flavour oscillations [9, 10], implying $m_{\nu_\ell} > 0$ and hence couplings between the leptonic generations.

An analogous set of generations exists for the quarks:

$$\begin{pmatrix} u \\ d \end{pmatrix}, \qquad \begin{pmatrix} c \\ s \end{pmatrix}, \qquad \begin{pmatrix} t \\ b \end{pmatrix}.$$

However, because all quarks have mass there is no analogous conservation law and therefore processes involving generation changing charged currents are allowed to occur, e.g. $c \to d + W^+$. Before the $c$, $b$ and $t$ quarks were known to exist, it was suggested that instead of the $W$ boson coupling to the physical, mass eigenstates, $d$ and $s$, it couples to the rotated, weak eigenstates $d'$ and $s'$. The rotated states are linear combinations of the mass eigenstates:

$$d' = d\cos\theta_c + s\sin\theta_c \tag{1.13}$$

$$s' = -d\sin\theta_c + s\cos\theta_c \tag{1.14}$$

where $\theta_c$ is the Cabibbo quark mixing angle. Cabibbo first introduced the doublet $u$, $d'$ to explain the weak decay of strange particles [11], e.g. $K^+ \to \mu^+\nu_\mu$. Experimentally, the Cabibbo angle is found to be small ($\theta_c \approx 13°$) such that vertices carrying a factor of $\cos\theta_c \simeq 0.97$ and $\sin\theta_c \simeq 0.22$ are said to be Cabibbo favoured (CF) and Cabibbo suppressed (CS), respectively. Processes involving two Cabibbo suppressed vertices are termed doubly Cabibbo Suppressed (DCS).

Cabibbo's theory was successful in explaining many experimental observations. However, one outstanding problem was the lack of any theoretical justification for the small measured limit on the rate of the weak neutral current process $K^0_S \to \mu^+\mu^-$.

A solution to this was presented by Glashow, Illiopoulos and Maiani (GIM) in 1970 [12]. By introducing a fourth quark, $c$, the existing theoretical decay amplitude was effectively cancelled out by an interfering process where the virtual $u$ quark is replaced with a $c$ quark. The simultaneous discovery of the $J/\psi$ meson at SLAC and Brookhaven [13,14] in 1974, followed by the discovery of the $D^0$ and $D^+$ mesons at SLAC in 1976 [15] lent strong support to the GIM mechanism.

Extending the Cabibbo-GIM weak mixing scheme to three quark generations is done by simply adding the $t$,$b'$ doublet. The formalism was worked out by Kobayashi and Maskawa. The positively charged weak current then becomes

$$J^\mu = \begin{pmatrix} \overline{u} & \overline{c} & \overline{t} \end{pmatrix} \frac{1}{2}\gamma^\mu(1-\gamma^5)V_{CKM} \begin{pmatrix} d \\ s \\ b \end{pmatrix} \tag{1.15}$$

where $V_{CKM}$ is the full Cabibbo-Kobayashi-Maskawa (CKM) quark mixing matrix,

$$V_{CKM} = \begin{pmatrix} V_{ud} & V_{us} & V_{ub} \\ V_{cd} & V_{cs} & V_{cb} \\ V_{td} & V_{ts} & V_{tb} \end{pmatrix} \tag{1.16}$$

which can be reduced and written in terms of four independent parameters; three Cabibbo-like angles, $\theta_1$, $\theta_2$ and $\theta_3$ and one phase factor, $\delta$. The phase factor allows $V_{CKM}$ to be complex and hence facilitates matter-antimatter asymmetry in the weak interation, i.e. the interactions are not invariant under the combined charge (C) and parity (P) transformations, a phenomenon known as *CP*-violation. Letting $s_i$ and $c_i$ denote $\sin\theta_i$ and $\cos\theta_i$ respectively the CKM matrix can be defined [16] as:

$$V_{CKM} = \begin{pmatrix} c_1 & s_1c_3 & s_1s_3 \\ -s_1c_2 & c_1c_2c_3 - s_2s_3e^{i\delta} & c_1c_2s_3 + s_2c_3e^{i\delta} \\ -s_1s_2 & c_1s_2c_3 + c_2s_3e^{i\delta} & c_1s_2s_3 - c_2c_3e^{i\delta} \end{pmatrix} \tag{1.17}$$

Setting $\theta_2 = \theta_3 = 0$ recovers the original Cabibbo scheme in which the third quark generation mixes with neither the first nor second. The magnitudes of the CKM matrix elements are determined by studying processes containing the relevant quark transition vertices. Current experimental evidence suggests that, with 90% confidence [17],

$$V_{CKM} = \begin{pmatrix} 0.9739 \text{ to } 0.9751 & 0.221 \text{ to } 0.227 & 0.0029 \text{ to } 0.0045 \\ 0.221 \text{ to } 0.227 & 0.9730 \text{ to } 0.9744 & 0.039 \text{ to } 0.044 \\ 0.0048 \text{ to } 0.014 & 0.037 \text{ to } 0.043 & 0.9990 \text{ to } 0.9992 \end{pmatrix} \quad (1.18)$$

The magnitudes of the off-diagonal elements in the third row and column suggest that mixing between the third quark generation and the other two is small. This is reflected in the long measured lifetimes of the $B$ mesons, $\sim 1.5 \times 10^{-12}$ s [17].

## 1.3 Charmed Meson Decays

All weak decays of mesons, charmed or otherwise, can be described by six quark diagrams [16,18], each of which is shown in figure 1.1. The diagrams, labelled (a) to (f), represent the external $W$-emission, internal $W$-emission, annihilation, $W$-loop or penguin, $W$-exchange, and mixing processes respectively.

External and internal $W$-emission are thought to be the dominant processes in hadronic charm decays. The enforcement of local gauge invariance in the context of QCD reveals colour charge to be a conserved quantity at all interaction vertices. Moreover, all naturally occuring particles are observed to be colour singlet states, i.e. colourless. Therefore, in order for the quarks produced by the internally emitted $W$ to hadronise with the other two quarks in the process, they must possess the same colour as the quarks in the initial charmed meson state. This is expected to reduce the rate of such processes by a factor of around three compared to decays with an externally emitted $W$ purely because less final state combinations are possible. This phenomenon is known as colour suppression. It is possible colour suppression can be significantly relieved through soft gluon exchange between the quarks, or through Final State Interations (FSI) where the outgoing quarks can rescatter into an alternative final state. For example, the Feynman diagrams in figure 1.2 show

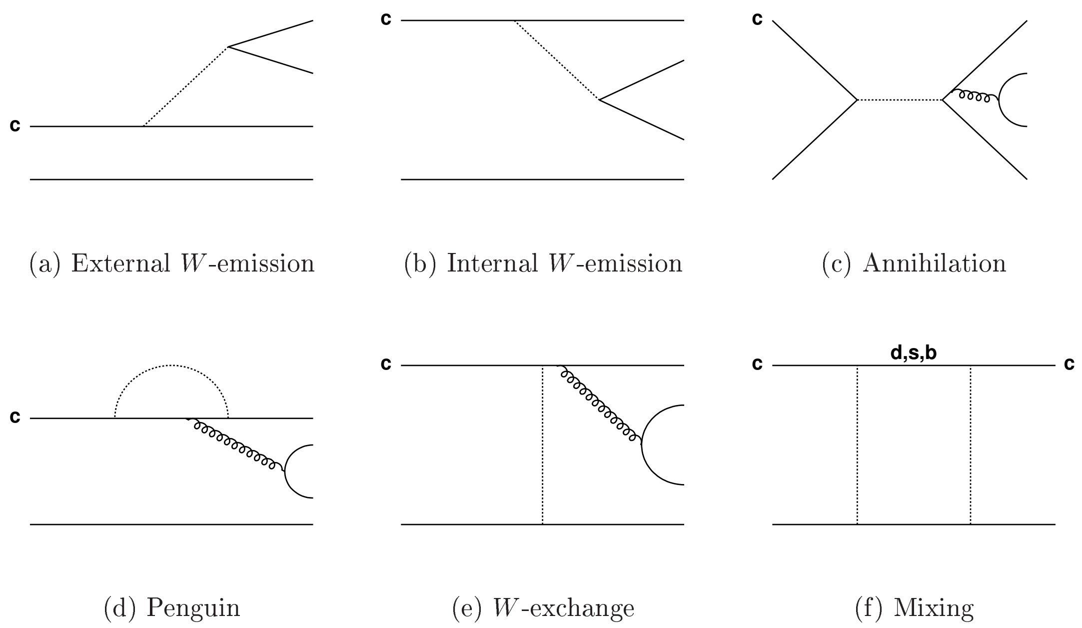


**Figure** 1.1: The six quark level Feynman diagrams that encompass all decays of a charmed meson. Solid lines represent fermions, dashed lines represent virtual $W$ bosons and curly lines represent virtual gluons. The incoming $c$ quark is labelled in each case.

two topologically similar decay modes of the $D^0$ meson which have identical CKM factors. In fact, the only difference is that the diagram in figure 1.2(a) is colour suppressed while the one in figure 1.2(b) is not. Therefore, a measurement of their width ratio can quantify the effect that colour suppression has on decay rates of charmed mesons. Experimentally it is found [17],

$$\frac{\Gamma(D^0 \to \overline{K}^0\pi^0)}{\Gamma(D^0 \to K^-\pi^+)} = 0.60 \pm 0.06 \tag{1.19}$$

which far exceeds the value of $\frac{1}{18}$ predicted through using a factor of $\frac{1}{3}$ for colour suppression. The result is interpreted as evidence that one or more other processes are reducing the strength of the colour suppression effect relative to expectations.

The largest effects in penguin ($W$-loop) diagrams are introduced via the heaviest virtual quarks, $s$ and particularly $b$ in this case. The decay widths for these processes

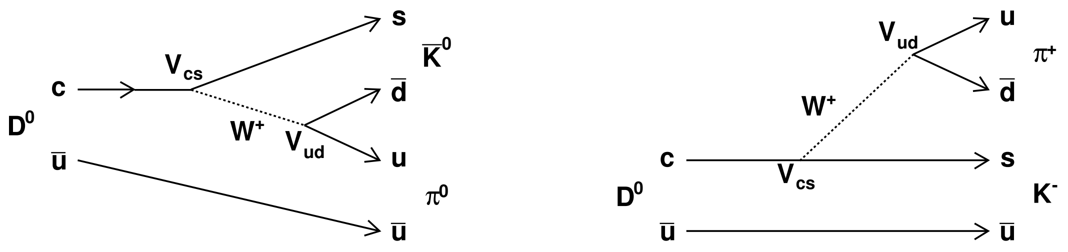


(a) $D^0 \to \overline{K}^0\pi^0$ (b) $D^0 \to K^-\pi^+$

**Figure** 1.2: Leading order Feynman diagrams for two decay modes of the $D^0$ meson. The $V_{CKM}$ elements acting at each weak vertex are included for clarity. The only difference between the two Cabibbo favoured processes is that the left hand diagram is colour suppressed.

therefore carry a factor of $|V_{cb}| \cdot |V_{ub}|$. Experimentally these CKM matrix elements are found to be $\ll 1$ (equation 1.18) and as a result the penguin contributions are expected to be heavily suppressed.

Contributions from the annihilation diagram are suppressed for the same reason the muon is favoured over the electron in the leptonic decay of the pion, where the width ratio is measured to be [17]

$$\frac{\Gamma(\pi^+ \to e^+\overline{\nu}_e)}{\Gamma(\pi^+ \to \mu^-\overline{\nu}_\mu)} = (1.230 \pm 0.004) \times 10^{-4} \tag{1.20}$$

The diagram for a decay of this type is the same as figure 1.1(c) except the outgoing fermion lines are leptons (not quarks) and hence there is no gluon emission and subsequent $q\overline{q}$ production. Considering the available phase space for such a process leads to the conclusion that the final state with the smallest mass would be the favoured process. However, in the case of a purely leptonic $D_s$ decay, the decay width is given by

$$\Gamma(D_s^+ \to \ell^+\nu_\ell) = \frac{G_F^2}{8\pi}|V_{ci}|^2 f_{D_s}^2 m_{D_s} m_\ell^2 \left(1 - \frac{m_\ell^2}{m_{D_s}^2}\right)^2 \tag{1.21}$$

where $G_F$ is the weak (Fermi) coupling constant, $f_{D_s}$ is an experimentally determined $D_s$ decay constant and $i$ denotes the flavour of the quark to which the $c$ quark has mixed.

The suppression results from the conservation of spin angular momentum. The $D_s$ meson is a pseudoscalar meson with total spin 0, as is the $\pi^+$. Therefore, the lepton and anti-neutrino produced by the $W$ decay in the $D_s$ meson centre of mass frame must carry oppositely aligned spins of $+\frac{1}{2}$ and $-\frac{1}{2}$, and hence have equal helicities. The approximately massless anti-neutrino must be righthanded (helicity=+1) according to the $V - A$ ($\gamma^\mu - \gamma^\mu\gamma^5$) form of the weak current. If the lepton were massless then it would be lefthanded, and thus violate conservation of spin angular momentum in the $D_s$ meson decay. Therefore, it is the small mass of the outgoing states that leads to the suppression of the decay width. Extending this idea to a hadronic $D_s$ decay, the asymptotically free $u$ and $d$ current-quark masses are small (of order 1 and 4 MeV/$c^2$ respectively) compared to the $\sim 2\,\text{GeV}/c^2$ $D_s$ meson which leads to helicity suppression of two body hadronic charm decays via annihilation.

Furthermore, it has been suggested [19] that in decays of the type $D \to P_1P_2$, where $D$ represents a charmed meson and $P_1$ and $P_2$ represent two pseudoscalar final state mesons, the amplitude, $\mathcal{A}$, contributed through annihilation,

$$\mathcal{A} \propto \frac{m_{P_2}^2 - m_{P_1}^2}{m_D^2} \tag{1.22}$$

which becomes heavily suppressed due to the comparatively large mass of the $D$ meson. In the chiral limit (massless quarks) this amplitude vanishes completely, analogous to the helicity suppression discussed above.

Although only relevant for neutral $D$ mesons, the mixing diagram is suppressed for the same reason penguin amplitudes are. It is worth mentioning that current experimental results support these arguments with both semileptonic and purely hadronic analyses yielding the following limits for $D^0$ decays [17], respectively:

$$\frac{\Gamma(K^+\ell^-\overline{\nu}_\ell\,(\text{via}\,\overline{D}^0))}{\Gamma(K^-\ell^+\nu_\ell)} < 0.005, \qquad \text{CL} = 90\%$$

$$\frac{\Gamma(K^+\pi^-\,(\text{via}\,\overline{D}^0))}{\Gamma(K^-\pi^+)} < 4.1\times 10^{-4}, \qquad \text{CL} = 95\%$$

## 1.4 Signal Decay Modes

The analysis presented in this thesis is focused on the search for three, as yet unobserved, rare decay modes of the $D_s$ meson; $D_s^+ \to K^+\pi^0$, $D_s^+ \to \pi^+\pi^0$, and $D_s^+ \to \pi^+K^0$. They are rare for a number of different reasons.

The leading order Feynman diagrams contain one Cabbibo suppressed vertex in the cases of $D_s^+ \to K^+\pi^0$ (figure 1.3(a)) and $D_s^+ \to \pi^+K^0$ (figure 1.3(c)), namely $V_{cd}$. Moreover, the $D_s^+ \to K^+\pi^0$ decay rate is colour suppressed.

On initial inspection, the process $D_s^+ \to \pi^+\pi^0$ is Cabibbo favoured through the annihilation of the $c$ and $\overline{s}$ quarks (figure 1.3(b)) and colour-allowed, which leads to a large expected rate. However, following the argument outlined in the previous section this decay is found to be helicity suppressed.

Each of the three signal channel decay widths is measured with respect to a Cabibbo allowed reference mode: $D_s^+ \to K^+\overline{K}^0$ (figure 1.3(d)). The motivation for this choice is presented in section 1.6.

Because the signal $D_s$ decay processes presented here are rare, due to the various factors outlined above, their decay rates are small, $\mathcal{O}(10^{-3})$ or less, and consequently challenging to determine experimentally. Quantitative predictions of the decay rates are presented in the next section. Despite these difficulties, the large statistics *BABAR* data sample combined with efficient background rejection leads to a realistic possibility of an observation.

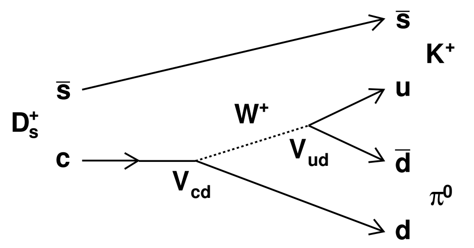


(a) $D_s^+ \to K^+\pi^0$

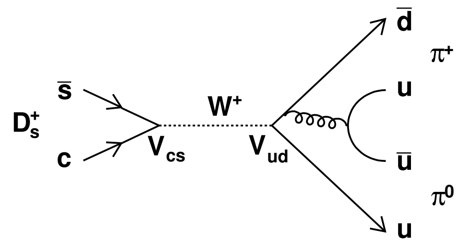


(b) $D_s^+ \to \pi^+\pi^0$

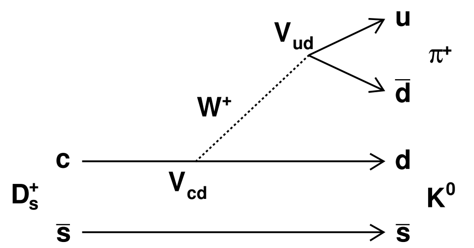


(c) $D_s^+ \to \pi^+K^0$

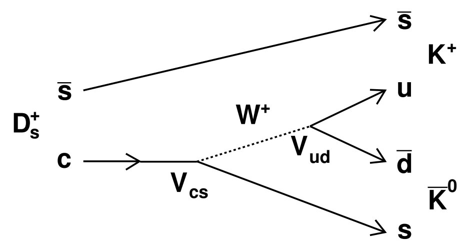


(d) $D_s^+ \to K^+\overline{K}^0$

**Figure** 1.3: Leading order Feynman diagrams for the $D_s$ decay modes reconstructed for this thesis. The $V_{CKM}$ elements are included at each weak vertex for clarity.

### 1.4.1 Theoretical Predictions

Nonleptonic decays of heavy mesons are notoriously difficult to describe with existing theory. No adequate theoretical framework based upon general principles currently exists that can produce good quantitative agreement with experimental measurement. However, several approximate methods and models exist, some of which are outlined in this section.

A starting point common to many theoretical techniques (including the ones described here) is to begin with some effective weak Hamiltonian for the two-body decay of charmed mesons:

$$H_W = \frac{G_F}{\sqrt{2}} V_{ci} V_{uj}^* \{ a_1 \, (\overline{u}\Gamma_\mu q_j)(\overline{q}_i \Gamma^\mu c) + a_2 \, (\overline{u}\Gamma_\mu c)(\overline{q}_i \Gamma^\mu q_j) \} \tag{1.23}$$

where $V_{qq'}$ is an element of the CKM quark mixing matrix, $i$ and $j$ represent either $d$ or $s$ quarks, $\Gamma_\mu = \gamma_\mu(1-\gamma^5)$, and $a_1$ and $a_2$ are the commonly termed Wilson coefficients [20] which are determined not from QCD, but from a fit to data. The quark currents in equation 1.23 correspond to the decay of a neutral $D$ meson, but in principle the Hamiltonian for other $D$ meson decays can be formed by exchanging these for a $c\,\overline{d}$ or $c\,\overline{s}$ initial state and replacing the CKM matrix elements with the relevant ones.

An attempt to describe the two-body nonleptonic decays of heavy mesons was made by Bauer, Stech and Wirbel (BSW) [21]. Instead of using strict QCD to make predictions they take equation 1.23 and use the method of factorisation to obtain $H_W$ for a specific exclusive hadronic decay. This involves replacing the quark currents with effective hadron currents to obtain the product of two hadronic matrix elements, and identifying the contributing diagrams in figure 1.1. The BSW model assumes that the amplitude, $\mathcal{A}$, is given either by terms multiplying $a_1$ (external $W$-emission), $a_2$ (internal $W$-emission) or both with all other contributions neglected. In this picture the amplitude for the decay $D^0 \to K^-\pi^+$, which has only an external $W$-emission diagram, becomes

$$\mathcal{A} = \frac{G_F}{\sqrt{2}} V_{cs} V_{ud}^{*} a_1 \left\langle \pi^+ \right| (\overline{u}d)_H \left| 0 \right\rangle \left\langle K^- \right| (\overline{s}c)_H \left| D^0 \right\rangle \tag{1.24}$$

where $(q\overline{q})_H$ indicates the change has been made to hadron field operators as described in [21] and references therein.

In the BSW approximation scheme all that is needed to make predictions of nonleptonic decay widths are the relevant meson decay constants and matrix element calculations. However, the predictions supplied by the model do not agree well with experimental data, particularly for $D_s$ decays. For example, they predict $\mathcal{B}(D_s^+ \to K^+ K_S^0) = (1.89 \pm 0.34) \times 10^{-2}$ [22] which is significantly smaller than the result from experiment to be discussed later in section 1.6. They do, however, acknowledge that annihilation contributions (which they have ignored in the limit of vanishing quark masses) could in fact play a significant role. In particular the presence of soft gluons inside hadrons can alleviate the helicity suppression by facilitating momentum transfer between the constituent quarks and gluons. The extent to which annihilation diagrams contribute to decay widths is not known. It has been argued [19] that in two body decays of the type $D \to PV$ and $D \to VV$ the contributions of intermediate pseudoscalar ($P$) and vector ($V$) meson poles cancel each other in the chiral limit, while the annihilation contributions for $D \to PP$ decays vanish independently.

An alternative method was devised around the same time as the BSW scheme by Chau and Cheng [23]. They proposed theoretical predictions of two-body hadronic decays of charmed mesons through a model-independent analysis of contributing quark diagrams (figure 1.1). All contributing amplitudes and the CKM matrix are determined through a direct comparison with experimental measurements of non-leptonic decays. Chau and Cheng also acknowledge the significance of SU(3) symmetry breaking and final state interations (FSI) in their scheme. They distinguish between the contributions from $d$ and $s$ quarks in penguin diagrams, and state that non-zero penguin contributions are an effect of SU(3) breaking. A further discussion on SU(3) symmetry breaking by Chau and Cheng, with reference to experimental measurement, can be found elsewhere [24]. FSI are included primarily as arguments for explaining the significant $D^+$ and $D^0$ lifetime difference.

In conclusion, they find contributions to the processes $D_s^+ \to K^+\pi^0$ and $D_s^+ \to \pi^+K^0$ from figures 1.1 (a), (b), (c) and (d). Unfortunately, they do not quote branching fraction predictions within the literature, except in the case of $D_s^+ \to \pi^+\pi^0$ where none of the diagrams which they consider are expected to contribute, in which case a decay rate of zero can be inferred.

The work of Bucella *et al.* [25, 26] claims that the infinitely heavy quark approximation ($m_c \to \infty$) is far from the true situation, and they therefore conjecture that heavy quark effective theory (HQET) [27] is not useful for purely hadronic decays of heavy flavour mesons. Instead, they use the factorization approach as described in [21] and determine the free parameters in their model via a fit to data. $W$-exchange and annihilation contributions, deemed to be significant, are included,

**Table** 1.2: Predictions of branching fractions for the signal modes of this analysis.

| Predictor | Branching Fraction Prediction / % | | |
|---|---|---|---|
| | $D_s^+ \to K^+\pi^0$ | $D_s^+ \to \pi^+K^0$ | $D_s^+ \to \pi^+\pi^0$ |
| Chau and Cheng [23] | - | - | 0 |
| Bucella *et al.* [25] | 0.16 | 0.43 | - |
| Lusignoli and Pugliese [28] | 0.146 | 0.373 | - |

as are FSIs, which are assumed to be dominated by nearby charm resonances. The latter are found to be particularly important for the large SU(3) breaking effects observed in experimental data. Quantitative branching fraction predictions for the signal decay modes are given in table 1.2.

A further conclusion of Buccela *et al.* is that significant penguin contributions can lead to $CP$-violating asymmetries at a level greater than $10^{-3}$. However, the statistical sensitivity of the analysis presented in this thesis is not expected to be sufficient to observe such effects.

The work of Bucella *et al.* is expanded upon by two of its contributors, Lusignoli and Pugliese [28], in response to claims made by Close and Lipkin [29] that new physics may be required to explain some large observed $D^+$ branching fractions. Discrepencies between theory and data regarding the ratio of CS and DCS decays to CF decays are explained by the effect of large annihilation contributions in the CS channels of the $D_s$ meson, such as $D_s^+ \to \pi^+K^0$ and $D_s^+ \to K^+\pi^0$. A refinement of their theoretical model based on the factorisation approximation and a subsequent fit to existing data yield new predictions of the $D_s \to PP$ decays studied in this thesis (table 1.2).

Despite the conclusions of Bucella *et al.*, an analysis of nonleptonic charmed meson decays using HQET and chiral perturbation theory has been done by Bajc *et al.* [30]. However, they only consider $D$ meson decay modes where the final state involves a single isospin in order to avoid the effect of FSIs. Consequently, they make no predictions for the relevant $D_s \to PP$ decays studied here.

### 1.4.2 Experimental Measurements

There are currently no published experimental observations of the two-body hadronic $D_s$ decay modes studied in this thesis. The only upper limit that exists is $\mathcal{B}(D_s^+ \to \pi^+ K^0) < 8 \times 10^{-3}$ with 90% confidence [17].

## 1.5 Charmed Strange Meson Production at *BABAR*

There are two distinct production processes of charmed, strange mesons at the *BABAR* experiment. Direct production occurs from $e^+e^- \to c\bar{c}$ followed by fragmentation of the $c\bar{c}$ pair. Production can also occur indirectly through the decays of $B$ mesons.

For the analysis presented in this thesis the choice is made to only use charmed strange mesons produced via $c\bar{c}$ fragmentation. Moreover, only events in which a $D_s^*$ meson is directly produced in the fragmentation are considered. This is desirable because the $D_s^*$ meson decays almost exclusively via a radiative process with $\mathcal{B}(D_s^{*+} \to D_s^+ \gamma) = (94.2 \pm 2.5)\%$ [17]. The remainder of the $D_s^*$ decay width consists of the isospin violating process $D_s^{*+} \to D_s^+ \pi^0$ mentioned in section 1.4. The photon provides an extra constraint with which to reject background, through the calculated mass difference, $\Delta M$, between the reconstructed $D_s$ and $D_s^*$. $\Delta M$ is an important variable for the maximum likelihood analysis developed in section 3.5.

Using $D_s^{(*)}$ mesons from $c\bar{c}$ events also introduces a powerful background discriminant in the form of the normalised momentum,

$$x_p = \frac{p^*_{D_s^*}}{\sqrt{{E^*_{beam}}^2 - m^2_{D_s^*}}} \tag{1.25}$$

where $p^*_{D_s^*}$ is the c.m. momentum of the reconstructed $D_s^*$ meson, $E^*_{beam} = \sqrt{s}/2$ or half the total energy of the $e^+e^-$ annihilation in the c.m. frame and $m_{D_s^*}$ is the nominal mass of the $D_s^*$ meson. At *BABAR* there are more particles produced with lower momentum than higher momentum, which implies more particle combinations and therefore a worse signal to background ratio at lower momentum. This combinatoric background is greatly reduced (and the signal to background ratio improved) by preferentially selecting mesons with high $x_p$ values. All $D_s^*$ mesons originating from $B$ decays are kinematically forbidden at values of $x_p$ greater than $\sim 0.5$, which is why only $c\bar{c}$ production is relevant for this analysis.

The CLEO collaboration have made measurements of $c\bar{c}$ fragmentation into $D_s^*$ and $D_s$ mesons in $e^+e^-$ annihilations at a centre of mass energy equal to the $\Upsilon(4S)$ mass [31]. The measurement is feasible because $x_p$ allows the complete removal of $D_s^*$ mesons originating from $B$ decays. A conclusion of the CLEO study is a measure of the relative production rate of vector and pseudoscalar mesons, $P_V$, defined as

$$P_V = \frac{N_V}{N_V + N_P} \tag{1.26}$$

where $N_P$ and $N_V$ are the number of vector ($D_s^*$) and pseudoscalar ($D_s$) mesons produced through the $e^+e^-$ annihilation production mechanism. They find $P_V = 0.44 \pm 0.04$ for events where the normalised momentum of the $D_s$ is greater than 0.44.

## 1.6 Reference Decay Mode

In order to measure accurately the branching fraction of a $D_s$ decay mode, the number of $D_s$ mesons that were initially produced has to be determined. Unfortunately, despite knowledge of both $P_V$ and the cross-section for $e^+e^- \to c\bar{c}$ at the $\Upsilon(4S)$ mass, the production rate of strange quarks from $c\bar{c}$ fragmentation is not well known. Moreover, the process of hadronisation is non-perturbative and phenomenological models are used. Therefore, to avoid these complications, a reference mode with a prior known branching fraction is reconstructed for the purposes of normalisation. An accurate measurement of a signal branching ratio can then be made with respect to the reference mode and a branching fraction can be subsequently calculated.

The chosen mode is the relatively well measured CF and colour allowed decay $D_s^+ \to K^+\overline{K}^0$ (figure 1.3(d)). Topologically the decay is very similar to the three signal decay modes, which makes it a good choice. For each mode, the $D_s$ decays to a charged track plus either a neutral kaon or neutral pion, which are reconstructed from $\pi^+\pi^-$ and $\gamma\gamma$ respectively. The decays all have three final state particles and will therefore have a similar detector acceptance. Hence, many systematic errors can be cancelled in the branching ratio measurements, leading to a more accurate result.

Currently, the Particle Data Group [17] quotes the branching fraction $\mathcal{B}(D_s^+ \to K^+\overline{K}^0) = (3.6 \pm 1.1) \times 10^{-2}$ which is calculated from the measurements of $\mathcal{B}(D_s^+ \to \phi\pi^+)$ and the ratio of these two branching fractions. However, a recent measurement [32] made by the *BABAR* collaboration yields the branching fraction

$$\mathcal{B}(D_s^+ \to \phi\pi^+) = (4.81 \pm 0.52 \pm 0.38) \times 10^{-2} \tag{1.27}$$

where the first and second errors are statistical and systematic respectively. These measurements are combined to form a weighted average:

$$\mathcal{B}(D_s^+ \to \phi\pi^+) = (4.4 \pm 0.5) \times 10^{-2} \tag{1.28}$$

Combining this improved value with the $K^+\overline{K}^0$ and $\phi\pi^+$ width ratio [17],

$$\frac{\Gamma(D_s^+ \to \phi\pi^+)}{\Gamma(D_s^+ \to K^+\overline{K}^0)} = 1.01 \pm 0.16 \tag{1.29}$$

allows a more accurate value for $\mathcal{B}(D_s^+ \to K^+\overline{K}^0)$ to be deduced. With the *BABAR* result included the new value is

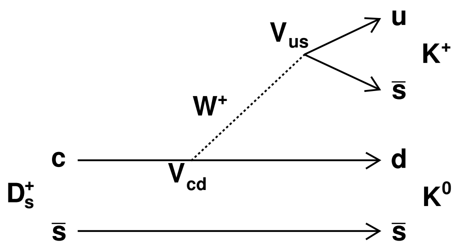


(a) Colour allowed.

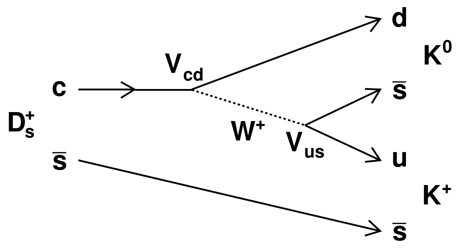


(b) Colour suppressed.

**Figure** 1.4: Leading order Feynman diagrams for the DCS decay $D_s^+ \rightarrow K^+K^0$.

$$\mathcal{B}(D_s^+ \rightarrow K^+\overline{K}^0) = (4.4 \pm 0.9) \times 10^{-2}. \tag{1.30}$$

A potential complication is that the $D_s$ can also decay via $D_s^+ \rightarrow K^+K^0$. This final state will be indistinguishable from that of $D_s^+ \rightarrow K^+\overline{K}^0$ and hence they will interfere, potentially changing the decay rates to $K_S^0$ and $K_L^0$. However, $D_s^+ \rightarrow K^+K^0$ is a doubly Cabibbo suppressed decay as indicated by the $V_{CKM}$ elements appearing in figure 1.4. Given the significant suppression of this channel (with respect to $D_s^+ \rightarrow K^+\overline{K}^0$) it is decided that the effects of ignoring it are negligible for the analysis presented here. Hence, the rate for $D_s^+ \rightarrow K^+K_S^0$ is assumed to be simply half that of $D_s^+ \rightarrow K^+\overline{K}^0$.

# Chapter 2

# The *BABAR* Detector and PEP-II $B$ Factory

The Stanford Linear Accelerator Centre (SLAC) is home to the *BABAR* experiment [33] and the PEP-II $B$ Factory [34], which facilitates the collisions of electrons and positrons. With a design operating luminosity of $3 \times 10^{33}$ cm$^{-2}$s$^{-1}$, PEP-II is an asymmetric $e^+e^-$ collider operating at a centre of mass energy equal to the mass of the $\Upsilon(4S)$ resonance, 10.58 GeV. A 9.0 GeV electron beam and a 3.1 GeV positron beam, travelling in opposite directions, are collided giving the $\Upsilon(4S)$ a Lorentz boost of $\beta\gamma = 0.56$. This enables *BABAR* to fulfil its primary physics goal of studying $CP$-violating asymmetries in the decay of neutral $B$ mesons to $CP$ eigenstates. The high luminosity that PEP-II provides also allows the precise measurement of bottom and charm meson decays and $\tau$ lepton decays, as well as searches for rare processes. A full discussion of the physics available at a $3 \times 10^{33}$ cm$^{-2}$s$^{-1}$ $B$ factory can be found in the *BABAR* Physics Book [35] while the primary physics goals are outlined in the Letter of Intent [36].

## 2.1 The PEP-II $B$ Factory

The PEP-II $e^+e^-$ storage system, operating at the $\Upsilon(4S)$ resonance, has surpassed its design goals to deliver sustained instantaneous luminosities upwards of $1 \times$

$10^{34}$ cm$^{-2}$s$^{-1}$. The time-integrated luminosity has also exceeded design specifications due to the machine's ability to maintain stable beam conditions over significant periods of time. The design and operation of PEP-II are described in greater detail elsewhere [37, 38]. In addition to the on-resonance data, approximately 12% of the running time is used to gather off-resonance data at a centre of mass energy 40 MeV lower than the $\Upsilon(4S)$ resonance for the purpose of non-resonant background studies.

### 2.1.1 Interaction Region

The $e^+$ and $e^-$ bunches collide head on at the interaction point (IP) inside a double walled beryllium beam pipe of outer radius 27.9 mm. The inner and outer pipes, with thicknesses of 0.83 mm and 0.53 mm respectively, are cooled by water flowing between them through a 1.48 mm thick channel. The inner surface is thinly coated with gold, and the pipe is wrapped in tantalum foil (in regions not near the IP) in efforts to reduce the impact of synchrotron radiation. At normal incidence the pipe represents $0.0106X_0$, where $X_0$ is one radiation length.

A pair of dipole magnets (B1) and a series of offset quadrupoles (Q1), both permanent samarium-cobalt magnets, separate the bunches in the horizontal plane of the IR. The B1 dipoles are positioned at $\pm 21$ cm along $z$ with respect to the IP and, along with the Q1 quadrupoles, are located inside the *BABAR* solenoidal field. Neither of the beam trajectories are parallel to the solenoidal field within the interaction region which results in both trajectories being perturbed. Generally, the perturbation is larger for the low energy beam. Although unavoidable, perturbations of the beam momenta can be minimised by offsetting the beam collision axis by $\sim$20 mrad in the horizontal plane with respect to the $z$-axis [39, 40], which is defined by the central Drift Chamber axis.

### 2.1.2 Trickle-Charge Operation

PEP-II used to operate (before June 2003) on a 40-50 minute fill cycle where the low energy ring (LER) and high energy ring (HER) are injected with charge for approximately 15 minutes. When the beam current has degraded sufficiently, data-taking temporarily stops while the beams are refilled once again. PEP-II has since upgraded to a trickle-charge operational mode, where the beam currents are maintained using a pulsed injection technique [41]. The primary concern with this approach is the increase in radiation dose delivered to the detector components due to the continuous injection of charge into the machine.

Trickle-charging of the LER only, where the stored beam lifetime is lower, yields an increase in delivered luminosity of $\sim 35\%$. With both the LER and HER operating in trickle-charge mode a further 12% is added. The upgrade culminates in a significant increase in the delivered time-integrated luminosity: the average-to-peak luminosity ratio has increased from $\sim 0.72$ to between $0.99 - 1.00$.

### 2.1.3 Beam Properties

Analyses at *BABAR* require the accurate monitoring of several machine parameters: luminosity, beam energies (LER and HER) and position and size of the IR. Both the luminosity and the beam direction are measured by *BABAR* using QED processes such as $e^+e^- \to e^+e^-$ and $e^+e^- \to \mu^+\mu^-$. Luminosity measurements are stable as a function of time with a statistical uncertainty of less than 1% for a 1 fb$^{-1}$ sample of data. The beam direction is measured on a run by run basis with a 1 mrad error associated with the boost direction from the laboratory to the centre of mass (c.m.) frame. A run is defined within the experiment as a period of stable data taking with a duration of 3 hours or less and is how *BABAR* data are divided.

Beam energy measurements are crucial in determining powerful variables for signal and background discrimination in $B$ and $D$ meson decays. For the purposes of the analysis presented in this thesis, the kinematic variable $x_p$, representing the normalised momentum of the $D_s^*$ meson, is an excellent discriminant against $D_s^*$ mesons that originate from $B$ decays. The beam energy is determined from the total magnetic bending strength resulting in r.m.s. energy spreads of 2.3 MeV and 5.5 MeV for the LER and HER respectively [33].

The position of the luminous region is vital for time-dependent analyses and thus critical to the primary physics goal of *BABAR*. In reconstructing two-track events the distance of closest approach of the tracks to the $z$-axis is measured as a function of the azimuthal angle $\phi$. This relationship is analysed for many events to determine the transverse position and size of the luminous region with an uncertainty of a few $\mu$m [33]. The vertex distribution of the two tracks is used to determine the longitudinal properties with an error of the order of 100 $\mu$m. The vertical size is too small to measure directly and is inferred from the luminosity, horizontal size and beam current measurements with a variation of $\sim 1 - 2\,\mu$m. All beam parameters are stable over the course of a single run.

### 2.1.4 Beam-Generated Backgrounds

For all physics analyses, the major causes of backgrounds during stable running of the machine are synchrotron radiation near the IR, beam-gas collisions in the evacuated beam pipe and electromagnetic showers caused by Bhabha scattering where the stray electron or positron hits material within a few metres of the IR [42, 43].

Collisions between the beam and the residual gas molecules in the beam pipe are proportional in rate to the product of the beam current and the residual pressure. During the operation of *BABAR* the rate has decreased due to scrubbing of the evacuated pipe by synchrotron radiation. Although the pressure in both the LER and HER has dropped below design, beam-gas scattering is still the primary cause of radiation damage for the Silicon Vertex Tracker (SVT).

Beam-generated backgrounds have implications for the operational state of detector components and thus the quality of any data that are recorded by the experiment. To avoid resolution degradation and losses in efficiency the backgrounds are carefully and continuously monitored. Thresholds are imposed for each subsystem, with the SVT, Drift Chamber (DCH) and Electromagnetic Calorimeter (EMC) having the ability to abort the beams should the background levels become dangerously high.

This is achieved through the strategic placement of PIN diodes positioned around the detector volume; their dark currents are proportional to the radiation dose.

### 2.1.5 Summary

PEP-II provides excellent luminosities for the *BABAR* experiment, in excess of design specifications. The current mode of operation sees the peak luminosity sustained for long periods of time with stable conditions and safe background levels. Current plans exist to upgrade the luminosity to around $1.5 \times 10^{34}$ cm$^{-2}$s$^{-1}$. This goal has implications for all detector sub-systems due to the increased occupancy, and the trigger system where rates will increase and likely exceed 2 kHz.

## 2.2 The *BABAR* Detector

Comparing time-dependent decay rates of neutral $B$ mesons to self conjugate states is a crucial test of $CP$ invariance. It is necessary to fully reconstruct one of the $B$ mesons while tagging the other $B$ meson from the identification of its decay products, involving the detection of two or more tracks plus multiple $\pi^0$ mesons. This primary physics goal places the most stringent requirements upon the detector design, which should incorporate

- a large, uniform acceptance;
- good vertex resolution and excellent detection efficiency for charged tracks down to momenta of 60 MeV/$c$;
- good energy and angular resolution for photons from $\pi^0$, $\eta$ and radiative decays in the energy range 20 MeV-4 GeV;
- excellent momentum resolution for signal and background discrimination;
- efficient particle identification for $e/\mu/\pi/K/p$ for purposes of flavour tagging and reconstruction of exclusive states;

- an open trigger system in combination with a high bandwidth data-acquisition system;
- detector components that are radiation hard for the projected lifetime of the experiment along with detailed monitoring; and
- an online computing system capable of processing and storing the large amount of data output by the trigger.

### 2.2.1 Design Overview

The *BABAR* detector's design and construction is the work of a large team of international scientists and engineers. Details of the original design can be found in the Technical Design Report [44]. *BABAR* is a nested set of sub-systems surrounding the PEP-II interaction region. The detector's position is offset by 0.37 m along the $z$-axis (in the direction of the positron beam) relative to the $e^+e^-$ interaction point (IP). This maximises the geometrical acceptance of the $\Upsilon(4S)$ decay products. Longitudinal and transverse schematic representations of *BABAR* can be seen in figures 2.1 and 2.2 respectively.

A silicon vertex tracker sits closest to the IP within the support tube which is surrounded by a drift chamber. Together they supply the angle and momentum measurements for charged tracks, and particle identification at low momentum through ionisation energy loss ($dE/dx$) measurements. Surrounding the tracking system is a ring-imaging Čerenkov detector for flavour tagging and then an electromagnetic calorimeter. All these detector components are enclosed by a superconducting solenoid generating a 1.5 T magnetic field to faciliate momentum measurements and separation of oppositely charged tracks. An instrumented flux return for the magnet makes up the bulk of the outer detector, providing both a neutral hadron and muon detector and structural support for the other sub-systems.

The *BABAR* co-ordinate system is defined by the drift chamber. The positive $z$-axis points approximately along the direction of the electron beam and is defined as the

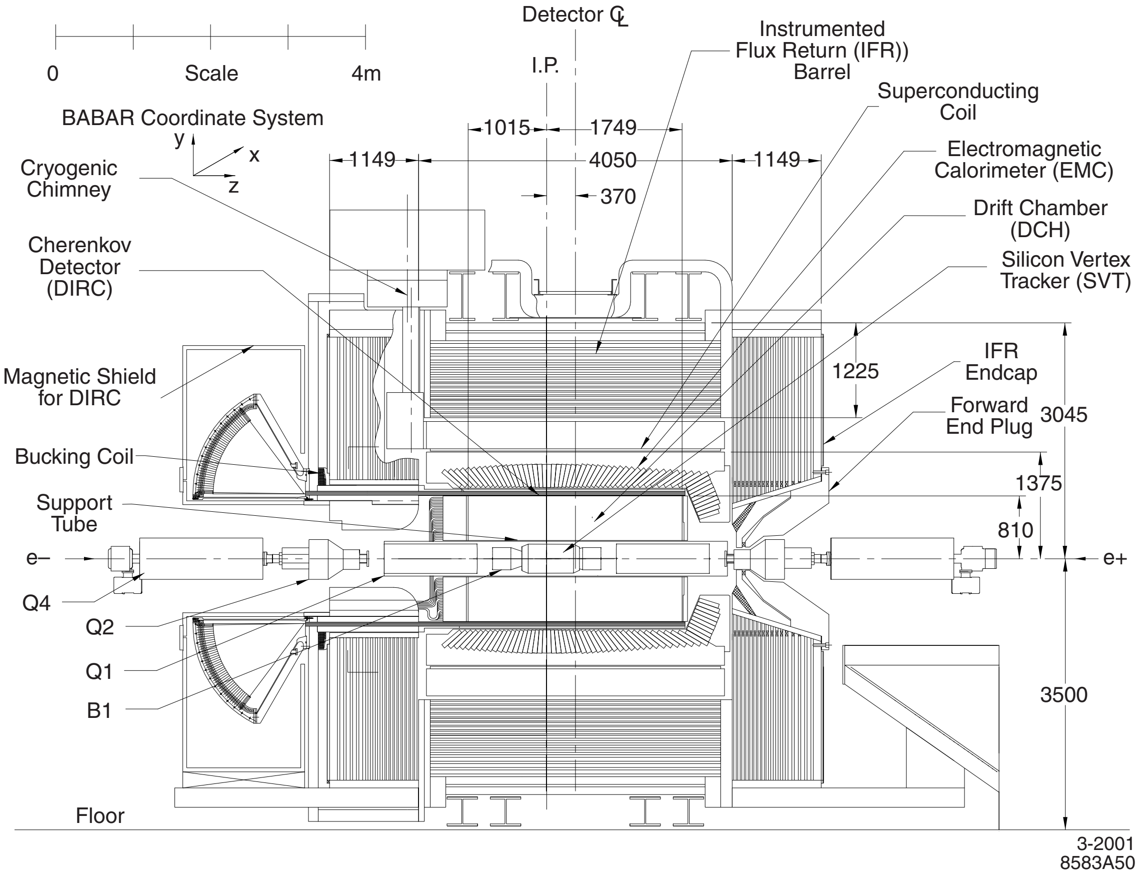


**Figure** 2.1: Longitudinal section schematic of the *BABAR* detector.

cylindrical drift chamber's axis of rotation. The positive $y$ and $x$ axes point upwards and laterally away from the PEP-II ring centre respectively.

Compact in design, the detector's radial dimension was constrained by the PEP-II beam pipe being 3.5 m above the floor. The physics performance and detector cost had to be balanced when choosing the dimensions of the sub-systems. The calorimeter was the most expensive system and as such its volume was kept to a minimum while not significantly degrading the performance of the tracking system. Furthermore, material between each detector sub-system and the IR was minimised in terms of radiation lengths such that resolution was not unnecessarily compromised (figure 2.3).

A detailed description follows for each of the sub-detectors, the trigger and data acquisition system.

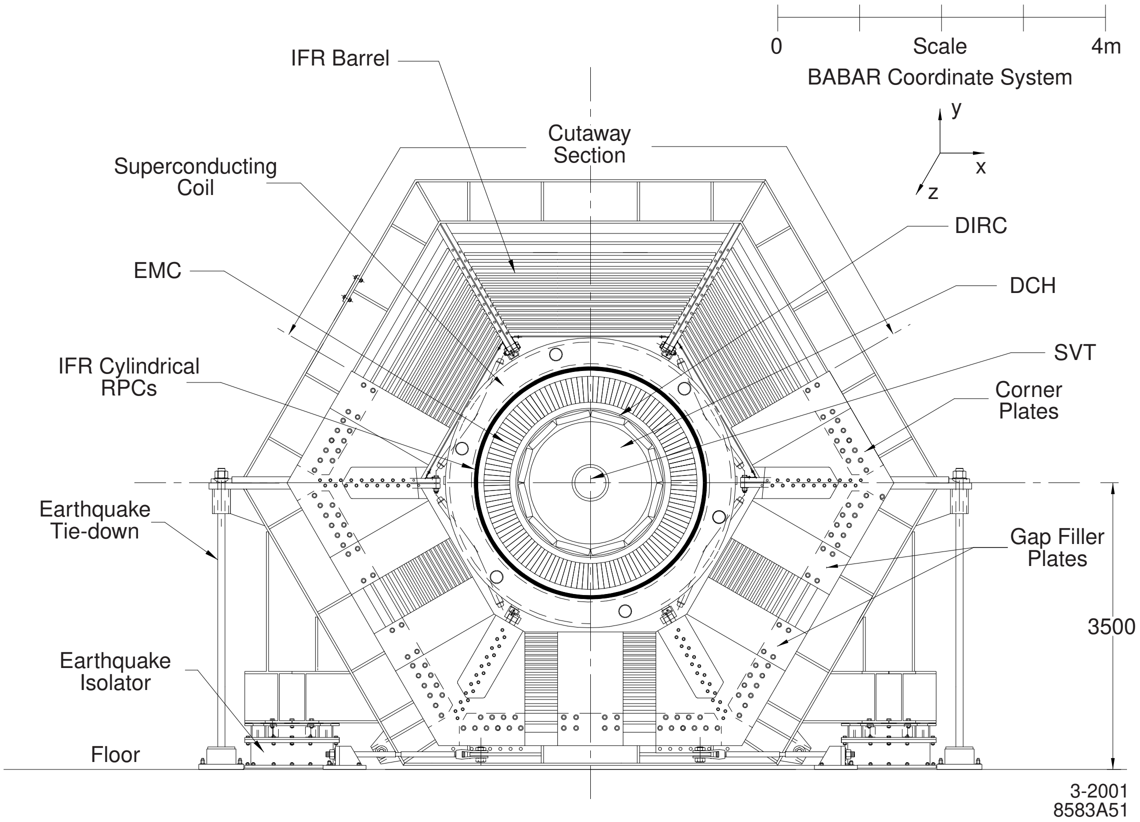


**Figure** 2.2: Transverse section schematic of the *BABAR* detector.

## 2.3 Silicon Vertex Tracker

The Silicon Vertex Tracker (SVT) sits at the centre of the *BABAR* detector near the interaction region (IR). It is one of the two charged particle tracking systems of *BABAR*, the other being the DCH which is detailed in section 2.4. To satisfy the physics goals of the experiment, reconstructing multiple decay vertices of weakly decaying $B$ and $D$ mesons is vital. The SVT is designed to detect charged particles efficiently and take precise measurements of their momenta and angles. The extent to which the SVT accomplishes these requirements has a direct impact on enhancing signal over background and hence the precision of any measurement the experiment makes.

In a wider experimental context, the tracking system measurements allow extrapolation of the tracks to the Detector of Internally Reflected Čerenkov light (DIRC),

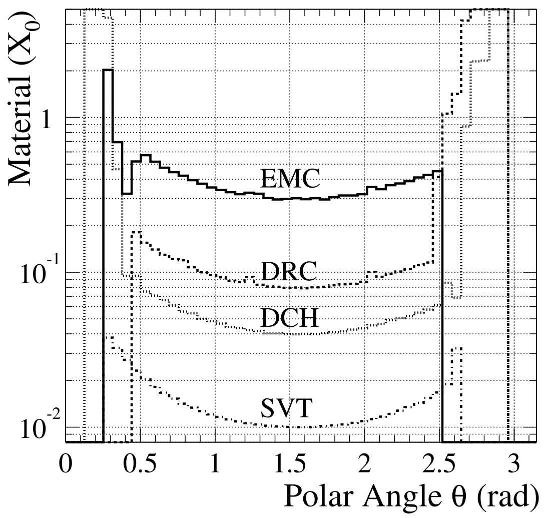


**Figure** 2.3: The radiation lengths of material a high energy particle traverses as a function of polar angle, $\theta$. The track is assumed to originate at the centre of the *BABAR* co-ordinate system.

EMC and Instrumented Flux Return (IFR). Errors on measured track parameters feed directly into the uncertainty of Čerenkov angle measurements at the DIRC. Therefore the SVT and DCH measurements should combine to give a small error compared to the average observed at the DIRC. The tracking systems complement each other in fulfilling all design requirements over a large momentum range, with the DCH more important at lower momenta and the SVT measurements dominating at higher momenta. The exception to this general rule is for tracks below the DCH threshold momentum of 90 MeV/$c$ where only SVT measurements are possible.

### 2.3.1 Design Constraints and Requirements

The driving factors behind the SVT design are requirements arising from experimental physics goals and the constraints introduced by the *BABAR* detector and the interaction region.

Maximising angular coverage is crucial which leads to the SVT being situated inside the support tube, where it can reach down to within 350 mrad in $\theta$ (polar angle) of the beam line in the forward region and within 525 mrad in the backward. This design asymmetry is a direct reflection of the Lorentz boost introduced by PEP-II. Further coverage is not possible due to the presence of the B1 and Q1 magnets near the IR.

Lying at the centre of *BABAR*, the SVT is designed to operate in the 1.5 T solenoidal field and withstand an integrated radiation dose of up to 2 MRad. PEP-II's environmental constraints necessitate cooling to transport the heat generated by the read-out electronics away from the IR. Access to the SVT, for reparation purposes or otherwise, is not possible during normal detector operations leading to timescales for upgrades or repairs averaging ~4 months. Therefore all instrumentation lying within the confines of the support tube must be both durable and reliable. This leads to redundancy being incorporated into the design.

Once the SVT is assembled the relative motion of the individual silicon sensors must be kept to a minimum to ensure optimal position resolution over long periods of time. However, the global position with respect to the *BABAR* co-ordinate system, as defined by the DCH, can change by $\pm 100\ \mu$m over several weeks. Rolling calibrations, taken on a run-by-run basis, measure three translations and three rotations to correct for these positional shifts ensuring track reconstruction is performed with the most current global alignment constants. During a single run, the global positional change is usually small compared to the beam dimensions.

Time-dependent $CP$ asymmetry measurements require a mean vertex resolution better than 80 $\mu$m along the $z$-axis for a fully reconstructed $B$ decay. By delivering this accuracy the SVT avoids its resolution having a significant impact on the $CP$ asymmetry measurements. The required reconstruction of final states in $B$ decays (and $\tau$ and charm decays) demands a resolution in the $x$-$y$ plane of order $\sim 100\ \mu$m. This is compared with, for example, the $\sim 275\,\mu$m separation of the two $D$ mesons in the decay $B^0 \to D^+D^-$.

A feature of $B$ meson decays is the typically low $p_t$ of the decay products. Tracks with transverse momentum less than 120 MeV/$c$ cannot be measured reliably in the

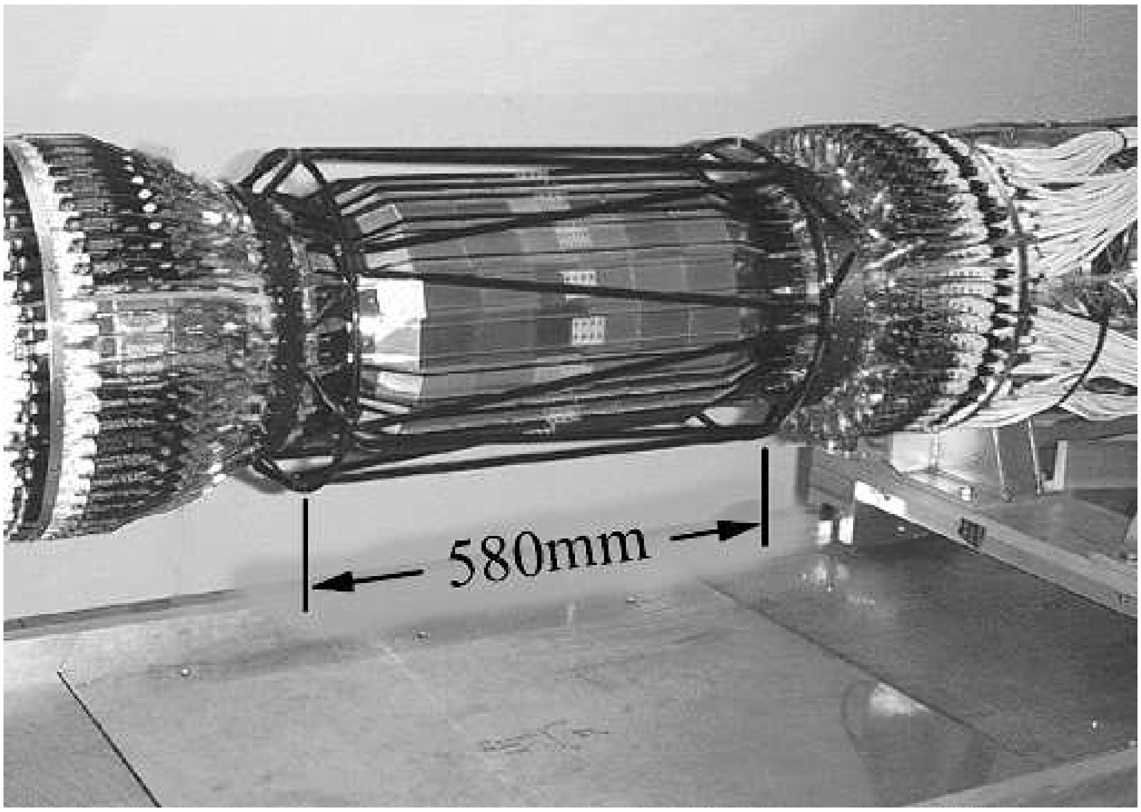


**Figure** 2.4: Fully assembled SVT. The carbon-fibre support frame (black structure) surrounds the silicon sensors, of which the outer layer is visible.

DCH alone. The SVT is required to perform this task, such that slow pions from $D^*$ meson decays can be identified. The momentum range must extend down to 50 MeV/$c$. The necessity for both standalone SVT tracking and matching tracks with those measured in the DCH is a crucial factor in determining the number of tracking layers in the SVT.

Extending further from the IR, the SVT is key in achieving the design resolution, of order 1 mrad, for Čerenkov angle measurements in the DIRC. It does this by making precise measurements of track angles and is particularly important for high momentum tracks.

The various design constraints and desired attributes discussed here have culminated in a five layer SVT. Each layer comprises double-sided silicon strip sensors, providing a spatial resolution of $10 - 15\,\mu$m for perpendicular tracks in the inner three layers,

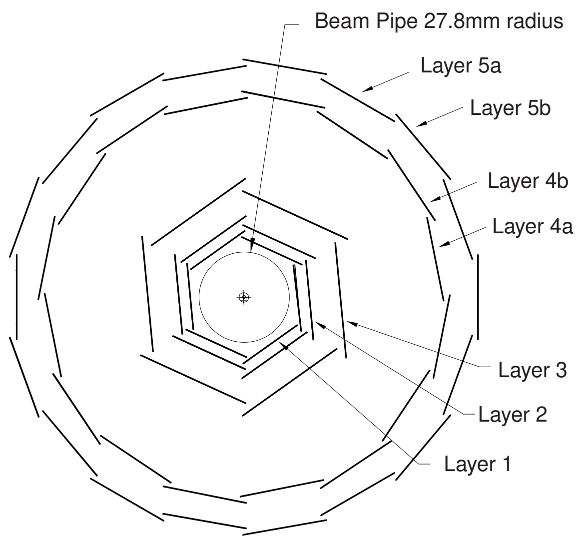


**Figure** 2.5: Transverse section schematic of the SVT depicting the relative positions of each module.

and $\sim 40\,\mu$m in the two outer layers. Generally, impact parameter measurements are supplied by the inner three layers, while pattern recognition and low $p_t$ tracking are predominantly performed by the outer two.

### 2.3.2 Structural Details

A photograph of the fully constructed SVT is shown in figure 2.4. Physically supporting the SVT is a carbon-fibre space frame, with individual modules given rigidity through two carbon-fibre ribs running along their length.

Each layer of the SVT is divided into a number of modules, arranged as depicted in figure 2.5. The inner three layers contain 6 modules each while layers 4 and 5 comprise 16 and 18 modules respectively. The $300\,\mu$m thick, double-sided silicon strip sensors [45] on each module are oriented orthogonally to one another, either in parallel with the beam axis ($\phi$ strips) or perpendicular to it ($z$ strips). Modules of the inner layers are tilted by $5^\circ$ in $\phi$ allowing adjacent ones to overlap and provide full azimuthal coverage. A similar result is achieved by dividing each outer layer into two sub-layers.

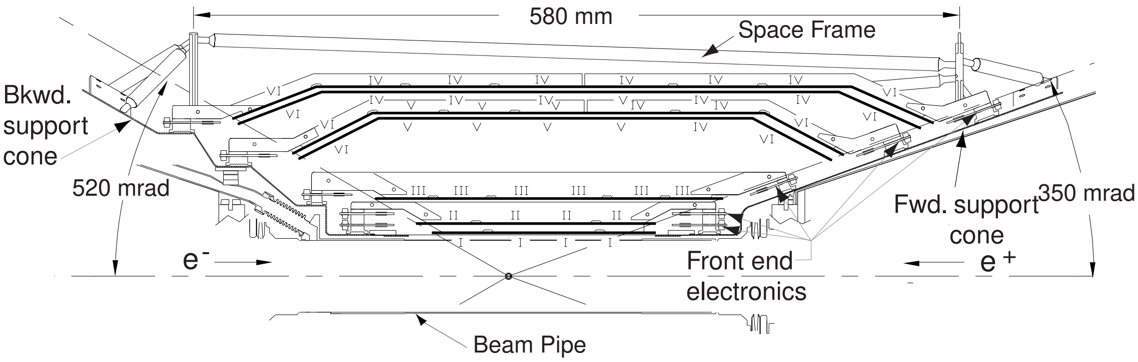


**Figure** 2.6: Longitudinal section schematic of the SVT showing the acceptance range and arched outer layer design.

The 0.96 m$^2$ active area covers approximately 90% of the solid angle in the c.m. frame, with typically 86% contributing to tracking. Particles traverse $\sim$ 4% of a radiation length when passing through the SVT. Limiting the amount of material in the acceptance region is achieved by locating the readout electronics outside the active detector volume. In the forward region this leaves only the 10 mm of space between the SVT acceptance boundary and the B1 magnet.

In addition to having more modules the outer two layers have an arched design, whereas the inner three are flat (figure 2.6). This serves two purposes: firstly, the amount of silicon required to cover the solid angle is minimised and more importantly, the crossing angle of particles near the acceptance edges is increased thereby reducing multiple scattering.

### 2.3.3 Front End Electronics

Several requirements drive the design of the SVT custom input/output computer, the ATOM [46] (A Time-Over-Threshold Machine), it should

- retain signals from all strips with the number of transmitted hits kept to a minimum. A hit is defined as a deposited charge > 0.95 fC which corresponds to 0.25 MIP (a Minimum Ionising Particle signal);

- have a signal-to-noise ratio > 15 for MIP signals for all modules;
- have the ability to accept random triggers;
- be able to sustain an integrated radiation dose > 2.5 MRad; and
- be compact: fit 128 channels into a 6.2 mm-wide chip.

The ATOM monitors the potential difference across a sensor and when this rises above a pre-determined threshold value it measures the time taken for the voltage to return below the threshold. Thie enables ionisation energy loss, $dE/dx$, to be measured in each SVT sensor.

The double-sided design enables up to 10 $dE/dx$ measurements to be made per track. A 60% truncated mean $dE/dx$ is calculated for each track with signals from at least 4 sensors. A resolution of $\sim$ 14% on the truncated $dE/dx$ mean is achieved for MIPs with approximately $2\sigma$ of separation between pions and kaons up to momenta of 500 MeV/$c$ and above 1 GeV/$c$.

The SVT data transmission and DAQ systems are described in detail elsewhere [47, 48].

### 2.3.4 Performance and Summary

The SVT has successfully operated in *BABAR* since its installation in 1999. Currently $\sim$ 95% of the readout electronics are operational with only 4 of the 208 readout sections not working. However, these non-functional sections were damaged during the installation procedure and not as a result of operation.

Measured hit reconstruction efficiencies for each of the half-modules can be seen in figure 2.7. The average efficiency is 97% over all half modules. For slow pions

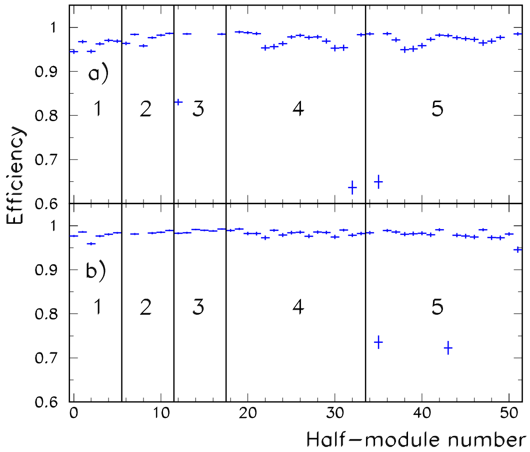


**Figure** 2.7: Hit reconstruction efficiency for a) forward and b) backward SVT half-modules. The horizontal axis marks the different modules with the vertical lines depicting layer boundaries. A missing data point denotes a non-functioning half-module.

this efficiency is $> 70\%$ for $p_T > 50$ MeV/$c$. Depending on the track angle, a hit resolution of $10 - 14$ $\mu$m is achieved.

The radiation budget of 2 MRad has been exceeded and no change has been observed in hit reconstruction efficiencies and resolutions as a result. The revised target is now 5 MRad. Studies are ongoing to determine the result of further radiation damage, with the signal-to-noise ratio expected to drop to 10 for readout sensors after 5 MRad.

The SVT is expected to continue functioning well until the end of the decade, with only slightly reduced physics performance in all realistic damage scenarios.

## 2.4 Drift Chamber

As part of the *BABAR* charged particle tracking system, the primary objective of the DCH is to detect charged particles efficiently and make precise measurements of their angles and momenta [49,50]. Together with the complementary SVT measurements, the DCH enables the reconstruction of exclusive $B$ and $D$ meson decays with minimal background. Of particular importance are the DCH measurements of low momentum tracks since they dominate the errors when extrapolating charged tracks to the DIRC, EMC and IFR.

### 2.4.1 Design Constraints and Requirements

A key requirement of the DCH is the ability to reconstruct vertices outside the volume of the SVT. For example, this is critical for the reconstruction of the reference mode chosen for the study reported in this thesis: $D_s^{\pm} \to h^{\pm} K_s^0$, where $h$ is either a pion or a kaon, followed by $K_s^0 \to \pi^+\pi^-$. The short-lived neutral kaon passes undetected through the SVT and decays predominantly in the DCH volume. In addition to transverse momenta and positions, the DCH must measure longitudinal track position with a resolution of $\sim 1$ mm.

The *BABAR* charged particle trigger requires information from the DCH for event acceptance or rejection. The time jitter for this cannot exceed 0.5 $\mu$s.

Particle Identification (PID) is a responsibility of the DCH at low momenta. By measuring the ionisation energy loss, $dE/dx$, with a resolution of 7%, pions and kaons can be separated up to momenta of 700 MeV/$c$. This is complementary to the DIRC where separation is best at high momentum. Furthermore, the DCH has a larger angular acceptance than the DIRC, providing the only PID information in the extreme forward and backward directions.

Uncertainty on track parameter measurements is dominated by multiple scattering due to the average momenta of $B$ and $D$ meson decay products being less than 1 GeV/$c$. This effect is reduced by minimising the material occupying the space in front of and inside the DCH volume. In addition to improved track resolution for high momentum tracks, the ability to match tracks in the SVT and DCH is increased. A thin outer wall minimises any detrimental effects affecting DIRC and EMC performance.

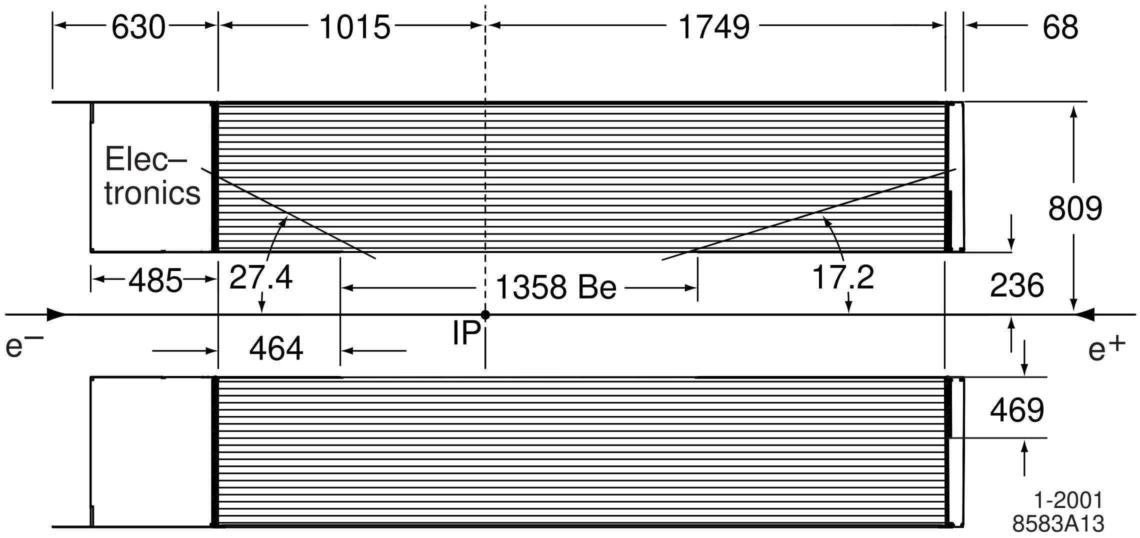


**Figure** 2.8: Longitudinal cross section schematic of the DCH. Due to the Lorentz boost, the DCH is centred 370 mm downstream from the interation point.

The DCH must fulfil all the above requirements while operating in the 1.5 T solenoidal field and in the presence of significant beam-generated backgrounds.

### 2.4.2 Structural Details

The DCH is a 40 layer chamber of small hexagonal cells and almost 3 m in length. A longitudinal cross-section can be seen in figure 2.8. Above a threshold momentum of 180 MeV/$c$, up to 40 spatial and $dE/dx$ measurements are taken for charged particles traversing the chamber. The 3-dimensional positioning is determined by tilting 24 of the layers slightly with respect to the $z$-axis.

In an effort to reduce multiple scattering further, aluminium field wires are chosen together with a helium based gas. A helium and isobutane mixture is chosen in a ratio of 4:1 (helium:isobutane), resulting in a radiation length five times longer than found in more commonly used argon-based mixtures. Hence with a smaller Lorentz angle, the spatial resolution is improved due to the more uniform time-distance relationship. Together with a lightweight, beryllium inner wall and carbon-fibre composite outer wall, the DCH has a total thickness of 0.0108 $X_0$.

Bounding the DCH on its inner and outer surfaces are the support tube and the DIRC respectively. The asymmetric positioning with respect to the IR and the chosen dimensions ensure that particles will traverse at least half the layers within the polar angle region, $17.2° < \theta < 152.6°$. Good angular coverage for forward going tracks is important to attain the maximum achievable invariant mass resolution.

The DCH's cylindrical layers comprise 7,104 hexagonally shaped drift cells. Each set of 4 layers forms a superlayer, within which the number of cells and wire orientation is the same for all layers. Non-tilted and tilted superlayers (with respect to the $z$-axis) are referred to as axial and stereo respectively. A schematic view of cell arrangement is shown in figure 2.9.

Specifications for all wires in the chamber are detailed in table 2.1. The tungsten-rhenium sense wires [51] offer a low enough linear resistivity of 290 $\Omega\mathrm{m}^{-1}$ while being strong with an excellent surface quality. The aluminium field wires have a far higher tension to match the gravitational sag of the sense wires, 200 $\mu$m at mid length, and ensure the sense wires are tensioned well below their elastic limit.

**Table** 2.1: DCH wire specifications.

| Type | Material | Diameter ($\mu$m) | Voltage (V) | Tension (g) |
|---|---|---|---|---|
| Sense | W-Re | 20 | 1930 | 30 |
| Field | Al | 120 | 0 | 155 |
| Guard | Al | 80 | 340 | 74 |
| Clearing | Al | 120 | 825 | 155 |

### 2.4.3 Front End Electronics

There is space at the rear of the DCH to house the front end electronics [52]. This design minimises material in the forward region that would obscure the calorimeter endcap. However, cell dimensions are small and access is difficult through the DIRC central support tube requiring a high-density of electronics components.

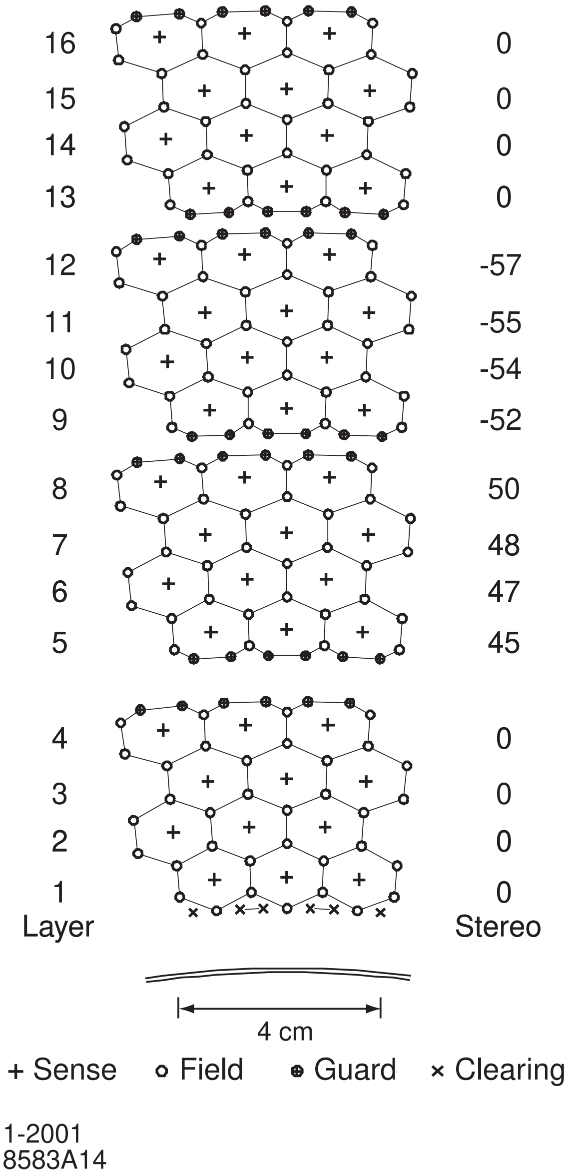


**Figure** 2.9: A schematic view of the drift cell arrangement for the innermost 16 layers (4 superlayers). The approximate cell dimensions are 11.9 mm by 19.0 mm in the radial and azimuthal directions respectively. Most cells consist of a single sense wire surrounded by 6 field wires. The stereo angle of the sense wires is shown in mrad by the column of numbers on the right hand side.

The electronic system is designed to measure the drift-time and the integrated charge. Additionally it must supply a single bit to the trigger system for each wire with a signal. Achieving a position resolution of 140 $\mu$m averaged over all cells and a 7% resolution for $dE/dx$ measurements drives the design of the electronics. In total, 28 optical fibres are required to transfer all the data to the readout system.

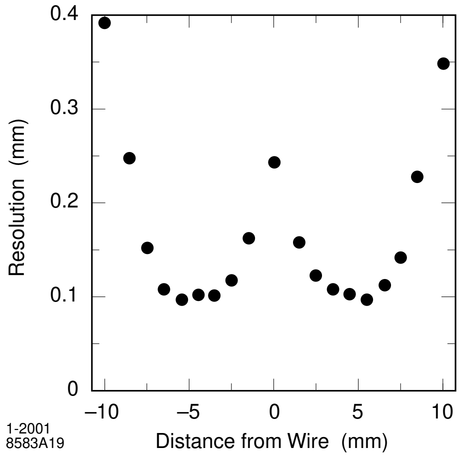


**Figure** 2.10: Position resolution of the DCH as a function of drift distance.

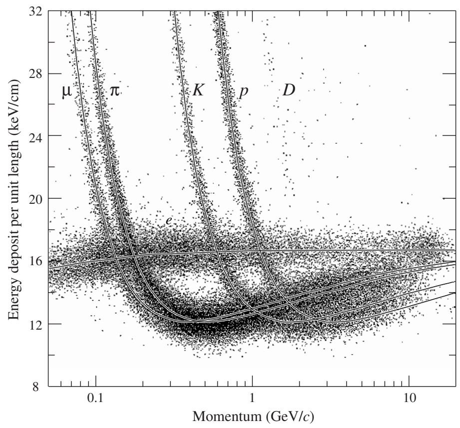


**Figure** 2.11: Ionisation energy loss for different mass particles.

### 2.4.4 Performance and Summary

Drift distances in the chamber are measured by determining the distance of closest approach between the track and the wire. Bias is avoided by excluding the hit on the wire under consideration from the fit. These estimates are subsequently averaged over all wires in a layer. A time-to-distance relation (between drift time and drift distance) is obtained using samples of $e^+e^-$ and $\mu^+\mu^-$ events. Position resolution as a function of drift distance can be seen in figure 2.10.

Ionisation energy loss for charged particles traversing the chamber, $dE/dx$, is derived through measuring the total charge deposited in each drift cell. A truncated mean is computed from the lowest 80% of $dE/dx$ measurements for each track, yielding the specific energy loss. Particles of different masses are distinguished by comparing the $dE/dx$ measurements taken in the chamber to the Bethe-Bloch predictions (figure 2.11). The measured r.m.s. resolution is found to be typically 7.5% when examining Bhabha scattering events.

Performance is close to design specification. A small number of wires are damaged as a result of an accident during the commissioning phase of installation, but otherwise all cells are fully operational. Both position and $dE/dx$ design resolutions are met.

## 2.5 Detector of Internally Reflected Čerenkov Light

The primary purpose of the Detector of Internally Reflected Čerenkov Light (DIRC) is to provide flavour tagging and thus enable *BABAR* to achieve its primary physics goal. It enables flavour tagging of the $B$ meson through the $b \to c \to s$ cascade decay. A full reconstruction of the second $B$ meson allows the study of $CP$-violation in the $b$ sector. Furthermore, the study of rare, hadronic, two-body decays, such as $D_s^+ \to K^+\pi^0$ and $D_s^+ \to \pi^+\pi^0$, requires good separation of charged $K$ and $\pi$ mesons. The DIRC must provide PID for particles from the pion Čerenkov threshold momentum up to 4.2 GeV/$c$, and as a result is complementary to the PID provided by the DCH $dE/dx$ measurements.

### 2.5.1 Conception and Design

The DIRC is a novel, ring-imaging Čerenkov detector [53]. It operates on the principle that the angles of incidence and reflection are equal for a photon reflecting at a flat surface. Photons produced in the radiator (the medium in which Čerenkov radiation is produced) remain trapped inside through total internal reflection. The Čerenkov angle, $\theta_c$, is determined through the equation $\cos\theta_c = 1/n\beta$, where $n$ denotes the refractive index of the radiator and $\beta = v/c$ ($v$ = velocity of the particle, $c$ = velocity of light in a vacuum).

Several key requirements must be satisfied by the design. In order to meet expectations the DIRC should possess the following attributes:

- a thin and uniform active volume, with regard to radiation lengths, to minimize impact on the electromagnetic calorimeter energy resolution;
- minimal radial thickness to avoid an increase in expense of the calorimeter;
- fast PID system signal response;
- tolerance of large backgrounds; and

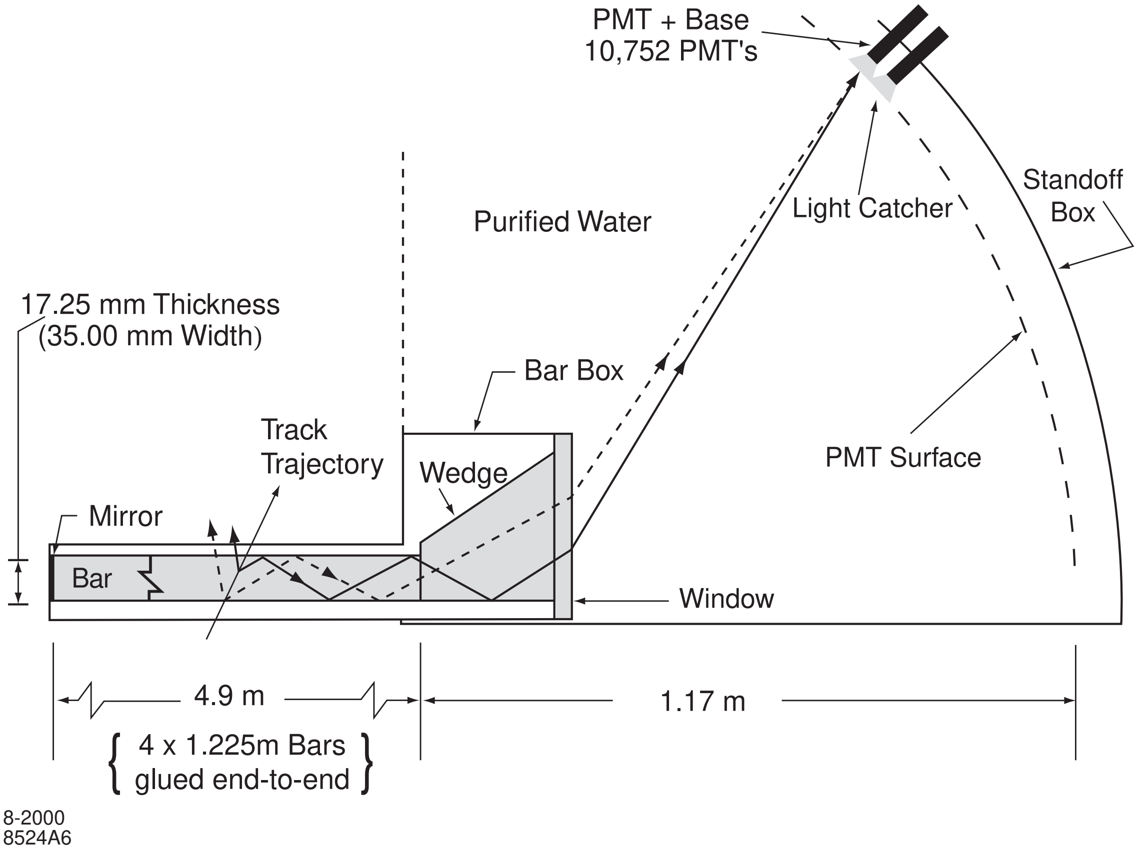


**Figure** 2.12: Schematic representation of the DIRC system.

- $K/\pi$ separation greater than $\sim 4\sigma$ over the momentum range.

### 2.5.2 Structural Details

The DIRC radiator material is a synthetic, fused silica (Spectrosil [54]) formed into long, thin bars of rectangular cross-section. Spectrosil is chosen due to its long attenuation length, large refractive index ($n = 1.473$), low chromatic dispersion and excellent optical surface quality. Each bar is 17 mm thick, 35 mm wide, and comprises four 1.225 m long bars glued end-to-end giving a total length of 4.9 m.

The bars are placed inside twelve hermetically sealed containers (bar boxes), with each box holding twelve bars to give a total of 144 bars, and arranged into a 12-sided barrel. The bars common to a single box are separated optically from one another by

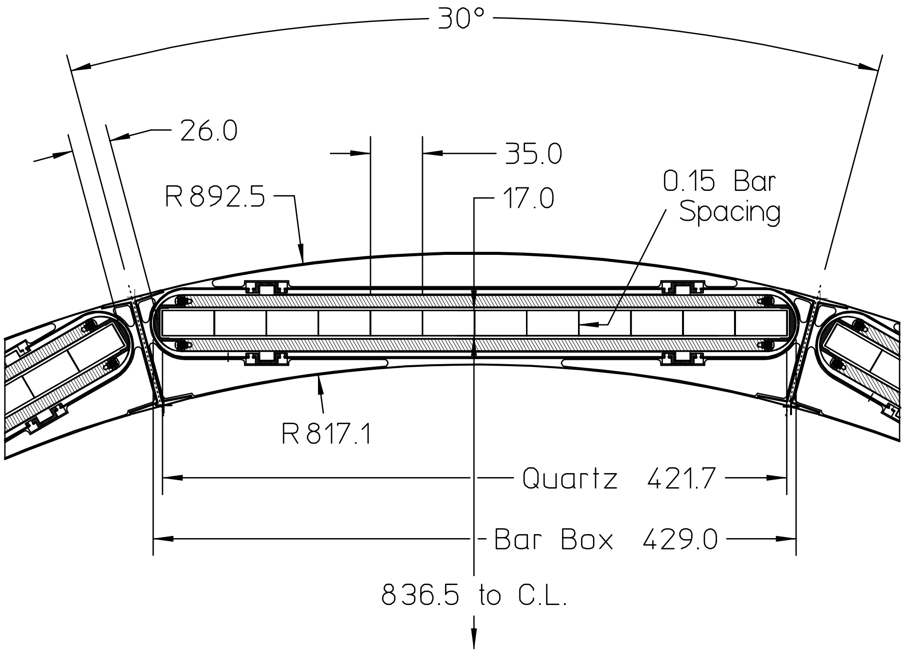


**Figure** 2.13: A transverse schematic of the DIRC radiator bars embedded within the Central Support Tube. All dimensions are in mm.

a ~150 $\mu$m air gap. All boxes are supported within an aluminium Central Support Tube (CST) along the active length of the detector. A schematic of this arrangement is shown in figure 2.13.

Tracks in *BABAR* are produced predominantly in the forward direction due to the energy asymmetry of the beams. Consequently, the DIRC's photon detector is positioned at the backward end such that it does not hinder the performance of other detector systems situated in the forward region. Since instrumentation is positioned solely at one end, a mirror is placed at the forward end of each bar to reflect photons back towards the instrumented end.

Photons produced in the radiator are detected by a densely packed array of 10,752 PMTs [55, 56] (photo-multiplier tubes) located within the standoff box: a large region, filled with purified water, which houses the instrumentation (figure 2.12). Water is chosen because both its refractive index ($n = 1.346$) and its chromaticity are close to that of fused silica, thus minimising total internal reflection and dispersion respectively at the water/silica interface. Furthermore, the $\sim 6,000$ litre quantity required is inexpensive.

Light reaching the instrumented end of a radiator bar meets a fused silica wedge glued to the bar (figure 2.12). The wedge has the effect of reducing the required active surface area in the standoff box and recovering photons that would be lost at the water/silica interface due to total internal reflection. A 10 mm thick fused silica window, common to the twelve wedges in a bar box, provides the seal and interface to the water in the standoff box. The distance between the end of the radiator bars and the PMTs is approximately 1.17 m.

A light catcher cone [57] surrounds each individual PMT to reflect light towards the PMT that would otherwise miss the active surface area. The cones are mounted in front of the PMT photocathodes and achieve a ~90% active surface area.

Including all mechanical supports the DIRC occupies 80 mm of the active detector volume in the radial direction, corresponding to $0.17X_0$ for a track at normal incidence. The radiator bars cover $\sim 94\%$ of the azimuth and $\sim 83\%$ of the polar angle cosine in the c.m. frame.

### 2.5.3 Reconstruction and Readout

The front end electronics (FEE), mounted outside the standoff box, are single photoelectron sensitive and measure the arrival time for each Čerenkov photon detected by a PMT. Three-dimensional imaging is performed by measuring the position and arrival time of PMT signals. Measurements are read for PMTs whose signal times lie within a ±300 ns trigger window. The track position and angles are known from SVT and DCH measurements such that $\theta_c$ and $\phi_c$ (the polar and azimuthal angles of the Čerenkov photon with respect to the track vector) can be determined using the positional knowledge of the radiator bar and PMT.

Signals arriving within the trigger window are used to calculate the set of vectors pointing from the centre of the radiator bar to the centre of each PMT. These vectors are extrapolated into the radiator bar and used to determine $\theta_c$ and $\phi_c$. The timing measurements are useful in suppressing photons resulting from the beam-induced background and for separating photons originating from different tracks in the same event (figure 2.14).

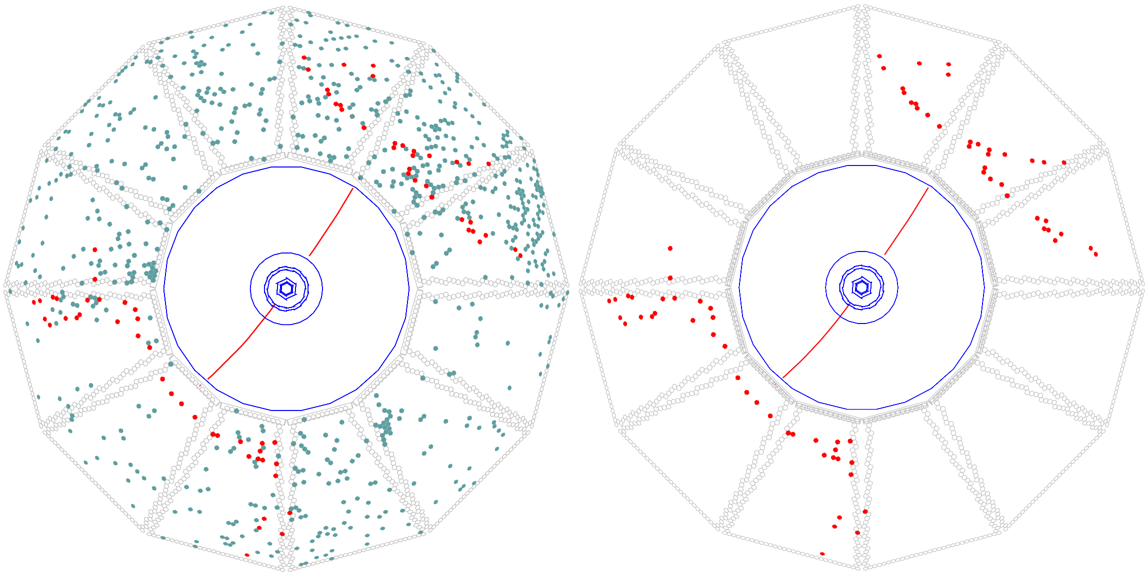

**Figure** 2.14: An $e^+e^- \to \mu^+\mu^-$ event at *BABAR* as seen by the DIRC. On the left, all signals within the ±300 ns trigger window are included. An 8 ns cut has been placed around the expected Čerenkov photon arrival time in the right hand plot. Consequently some 500 background hits have been rejected.

Backgrounds are dominated by photons orignating from the PEP-II machine hitting the standoff box. The signal to background is enhanced by selecting on the difference between the measured and expected photon arrival time, $\Delta t_\gamma$. Using an unbinned maximum likelihood fit, a value for the likelihood is determined for each of the five stable particles, e, $\mu$, $\pi$, K and p, and the observed number of signal and background photons is calculated for each track.

### 2.5.4 Performance and Summary

Resolutions and efficiencies for the DIRC are measured through the reconstruction of di-muon events such as the one depicted in figure 2.14.

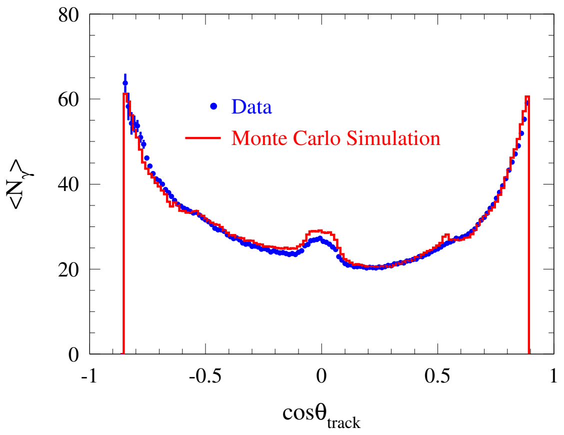


**Figure** 2.15: Number of detected DIRC photons for reconstructed tracks as a function of track polar angle $\theta$ in $e^+e^- \to \mu^+\mu^-$ events. The mean number of photons in the simulation is tuned to match the data.

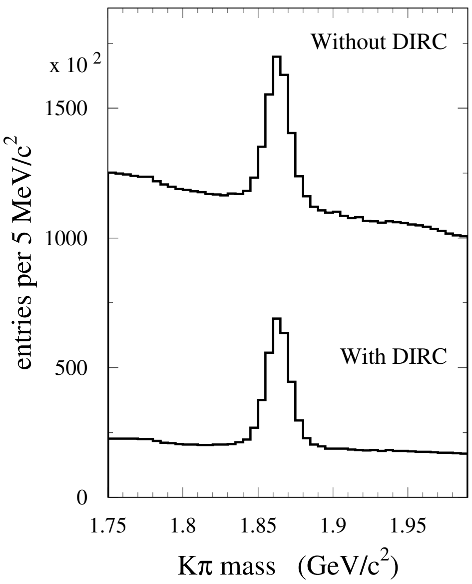


**Figure** 2.16: The beneficial effect of DIRC kaon identification on the K$\pi$ invariant mass spectrum for $D^0$ decays.

The geometric arrangement of the PMTs and radiator bars together with the r.m.s. spread of photon production and transmission dispersions suggests an expected single photon resolution of approximately 10 mrad. Analysis of di-muon events yields a measured resolution of 10.2 mrad which compares well with the expected value. Measurements of $\Delta t_\gamma$ give a resolution of 1.7 ns, again comparing favourably with the intrinsic 1.5 ns PMT spread.

A direct data/Monte Carlo comparison is shown for the mean number of photons for a track in figure 2.15. At larger values of $|\cos\theta_{track}|$ the expected number of photons increases due to the increasing track path length within the radiator and the increasing probability of photons to be trapped via total internal reflection.

Ultimately the DIRC must provide flavour tagging for hadron reconstruction. The decay $D^0 \to K^-\pi^+$ is reconstructed with and without kaon selection applied in figure 2.16. It is used to measure the mean kaon selection efficiency and pion misidentification, found to be 96.2±0.2% (stat.) and 2.1±0.1% (stat.) respectively.

The DIRC performs close to expectations derived from Monte Carlo simulations and provides good hadronic PID for *BABAR*. Currently, approximately 99.7% of PMTs and readout electronics are operating normally.

## 2.6 Electromagnetic Calorimeter

The detection of photons from $\pi^0$ and $\eta$ decays and from radiative processes, e.g. $D_s^{*+} \to D_s^+\gamma$, is the task of the Electromagnetic Calorimeter (EMC). The EMC measures electromagnetic showers over an energy range from 20 MeV up to 9 GeV. The lower bound of the energy range is determined by the need to efficiently reconstruct $B$ meson decays containing multiple $\pi^0$ and $\eta$ mesons. QED processes such as $e^+e^- \to \gamma\gamma$ set the upper bound of the required energy range. The EMC's electron identification capability contributes to the study of semi-leptonic decays of $B$ and $D$ mesons and $\tau$ leptons, and to the reconstruction of vector mesons such as the $J/\psi$.

### 2.6.1 Design and Requirements

The design choice for the EMC is a hermetic, total-absorption calorimeter. An array of caesium iodide crystals doped with 0.1% thallium (CsI(Tl)) is used in combination with silicon photodiodes to absorb the energy and measure the intensity of the scintillation light. This design principle is also successfully employed by the CLEO [58] and BELLE [59] experiments.

The crystals have an intrinsic photon detection efficiency close to 100% down to energies of a few MeV. However, due to the presence of beam-generated backgrounds and the amount of material between the EMC and IR, the effective lower energy limit becomes $\sim 20$ MeV. Since the $\pi^0$ efficiency is sensitive to the minimum detectable photon energy it is important to keep all material in front of the calorimeter to a minimum.

Energy resolution requirements are governed by the measurement of rare $B$ meson decays such as $B^0 \to \pi^0\pi^0$, which demands a resolution of 1-2%. The $\pi^0$ mass

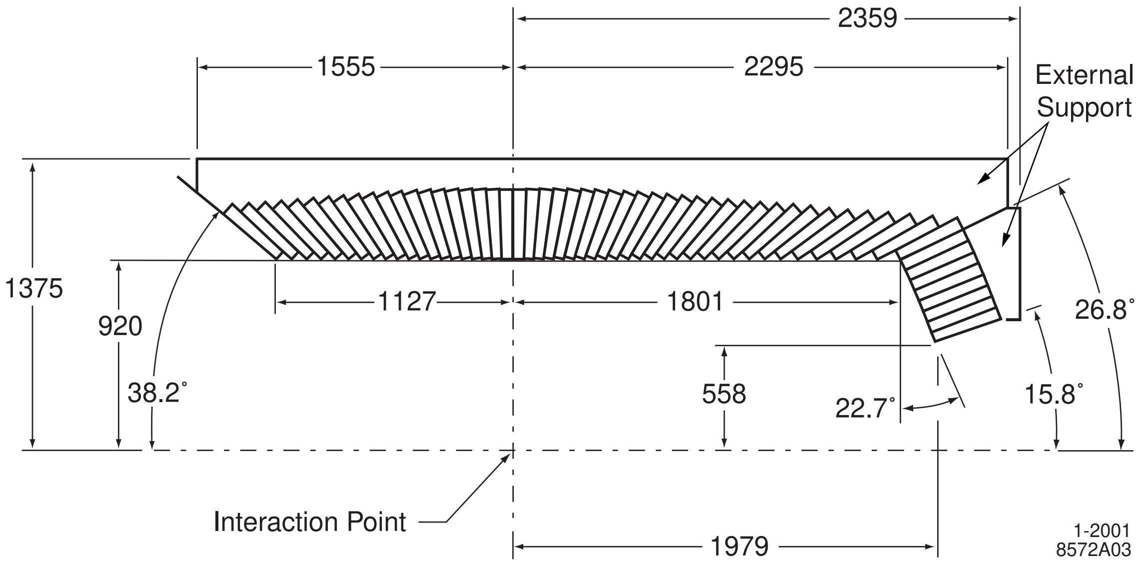


**Figure** 2.17: Cross section of the top half of the EMC showing the major dimensions in mm. The EMC is symmetric about the $z$-axis.

resolution is also dominated by the energy resolution below energies of 2 GeV. The angular resolution, which dominates at higher energies, must be of the order of a few mrad. It is determined by both the transverse crystal size and the distance from the IR. Both the energy and angular resolutions can be described empirically:

$$\frac{\sigma_E}{E} = \frac{a}{E(\mathrm{GeV})^{1/4}} \oplus b \tag{2.1}$$

$$\sigma_\theta = \sigma_\phi = \frac{c}{\sqrt{E(\mathrm{GeV})}} \oplus d \tag{2.2}$$

where $E$ and $\sigma_E$ represent the measured photon energy and its associated r.m.s. error, $\sigma_\theta$ and $\sigma_\phi$ are the polar and azimuthal angular errors, and $a$, $b$, $c$, and $d$ are constant parameters determined through fits to data.

Environmental control is essential to maintain stable, long term operation of the EMC. Leakage currents of the photodiodes rise exponentially with temperature and the CsI(Tl) crystals can become physically deformed if their temperature is not maintained at $20 \pm 1$ °C. The heat generated by the electronics is thermally conducted away via circulation of Fluorinert [60] and water separately through pipes that pass between the various readout components. In addition, a dry nitrogen atmosphere is provided to keep the slightly hygroscopic crystals free of moisture.

### 2.6.2 Structural Details

The physical design of the EMC is largely determined by the energy asymmetry of the PEP-II beams. A cylindrical barrel provides full azimuthal coverage while a forward endcap ensures 90% of the solid angle is covered in the c.m. frame (figure 2.17). The polar angle coverage extends from 15.8° to 141.0°. A double Faraday cage of two 1 mm thick aluminium sheets shields the readout electronics from external noise and serves as an environmental barrier.

A total of 5,760 crystals are housed within the barrel arranged into 48 azimuthal rings of 120 identical crystals each. A further 820 crystals arranged into 8 rings are contained in the endcap. The crystals are grouped into modules, containing 21 ($7 \times 3$ in $\theta \times \phi$) and 41 crystals each in the barrel and endcap respectively. Minimizing the material in front of the crystals reduces the probability of pre-showering and so the crystal modules are supported at the back.

In addition to the crystals acting as a scintillating medium they serve as light guides by trapping the light produced through total internal reflection at the polished crystal surface. The small amount of light that is transmitted at the surface is partially recovered by covering the crystals in a light-reflective material. A schematic of a crystal installed in the EMC is shown in figure 2.18.

The tapered trapezoidal design results in a front crystal face of $4.7 \times 4.7$ cm$^2$ and a back face of $6.1 \times 6.0$ cm$^2$. The crystals increase in length from the backward to the forward region from 29.6 cm to 32.4 cm which limits shower leakage for the higher energy particles in the forward region.

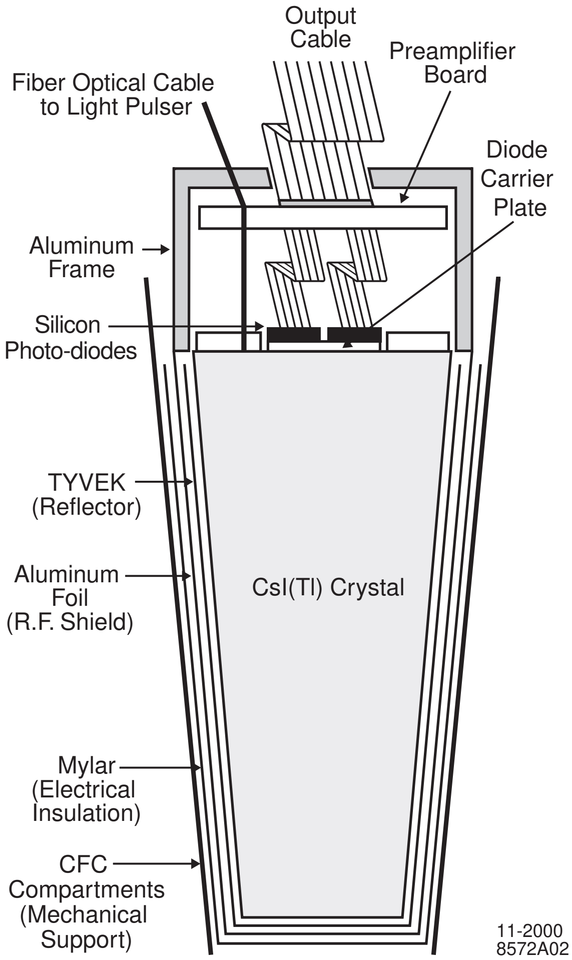


**Figure** 2.18: Schematic representation (not to scale) of a crystal installed in its CFC (carbon-fibre epoxy composite) support structure. Also indicated are the front end readout electronics attached to the crystal's rear surface.

### 2.6.3 Readout Electronics and Event Reconstruction

Photons are detected by two PIN silicon photodiodes [61] each measuring $1 \times 2$ cm$^2$. They are attached to a polysterene substrate which is glued to the rear face of a crystal using an optical epoxy chosen to maximise optical transmission. Two photodiodes are fitted for redundancy purposes, because the front end readout components are inaccessible after installation.

Each of the photodiodes has a preamplifier attached to it whose signal is transmitted to a custom auto-range encoding (CARE) circuit [62]. The CARE circuit provides four gains to yield a measurement within one of four energy ranges: 0-50 MeV, 50-400 MeV, 0.4-3.2 GeV and 3.2-13.0 GeV.

Electromagnetic showers in the EMC typically spread over multiple crystals. These clusters of energy deposits are identified as clusters with a single energy maximum or more than one maximum (called bumps) using pattern recognition algorithms. A cluster must contain a crystal with an energy greater than 10 MeV and surrounding crystals are included in the cluster if their energy is greater than 1 MeV. Contiguous neighbours of a crystal (including diagonals) with an energy greater than 3 MeV are also included. Clusters can be divided into as many bumps as the number of local maxima.

A centre of gravity method with logarithmic weights is used to determine a bump's position, a procedure which favours lower-energy crystals and uses only the core crystals that make up the cluster. Tracks and bumps are associated by extrapolating the track out to the calorimeter's inner face where the track impact point and bump centroid position are compared. If this distance is consistent with the track's momentum vector the track and bump are associated.

### 2.6.4 Performance and Summary

The energy resolution is determined at different energies by using a 6.13 MeV radioactive photon source for low energy, and Bhabha events for high energy. These are combined with measurements of photons resulting from the decay process $\chi_{c1} \rightarrow J/\psi\gamma$ with an average photon energy of 500 MeV. A fit to equation 2.1 yields the following result,

$$\frac{\sigma_E}{E} = \frac{(2.32 \pm 0.30)\%}{E(\,\mathrm{GeV})^{1/4}} \oplus (1.85 \pm 0.12)\% \tag{2.3}$$

Although slightly higher than design expectations the above result agrees well with detailed Monte Carlo simulations.

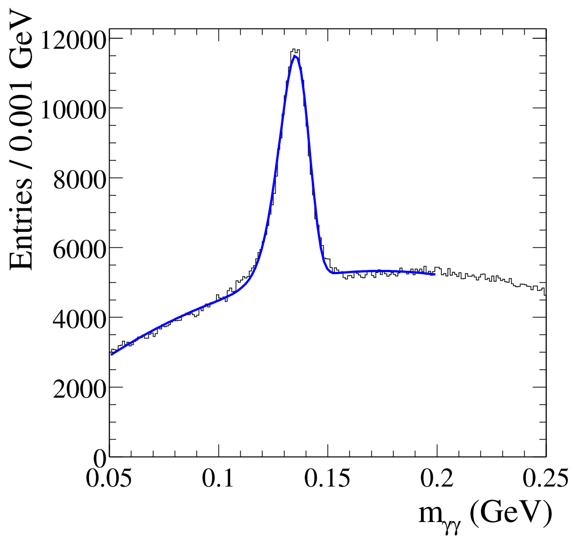


**Figure** 2.19: The invariant two-photon mass for $B\overline{B}$ events. Only photons with energies greater than 30 MeV are considered and the composite $\pi^0$ energy must be greater than 300 MeV.

The decays $\pi^0 \rightarrow \gamma\gamma$ and $\eta \rightarrow \gamma\gamma$ are used to determine the angular resolution. A fit to equation 2.2 yields a result that is slightly better than expected from Monte Carlo simulations,

$$\sigma_\theta = \sigma_\phi = (\frac{3.87 \pm 0.07}{\sqrt{E(\text{ GeV})}} \oplus 0.00 \pm 0.04) \text{ mrad} \tag{2.4}$$

The reconstructed invariant two-photon mass is 135.1 MeV/$c^2$ and over the full photon energy range remains stable to better than 1%. The $\pi^0$ mass distribution can be seen in figure 2.19 for reconstructed $B\overline{B}$ events.

By requiring the DCH $dE/dx$ and DIRC $\theta_c$ measurements to be consistent with an electron the EMC combines shower energy, shower lateral moment and track momentum measurements to achieve an electron identification efficiency of 94.8% for the momentum range $0.5 < p < 2$ GeV/$c$. The misidentification rate is at the level of 0.3%.

Overall the EMC is performing well, with only 2 permanently dead channels of the 6580 total, resulting from unfortunate accidents in the installation process.

## 2.7 Superconducting Solenoid

A magnetic field is required by the *BABAR* experiment to enable charged particle momentum measurements. The magnet system comprises a superconducting solenoid [63], a segmented steel flux return and a field compensating bucking coil. The flux return also serves as a hadron absorber for hadron/muon identification and provides structural support for the other detector sub-systems.

### 2.7.1 Design Considerations and Physical Structure

Momentum resolution of charged tracks is the overriding factor determining a required field strength of 1.5 T. This magnitude must be maintained to within a few percent inside the tracking volume. Field uniformity is important and is achieved by increasing the current density of the solenoidal coil at the ends relative to its centre. Furthermore, the field's influence upon PEP-II's beam-manipulating magnets should be kept to a minimum. The samarium-cobalt B1 dipole and Q1 quadrupole magnets can sustain the 1.5 T longitudinal field but cannot cope with a significant radial component. Their field properties can be degraded through partial demagnetisation if the radial component exceeds $\sim$0.25 T at a radius of $r$ =200 mm.

Magnetic flux leakage is a problem, particularly at the backward end near the DIRC standoff box. The field is kept to below 1 Gauss in the region of the DIRC PMTs by installing a bucking coil [64] at the face of the backward door. It also keeps field leakage into PEP-II components to a minumum. The backward plug is carefully designed to aid in the achievement of field uniformity and control of the radial components.

The flux return is a hexagonal structure (figure 2.2) weighing $\sim$870 metric tons, comprising a barrel section and two sets of end doors in the forward and backward region. The barrel flux return houses the magnet coil cryostat. Access to the inner detector is permitted through the vertically split end doors, which are mounted on skids so that they can be raised and moved.

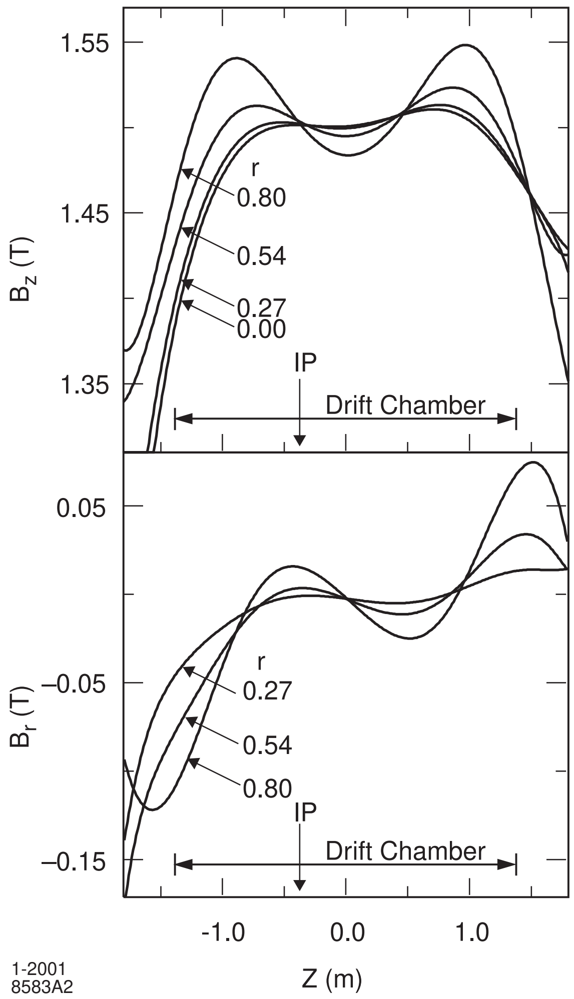


**Figure** 2.20: Magnetic field quality for the $B_z$ and $B_r$ field components.

### 2.7.2 Field Operation

The solenoid, with its niobium-titanium superconducting material, is cooled to an operating temperature of 4.5 K by circulating liquid helium through channels attached to the solenoid support cylinder.

A detailed mapping of the magnetic field components throughout the detector volume was conducted to a precision of 0.2 mT. This was achieved through the use of a specially designed device which measures the field strength at 24 azimuthal points for a total of 37 positions along the $z$-axis. The mapping device was based upon a design developed at Fermilab [65].

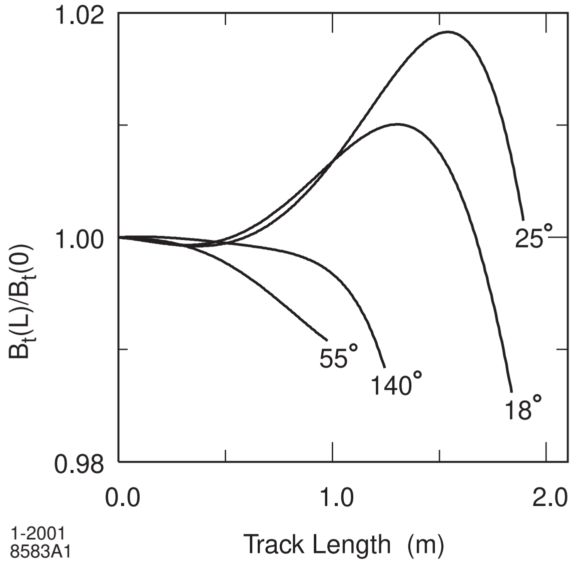


**Figure** 2.21: Variation in the field component transverse to the trajectory of a high momentum track passing through the tracking volume. The four curves represent different track polar angles labelled in the figure.

The principal field component, $B_z$, points along the $z$-axis and is kept, along with $B_r$, as uniform as possible along the tracking volume length (figure 2.20). For a given high momentum track, the field transverse to the track trajectory varies by less than 2.5% through the tracking region (figure 2.21).

### 2.7.3 Summary

The magnet system has performed to design specifications since its successful installation into *BABAR*. The bucking coil and shielding perform well in reducing the field strength in the proximity of the DIRC PMTs and in reducing field leakage into the PEP-II components. No spontaneous quenches of the field have been observed.

## 2.8 Instrumented Flux Return

The design for the flux return incorporates instrumentation for the efficient identification of muons and neutral hadrons over a wide range of momenta and angles.

The IFR (Instrumented Flux Return) is important for tagging the flavour of neutral $B$ mesons in semi-leptonic decays and for reconstructing vector mesons such as the $J/\psi$. This also applies to semi-leptonic decays of other $B$ and $D$ mesons as well as $\tau$ leptons. Studying $CP$ eigenstates of exclusive $B$ decays requires efficient $K_L^0$ detection. Additionally, the IFR improves neutrino reconstruction through missing energy measurements.

### 2.8.1 Concept and Design Requirements

As with all other detector sub-systems the IFR must fulfil a series of requirements. Primarily the IFR should have

- large solid angle coverage and good angular resolution;
- excellent efficiency;
- good background rejection for muons over all momenta; and
- reliable and well monitored readout electronics.

The steel flux return is used as both a muon filter and hadron absorber. The steel is finely segmented and into the gaps are placed resistive plate chambers [66] (RPC) with a two co-ordinate readout capability. The RPCs are installed in both the barrel (19 layers) and the forward and backward end doors (18 layers each) to maximize solid angle coverage. A further two layers are positioned between the EMC and the magnet cryostat for detection of particles exiting the calorimeter.

Streamers from ionising particles are detected by the RPCs using capacitive readout strips. The benefits of using these strips include straight-forward low cost construction, robust operation and good time resolution of 1-2 ns. They also facilitate the covering of awkwardly shaped surfaces, further minimising the dead space in the detector. A basic schematic of an RPC can be seen in figure 2.22.

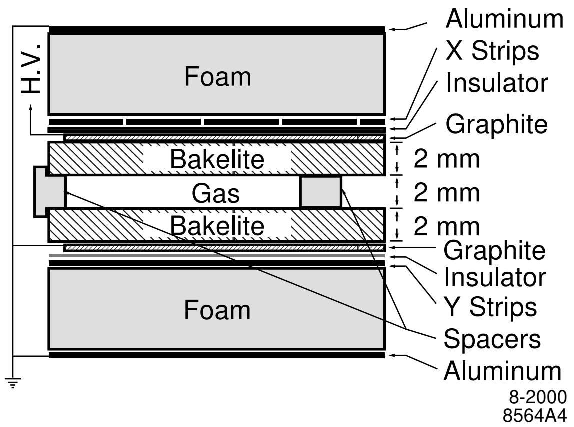


**Figure** 2.22: Cross section schematic of a planar RPC. Cylindrical RPCs differ slightly but the concept is identical.

Hits registered by individual RPCs during an event are grouped together to form clusters. A detailed description of the cluster forming algorithms can be found elsewhere [67].

### 2.8.2 Structural Details

The IFR uses a total of 806 RPC modules, covering a combined active area of approximately 2,000 m$^2$. The six barrel sectors hold 57 modules each, the four half end doors hold 108 each, and the two cylindrical layers hold 32 each. Figure 2.23 shows the principal dimensions of the barrel sextants and end-doors of the flux return, and the number of module layers each holds. During the IFR's assembly, all planar RPCs were inserted into the gaps before the flux return was installed. The cylindrical chambers were installed after the solenoid and calorimeter.

Measurement of the $z$ co-ordinate by each barrel module is performed by 32 strips arranged perpendicularly to the beam axis. A total of 96 strips parallel to the beam axis extend over 3 modules to determine $\phi$. Modules in the four cylindrical sections, covering a quarter of the azimuth each, are arranged into pairs of single gap RPCs. The inner layer has two sets of orthogonal strips running parallel to the module's

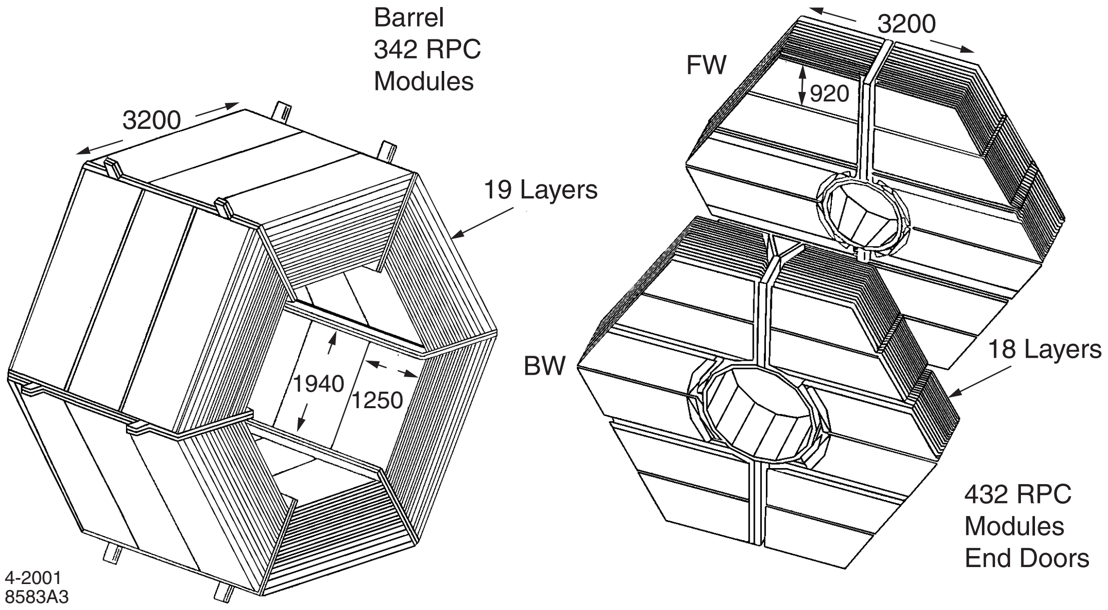


**Figure** 2.23: Diagram of the barrel and forward (FW) and backward (BW) end doors. The number of RPC layers in each is shown along with their principal dimensions (mm).

diagonal, making them helical with respect to the $z$-axis. The outer layer has two sets of orthognal strips running parallel to $z$ and $\phi$.

### 2.8.3 Front End Electronics

The IFR FEE (front end electronics) has approximately 53,000 readout channels instrumented through $\sim$ 3,300 FECs [68, 69] (front-end cards). The entire FEE system is described in more detail elsewhere [70]. Most FECs are located within the steel gaps while the remainder are mounted externally on the flux return.

During normal operation the RPCs use a non-flammable gas mixture made up of argon, freon and isobutane, each typically comprising 56.7%, 38.8% and 4.5% of the mixture, respectively.

When the trigger issues a Level 1 Accept the data are read out by dedicated ROMs (read out module). However, the FECs are not equipped with a buffer since the

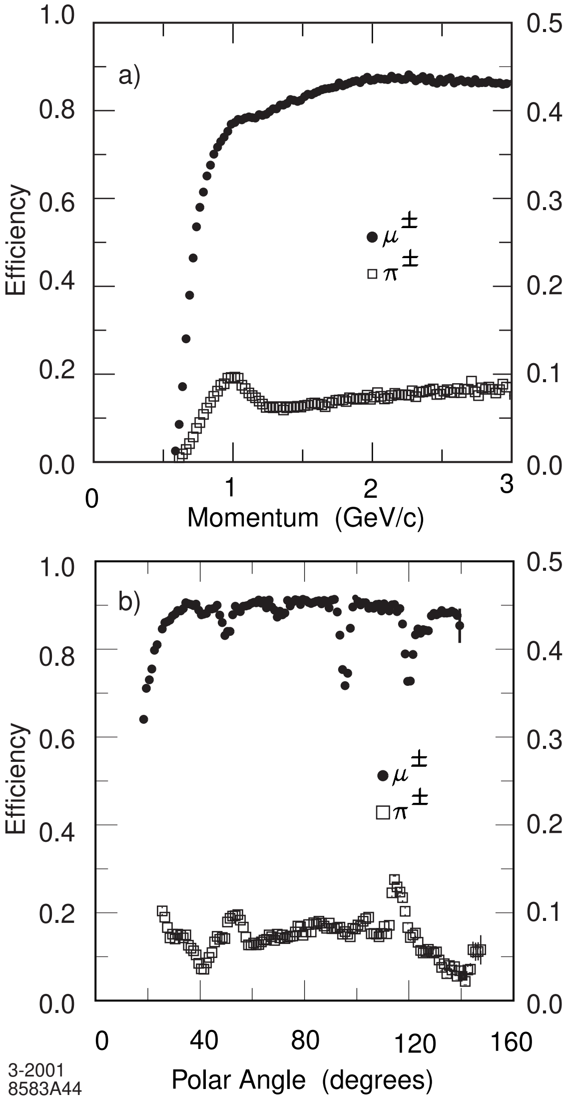


**Figure** 2.24: Muon identification efficiency (left hand scale) and pion mis-identification rate (right hand scale) as a function of both momentum (top) and polar angle (bottom). In the bottom plot, the momentum spectrum runs from 1.5-3.0 GeV/$c$.

occupancy is extremely low everywhere.

To maintain safe, stable operating conditions, a monitoring and control system is installed to control the large number of IFR components situated in and around the detector.

### 2.8.4 Particle Identification

Muon identification is a primary objective of the IFR and it incorporates information from other sub-systems to perform this task. The SVT and DCH are used to project tracks from the inner detector to the flux return and thus match them with clusters formed in the IFR. Furthermore, the muon candidates are required to satify the demands of a minimum ionising particle in the EMC.

Samples of muons are taken from reconstructed $\mu\mu ee$ and $\mu\mu\gamma$ final states and compared with samples of pions from $K_s^0 \to \pi^+\pi^-$ and three prong $\tau$ decays to determine efficiency and mis-identification rates. Over a momentum range of $1.5 < p < 3.0$ GeV/$c$ an efficiency for muon ID of $\sim 90\%$ is achieved with a pion fake rate of 6-8% (figure 2.24).

Neutral hadrons such as the $K_L^0$ are identified by requiring clusters not to be consistent with tracks in the SVT and DCH. Trajectories are inferred using the primary event vertex and the calculated centroid of the neutral cluster in the IFR. However, the energy of the hadronic shower cannot be determined.

Neutral showers in the EMC are combined with the IFR cluster information, since many of the neutral hadrons will interact with the detector before reaching the steel flux return. Missing momentum is calculated by combining the total beam momentum and the measured particles in the final state, and used to determine the direction of the neutral hadron.

The angular resolution for $K_L^0$ mesons is estimated using a sample of $e^+e^- \to \phi\gamma$ events, where the $\phi$ decays to $K_L^0 K_S^0$. It is found to be of the order of 60 mrad with an improvement by a factor of two if the neutral hadron interacts in the EMC.

The angular difference distribution, $\Delta\phi$, between the vectors for the missing momentum and the nearest neutral cluster demonstrates how missing momentum can be associated with a neutral hadron (which is assumed to be a $K_L^0$). Figure 2.25 shows this distribution for events with a reconstructed $J/\psi$.

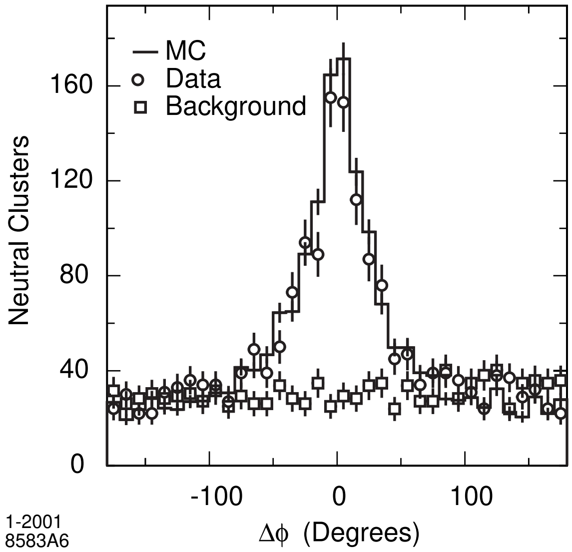


**Figure** 2.25: The angular difference between the missing momentum and nearest neutral cluster vectors for events with a reconstructed $J/\psi$. The Monte Carlo sample is scaled to the luminosity of the data while the background is synthesised using neutral hadrons and missing momenta from different events.

### 2.8.5 Performance and Summary

The IFR provides efficient muon identification and facilitates $K_L^0$ detection though interactions in the steel and calorimeter. During the initial periods of running, several RPCs have suffered significant reductions in efficiency which has subsequently been linked to temperature fluctuations around the chambers. Water cooling has been installed to prevent further degradation. Although adequate, the IFR has failed to deliver the desired physics performance to date.

In the forward endcap, five brass layers have been installed between the steel to increase the hadronic absorption. This has been done in conjunction with a complete replacement of the RPCs in this region in an effort to improve the IFR's efficiency. Moreover, an upgrade to eventually replace all the RPCs with plastic Limited Streamer Tubes (LST) in the barrel section is currently underway. LST technology is proven to provide good efficiency over many years of stable operation; prominent examples include ZEUS [71], ALEPH [72], CLEO [73] and SLD [74]. The upgrade is necessary for *BABAR* to compete in analyses where muon and hadron

ID are important such as semileptonic and purely leptonic decays and processes involving $J/\psi$ mesons.

## 2.9 Event Trigger

*BABAR* has a two-tier trigger system designed to cope with PEP-II background rates up to ten times higher than initially predicted [44]. The Level 1 (L1) trigger is implemented in hardware and the Level 3 (L3) in software. Redundancy is built into the system for measurement and monitoring of trigger efficiencies.

With an output rate of $\sim$1 kHz, the L1 produces triggers inside a fixed latency window of 11-12 $\mu$s after the $e^+e^-$ interaction which are passed on to the Fast Control and Timing System (FCTS). The L3 has an acceptance rate of $\sim$90 Hz for physics events after it receives the output from L1 and performs a second stage rate reduction.

### 2.9.1 Design Requirements

The purpose of the trigger system is to select physics events of interest (table 2.2) while rejecting background events and maintaining the total event rate at less than 120 Hz. Moreover, the trigger must be able to function reliably with a well understood efficiency even with extreme background conditions, and contribute less than 1% to detector dead time.

The trigger is designed with $B$ physics in mind, hence for $B\overline{B}$ events the trigger efficiency should exceed 99%. For continuum and $\tau^+\tau^-$ events the efficiencies should be better than 95% and 90% respectively.

**Table** 2.2: The principal physics processes with their associated cross sections, production rates and L1 acceptance rates. The numbers are for a c.m. energy of 10.58 GeV and a luminosity of $3 \times 10^{33}$ cm$^{-2}$s$^{-1}$. Here $q\overline{q}$ includes $u\overline{u}$, $d\overline{d}$ and $s\overline{s}$.

| Event type | Cross section (nb) | Production Rate (Hz) | Level 1 Trigger Rate (Hz) |
|---|---|---|---|
| $B\overline{B}$ | 1.1 | 3.2 | 3.2 |
| $c\overline{c}$ | 1.3 | 3.9 | 3.9 |
| other $q\overline{q}$ | 2.1 | 6.3 | 6.2 |
| $e^+e^-$ | $\sim$53 | 159 | 156 |
| $\mu^+\mu^-$ | 1.2 | 3.5 | 3.1 |
| $\tau^+\tau^-$ | 0.9 | 2.8 | 2.4 |

### 2.9.2 Level 1 Trigger

Three detector sub-systems contribute to the L1 trigger decision, namely the DCH, EMC and IFR. The DCH triggers on the measured transverse momentum, $p_t$, of detected tracks when it exceeds a configurable minimum value. The EMC is split into 280 towers where each tower corresponds to a group of crystals spanning sections of $\theta$ and $\phi$ in the barrel ($8 \times 3$ in $\theta \times \phi$)) and wedges in $\phi$ in the endcap. In a given tower all crystal energies are summed for those that exceed a 20 MeV threshold. The IFR is used to trigger on $\mu^+\mu^-$ events and cosmic rays primarily for diagnostic purposes.

Operating in a continuous sampling mode, the L1 global trigger (GLT) receives trigger primitives from the DCT (Drift Chamber Trigger) and EMT (Electromagnetic Trigger) every 134 ns. They are known as $\phi$-maps and contain summary data on the position and energy of particles. Each $\phi$-map is made up of an $n$-bit word representing trigger objects within a particular azimuthal region. A trigger object indicates the presence of a particle, be it a DCH track or energy deposit in the EMC. These primitives are formed into specific triggers including track-cluster matching and sent to the FCTS, which is capable of masking or pre-scaling any triggers. Event readout is then initiated via a L1 Accept signal if any valid triggers remain. The entire process is performed within the 12.8 $\mu$s FEE buffer limit.

Of the 1 kHz L1 rate approximately 130 Hz is due to Bhabha and annihilation

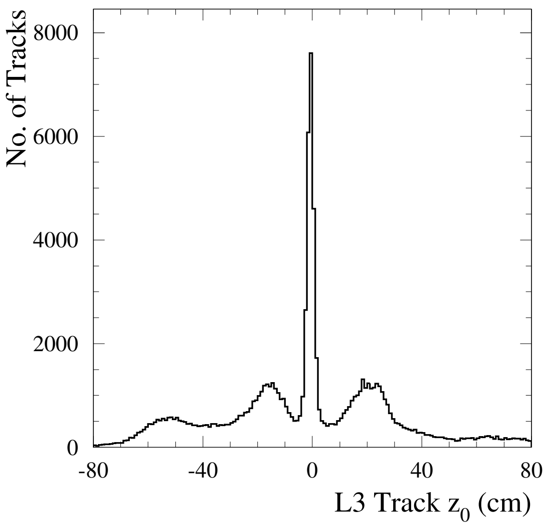


**Figure** 2.26: The $z_0$ (see text) distribution for single tracks reconstructed by the L3 trigger. Physics events are peaked at $z_0 = 0$.

physics events. Cosmic rays and random beam crossings contribute 100 Hz and 20 Hz respectively while the remaining majority results from particles interacting with the beam pipe and detector components. Figure 2.26 shows the distribution of $z_0$ (the point at which the track intersects the $z$-axis) for single tracks reconstructed by L3 for all L1 triggers. It clearly shows the physics events peaked at zero and additional peaks either side at $\pm 20$ cm corresponding to flanges of the beam pipe.

### 2.9.3 Level 3 Trigger

The software-based L3 trigger has access to the entire event information, including the output of L1, and is designed to reconstruct, classify and filter events using the resources of the online computer farm. Algorithms for the DCH and EMC exist to determine quantities of interest for a given event. A series of L3 filters based on tracks and clusters perform event classification and background reduction.

A DCH-based L3 algorithm is employed to reject beam-generated background. Fast pattern recognition is used to determine the five helix track parameters for tracks with $p_t > 250$ MeV/$c$. Furthermore, the EMC provides an all neutral trigger for L3

**Table** 2.3: L3 output for physics and other events at a luminosity of $2.6\times10^{33}$ cm$^{-2}$s$^{-1}$.

| Event type | Rate (Hz) |
|---|---|
| Hadrons, $\tau\tau$, and $\mu\mu$ | 16 |
| Other QED, 2-photon events | 13 |
| Unidentified Bhabha backgrounds | 18 |
| beam-induced backgrounds | 26 |
| Total physics accept | **73** |
| Calibration Bhabhas ($e^+e^-$) | 30 |
| $\gamma\gamma$, Radiative Bhabhas ($e^+e^-\gamma$) | 10 |
| Random triggers and cosmic rays | 2 |
| L1,L3 pass through diagnostics | 7 |
| Total calibration/diagnostics | **49** |

consisting of a series of algorithms to select events of interest. It provides essential complementary information to the DCH for the identification of Bhabha events.

In addition to online luminosity monitoring, L3 flags Bhabha, radiative Bhabha, cosmic ray and $\gamma\gamma$ final state events for offline luminosity measurements and calibration. To this end the readout rate of flagged Bhabha events is adjusted such that the distribution is approximately flat across the full range of $\theta$.

When triggering on events at 10.58 GeV at a luminosity of $2.6\times10^{33}$ cm$^{-2}$s$^{-1}$, the L3 output rate contains $\sim$13% interesting physics events (table 2.3). Diagnostic and calibration events make up almost 40%.

### 2.9.4 Summary

The *BABAR* event trigger system fulfils all design goals at an operating luminosity of $3\times10^{33}$ cm$^{-2}$s$^{-1}$. Triggering on $B\overline{B}$ events has a desired efficiency of $\sim$99% and L3 processors do not become saturated until the L1 output rate reaches 2.7 kHz, significantly higher than the 2 kHz design rate. It is anticipated that the trigger will continue to function well for the full life of the experiment and at luminosities above $10^{34}$ cm$^{-2}$s$^{-1}$.

## 2.10 Data Acquisition System

The entire data acquisition (DAQ) chain involves the FEE, L3 trigger, event data logging, detector monitoring and control, data quality monitoring and all online detector calibrations. Collectively it is know as the *BABAR* online computing system, and is composed of a series of online sub-systems with unique responsibilities:

- Online Dataflow (ODF) - communicates with FEE and builds event data;
- Online Event Processing (OEP) - processes complete events and L3 trigger software and performs data quality monitoring;
- Logging Manager (LM) - writes events to disk after receiving them from OEP;
- Online Detector Control (ODC) - controls and monitors all detector sub-systems; and
- Online Run Control (ORC) - provides a graphical user interface (GUI) to facilitate control of all other online systems listed above.

A farm of 32 online CPUs host both the OEP and L3 trigger software for event reconstruction, while additional nodes run the various data quality monitoring processes. A schematic of the online computing system hardware is show in figure 2.27.

### 2.10.1 System Requirements

The online computing system has a responsibility to manage data acquisition for events with an average size of 32 kB, and must not contribute more than 3% to the time-averaged dead time of the detector. Although the L1 trigger output rate is $\sim$1 kHz, the system should support a rate of up to 2 kHz reliably and ensure the L3 output rate never exceeds a maximum value of 120 Hz.

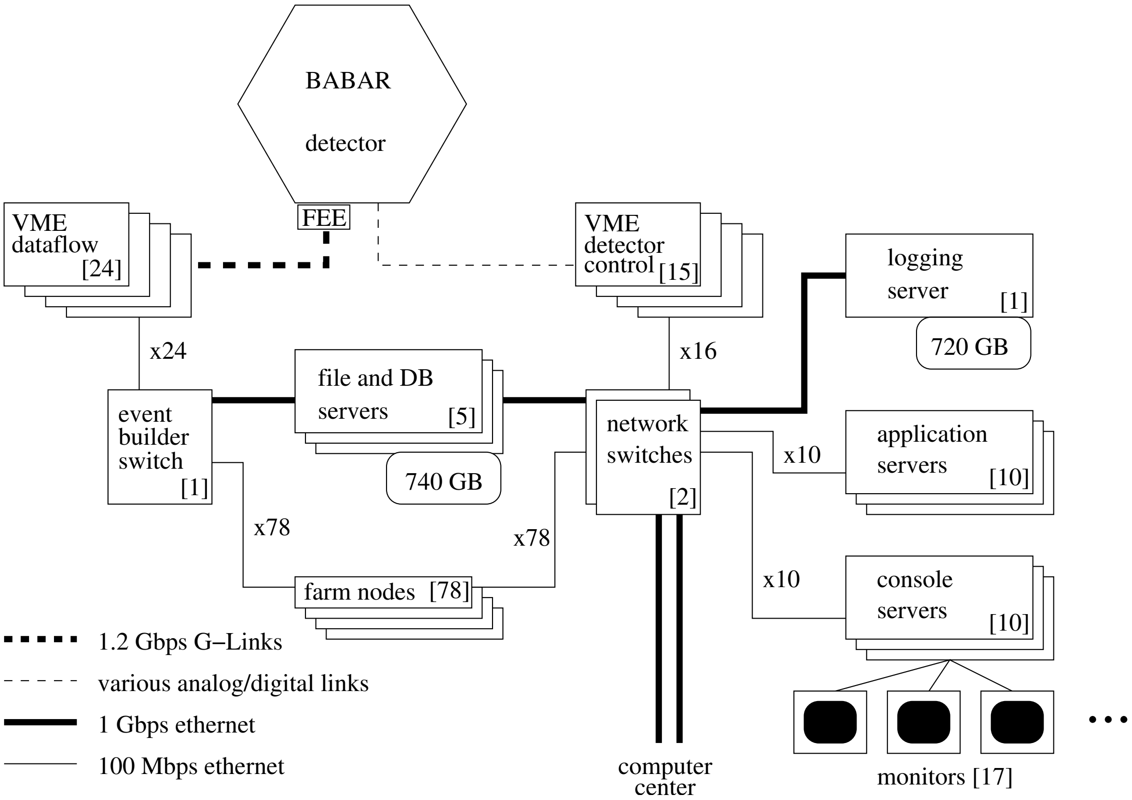


**Figure** 2.27: A schematic representation of the hardware used for the online computing system.

Monitoring of detector sub-systems and environmental conditions in and around the IR is also a key responsibility of the online system. Operating parameters of the PEP-II machine are closely monitored to ensure that data are recorded only for those conditions that are considered stable for detector operation. All of this should be achievable through a simple GUI from which all aspects of the detector can be monitored and controlled.

### 2.10.2 Online Control

Control of the detector is performed through a custom GUI that provides a complete facility for manipulating the state of the detector, performing calibrations and the acquisition of data. For monitoring and control of detector sub-systems directly, the Experimental Physics and Industrial Control System [75] (EPICS) is chosen to provide direct connections to the sub-system power supplies and hardware.

The EPICS system also enables a sharing of information between the PEP-II machine and *BABAR* detector. To achieve efficient data acquisition it is desirable that data pertaining to the state of the PEP-II machine should be available in real time within ODC. Vice versa, information such as current background conditions in the detector is available to the PEP-II operators enabling them to adjust the machine settings and return to stable operation as quickly as possible.

### 2.10.3 Data Storage

Events that satisfy all requirements of the L3 trigger algorithms in OEP are written to RAID storage arrays by the LM, running on a dedicated server. Those events common to a single data run are stored in a single file which is typically 15-20 GB in size. Once completed, each datafile is copied to the SLAC High Performance Storage System [76] (HPSS) for archiving. Data is then retrieved, within 8 hours of its acquisition, for full offline event reconstruction.

### 2.10.4 Summary

The online computing system satisfies all requirements set out by the *BABAR* experiment. It is capable of taking data reliably up to a L1 output rate of 2.5 kHz while keeping the L3 output rate below 120 Hz. Furthermore, the system has the ability to log data at a rate far greater than the 120 Hz constraint. L3 output is kept to this level to reduce the load on downstream event reconstruction systems and storage facilities, but it is still high enough to provide good trigger efficiency for low multiplicity final states. At nominal operation the DAQ system logs data with an efficiency of over 98%.

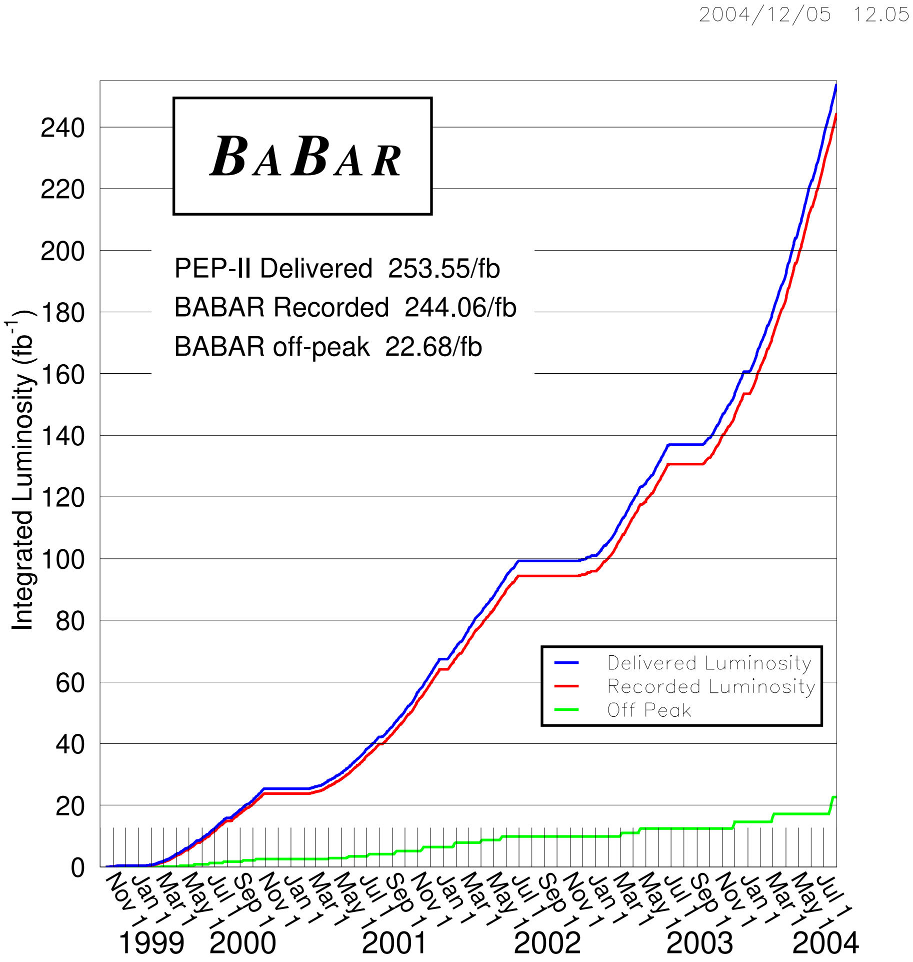


**Figure** 2.28: Time-integrated PEP-II delivered and *BABAR* recorded luminosity. The final values are scaled from the PEP-II luminosity monitor by the L3/PEP-II and L3/offline luminosity correction factors.

## 2.11 *BABAR* Summary and Outlook

The *BABAR* detector continues to fulfil its physics goals and operates at close to or beyond design expectations. Reliable and efficient performance in conjunction with the PEP-II machine has culminated in a 244 fb$^{-1}$ high quality dataset (figure 2.28) that is extensively used for physics analyses. The data have been collected between 1999 and 2004 during four major, continuous running periods denoted Run1-Run4. Significant down-time between the major run periods is used for substantial detector maintenance and upgrade projects.

Along with efficient detector operation, the size of the data sample is due to excellent beam conditions. PEP-II has achieved instantaneous luminosities beyond three times the design specification and the introduction of LER-only trickle-injection in November 2003, followed by both the HER and LER in March 2004, allowed the dataset to double in size in just 18 months.

The future plans for *BABAR* involve two successive doublings of the dataset over the next 3 years, leading to a total integrated volume of $\sim 1$ ab$^{-1}$ by 2008. To aid in achieving this target PEP-II vacuum and RF upgrades are planned. The completion of the LST upgrades is expected by the summer of 2006.

# Chapter 3

# Analysis Development

## 3.1 Overview

In searching for rare decay modes of the $D_s$ meson, decay chains are fully reconstructed using a kinematic, least squares fit. A simulation of the *BABAR* experiment provides large Monte Carlo (MC) datasets with which to develop a blind analysis and identify discriminating variables to enhance the signal to background ratio. A blind analysis is one in which the data are not used at any stage of the development. The data are only analysed after the method is shown to be unbiased and optimal after being tuned on MC data. No reconciliation between real and MC data is attempted, instead any differences are accounted for through the inclusion of systematic errors. Where multiple candidates per event remain after all selections are applied, a consistent method is used to select the best candidate. A maximum likelihood technique is employed to analyse the final, signal-enhanced data.

In total, four decay modes and their charge conjugates are reconstructed; $D_s^+ \to K^+\pi^0$, $D_s^+ \to \pi^+\pi^0$, $D_s^+ \to \pi^+K^0$ and $D_s^+ \to K^+\overline{K}^0$. The first three are the signal modes while the fourth is a reference mode needed for normalisation of the measurements. For the decay modes involving a $K^0$ or $\overline{K}^0$ in the final state, the actual reconstructed particle is a $K_S^0$. This choice is made due to the complications involved in $K_L^0$ reconstruction. Moreover, the $K_S^0$ is reconstructed from a $\pi^+\pi^-$ final state. When calculating branching ratios for the signal modes with respect to $D_s^+ \rightarrow K^+\overline{K}^0$ these factors must be taken into account. The procedure is known as decay tree reconstruction, where a single particle represents the root of the decay tree and all subsequent particles result either directly or indirectly from the decay of this particle. For all decay trees reconstructed in this analysis the root particle is a $D_s^*$ meson.

The development of the analysis is split into several concurrent stages:

1. Event preselection,
2. Refined decay tree reconstruction,
3. Initial signal to background enhancement,
4. Development of the maximum likelihood analysis, and
5. Optimisation of signal to background enhancement for the likelihood analysis.

Each stage is described in detail within this chapter. Once development and optimisation has been performed, the likelihood analysis is tested for any bias that may have been introduced during the development. To accomplish this the technique of toy Monte Carlo analysis is employed. A toy dataset is one that is generated using predefined probability density functions that describe the distributions of the variables to be generated. The technique allows for the identification of inconsistencies within the likelihood analysis through repeated generating and fitting of the toy Monte Carlo samples.

**Table** 3.1: The datasets used for this analysis together with their integrated luminosity contribution.

| Data Set | Integrated Luminosity / $\mathrm{fb}^{-1}$ | | |
|---|---|---|---|
| | Off Resonance | On Resonance | Combined |
| Run1 | 2.33 | 17.81 | 20.14 |
| Run2 | 6.83 | 59.40 | 66.23 |
| Run3 | 2.39 | 30.63 | 33.02 |
| Run4 | 9.93 | 99.41 | 109.34 |
| Total | 21.48 | 207.25 | 228.73 |

## 3.2 Datasets

### 3.2.1 Data

This analysis uses the complete *BABAR* Run1-Run4 dataset. After processing, the total usable integrated luminosity is $\sim 229\ \mathrm{fb}^{-1}$ of which $\sim\ 21.5\ \mathrm{fb}^{-1}$ was taken off resonance at a centre of mass energy $\sim\ 40$ MeV below the mass of the $\Upsilon(4S)$. Each run contributes the corresponding off and on resonance amounts in table 3.1.

### 3.2.2 Monte Carlo Data

In an attempt to avoid bias, development of the analysis is performed using a sample of simulated events of comparable size to the full data sample. The *BABAR* experiment is simulated using software centred around the Geant4 simulation toolkit [77]. In addition to the major backgrounds, sizeable samples of pure signal for each mode of interest are produced in order to parameterise the signal with some accuracy. Table 3.2 lists the signal and background Monte Carlo (MC) samples used in this analysis.

## 3.3 Event Preselection

The full data and MC samples undergo an initial selection procedure, known as a 'skim', to remove unwanted background events while retaining as much signal as is practical. This is achieved by placing cuts on certain variables at various stages of the decay chain reconstruction. The skim constructs composite particles in the signal decay tree through 4-momentum addition of the daughter particles for speed since the datasets are large. At a later stage events which pass the skim criteria have their decay tree recomputed using the TreeFitter algorithm. TreeFitter is a global decay chain fit using a Kalman filter [78] which, for the decay modes involving $K_S^0$ reconstruction, yields more accurate results than 4-momentum addition but requires more computational resources. It is also used for the modes containing $\pi^0$ candidates for consistency throughout the reconstruction process.

### 3.3.1 Charged and Neutral Objects

The composite candidates in the decay tree are constructed by creating combinations of tracks and/or neutrals in the event.

Where a list of charged tracks is required in the decay tree the GoodTracksLoose list is chosen, except in the special case of $K_S^0$ reconstruction which is described below. The list contains all non-zero charge candidates (initially with a pion mass hypothesis) in the event that satisfy

- $N_{DCH} \geqslant 12$;

**Table** 3.2: MC samples used for analysis development.

| Background Modes | No. of events |
|---|---|
| $q\overline{q}$ $(q = u, d, s)$ | 677 M |
| $B^+B^-$ | 584 M |
| $B^0\overline{B^0}$ | 527 M |
| $c\overline{c}$ | 426 M |
| $\tau^+\tau^-$ | 347 M |
| Signal Modes (charge conjugation implied) | |
| $c\overline{c} \to D_s^{*+} + X$, $D_s^{*+} \to D_s^+\gamma$, $D_s^+ \to K^+\pi^0$ | 468 k |
| $c\overline{c} \to D_s^{*+} + X$, $D_s^{*+} \to D_s^+\gamma$, $D_s^+ \to \pi^+\pi^0$ | 470 k |
| $c\overline{c} \to D_s^{*+} + X$, $D_s^{*+} \to D_s^+\gamma$, $D_s^+ \to K^+K_S^0$ | 464 k |
| $c\overline{c} \to D_s^{*+} + X$, $D_s^{*+} \to D_s^+\gamma$, $D_s^+ \to \pi^+K_S^0$ | 462 k |

- $p_T > 0.1$ GeV/$c$;
- $p < 10.0$ GeV/$c$;
- $\mathrm{DOCA}_{xy} < 1.5$ cm; and
- $-10$ cm $\leqslant \mathrm{DOCA}_z \leqslant 10$ cm,

where $N_{DCH}$ is the number of hits recorded by the DCH, $p_T$ is the track's transverse momentum in the laboratory frame, $p$ is the track's momentum in the laboratory frame, $\mathrm{DOCA}_{xy}$ is the distance of closest approach between the track and the primary event vertex in the $x$-$y$ plane and $\mathrm{DOCA}_z$ is the distance of closest approach between the track and the primary event vertex along the $z$-axis.

Where photons are required the GoodPhotonLoose list is chosen. The list comprises single bump neutral objects detected in the EMC that are not consistent with a track in the event. In addition, the photon mass hypothesis is assigned to these candidates and they are required to have a raw EMC energy greater than 30 MeV and a lateral moment [79] less than 0.8.

### 3.3.2 $\pi^0$ Candidates

Various lists of neutral pions are produced for each event through 4-vector addition of photons. Candidates on the GoodPhotonLoose list have their 4-momenta summed and the resultant $\pi^0$ candidate is kept if the mass lies in the range $0.10 < M_{\pi^0} < 0.16$ GeV/$c^2$ and the energy in the laboratory frame satisfies $0.2 < E_{lab} < 100.0$ GeV. Distributions of these quanitites can be seen in figure 3.1. The list is refined by requiring the $\pi^0$ production point to be the event's primary vertex, and by applying a mass constraint. By constraining the pion's mass the mass resolution of its parent particle can be significantly improved, providing the $\pi^0$s are real.

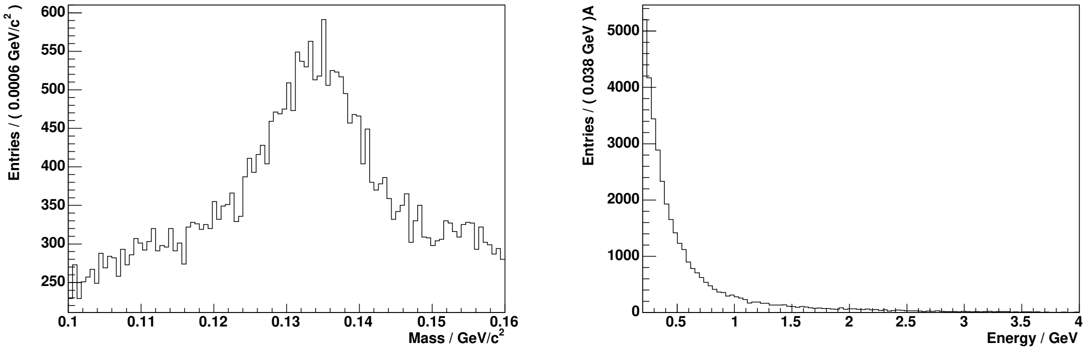


**Figure** 3.1: $\pi^0$ mass distribution before the mass constraint is applied during the $D_s$ decay chain fit (left) together with the energy in the laboratory frame (right).

### 3.3.3 $K_S^0$ Candidates

Neutral kaon reconstruction is performed using the TreeFitter algorithm to determine the decay position. All detected particles with non-zero charge in the event are used to construct the KsLoose list via the decay $K_S^0 \rightarrow \pi^+\pi^-$. The tracks have the pion mass hypothesis assigned. Since vertexing is computationally expensive a loose mass cut is applied before the process begins using 4-vector addition, $0.3 < M_{K_S^0} < 0.8$ GeV/$c^2$, together with a point of closest approach (POCA) mass cut of $0.45 <$ POCA $M_{K_S^0} < 0.55$ GeV/$c^2$. After vertexing a tighter mass cut (figure 3.2) is applied: $0.47267 < M_{K_S^0} < 0.52267$ GeV/$c^2$.

### 3.3.4 Skim Selection Criteria

The full decay chain for each of the signal modes is constructed from the particle lists mentioned above. $D_s$ mesons are composed of charged tracks with the relevant mass hypothesis and either a $\pi^0$ or $K_S^0$ candidate. The $D_s$ mesons are combined with a photon to reconstruct the $D_s^*$ mesons. The skim performs this for each of the four final states; $D_s^\pm \rightarrow K^\pm\pi^0$, $D_s^\pm \rightarrow \pi^\pm\pi^0$, $D_s^\pm \rightarrow K^\pm K_S^0$ and $D_s^\pm \rightarrow \pi^\pm K_S^0$. An event passes the skim if any candidates remain after applying the following cuts:

- $1.65 < M_{D_s} < 2.30$ GeV/$c^2$,

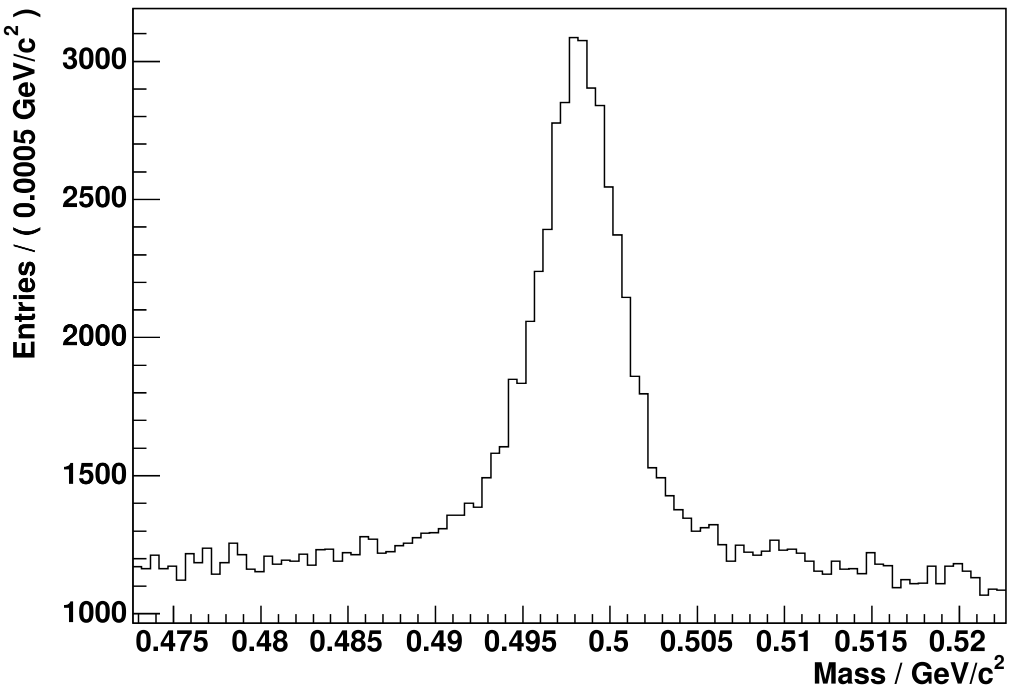


**Figure** 3.2: Mass distribution for $K_S^0$ candidates used in the reconstruction of $D_s$ mesons.

- $1.7 < M_{D_s^*} < 2.5\ \mathrm{GeV}/c^2$,
- $\Delta M < 0.25\ \mathrm{GeV}/c^2$ and
- $p_{cms} > 2.6\ \mathrm{GeV}/c$ for the $D_s^*$ candidate.

where $\Delta M = M_{D_s^*} - M_{D_s}$ and $p_{cms}$ is the momentum in the centre of mass frame. At this stage the cuts are required to reduce the event selection rate to practical levels for the more complicated event reconstruction to follow the skim because the *BABAR* dataset is large. Therefore, the cut values are quite loose.

The skim selection efficiencies for the different signal and background modes, as determined from MC samples, are listed in table 3.3. By far the most powerful of these variables is the centre of mass momentum cut on the $D_s^*$ candidate, $p_{cms}$, which is discussed further in the next section. It is essentially $p_{cms}$ that causes the signal MC event selection efficiencies to be reduced to the 50% level.

**Table** 3.3: Skim event selection efficiencies for MC samples.

| MC Sample | Skim Selection Efficiency / % |
|---|---|
| $D_s^\pm \to K^\pm \pi^0$ | 47.0 |
| $D_s^\pm \to \pi^\pm \pi^0$ | 48.7 |
| $D_s^\pm \to K^\pm K_S^0$ | 44.2 |
| $D_s^\pm \to \pi^\pm K_S^0$ | 46.6 |
| $q\overline{q}$ $(q = u, d, s)$ | 19.6 |
| $B^+B^-$ | 3.2 |
| $B^0\overline{B^0}$ | 2.6 |
| $c\overline{c}$ | 12.9 |
| $\tau^+\tau^-$ | 2.1 |

### 3.3.5 Refined Decay Tree Reconstruction

After the skim has selected potential events of interest, these events are fully reconstructed again under a different regime. The reconstruction is the same except the TreeFitter decay chain fitting algorithm, together with a set of constraints, replaces the 4-vector addition used by the skim.

In reconstructing the $D_s$ candidates a constraint must be placed on the production vertex, because in the case of decay modes with a $\pi^0$ there is only one daughter track and hence there is no way of reconstructing the $D_s$ decay vertex. Since the parent particle is a resonance the $D_s$ is required to originate within the run-averaged interaction point, which spans approximately 10 $\mu$m in $y$, 200 $\mu$m in $x$ and 8 mm in $z$. Following this the $D_s$ candidates survive if they possess,

- a mass in the range, $1.75 < M_{D_s} < 2.15$ GeV/$c^2$;
- a probability associated with the TreeFitter least squares fit $\chi^2$ above 0.001; and
- a $|\cos\theta_H|$ value less than 0.9, where $\theta_H$ is the helicity angle defined as the angle between the daughter charged track direction in the rest frame of the mother ($D_s$) and the mother's flight direction in the laboratory frame.

Unlike leaf-by-leaf fitters which build decay trees from the bottom up, TreeFitter performs a least squares fit on the entire decay tree simultaneously. Consequently, when producing the list of $D_s^*$ candidates the previous vertex fit for the $D_s$ candidate is invalidated and the entire tree is fitted together. All particles in the chain then have their respective 4-momenta updated using the fit result. A set of cuts are applied at this stage after reconstruction of the $D_s^*$:

- $1.75 < M_{D_s^*} < 2.40$ GeV/$c^2$,
- $\chi^2$ probability of the TreeFitter decay chain fit $> 0.001$,
- $\Delta M < 0.25$ GeV/$c^2$ and
- $p_{cms} > 3.4$ GeV/$c$ for the $D_s^*$ candidate.

At this stage the cuts are designed to reduce the event rate further for a more detailed analysis to be conducted, hence the cut values used above are somewhat arbitrary. Of the cuts that have been tightened from the skim selection stage, the most notable is the centre of mass momentum cut on the $D_s^*$ candidate, $p_{cms}$. This quantity is highly correlated with the normalised $D_s^*$ momentum defined by equation 1.25. A lower bound cut value of $p_{cms} = 3.4$ GeV/$c$ corresponds to $x_p \simeq 0.7$, which is reflected later in figure 3.3.

The event selection efficiencies for each dataset after the final reconstruction are listed in table 3.4. Efficiencies for each individual reconstruction mode are provided for completeness.

## 3.4 Initial Signal to Background Enhancement

At this stage all events have been reconstructed and a loose set of kinematic cuts have been applied to remove the vast majority of background events from the data and MC samples. Now some additional variables are chosen for the preferential selection

**Table** 3.4: Event selection efficiencies for generic MC and signal MC samples after the refined event reconstruction. Efficiencies for each reconstruction mode are listed.

| Sample | Mode Specific Reconstruction Efficiencies / % | | | |
|---|---|---|---|---|
| | $D_s^\pm \to K^\pm\pi^0$ | $D_s^\pm \to \pi^\pm\pi^0$ | $D_s^\pm \to K^\pm K_S^0$ | $D_s^\pm \to \pi^\pm K_S^0$ |
| $q\overline{q}$ $(q = u, d, s)$ | 1.07 | 0.782 | 0.698 | 0.487 |
| $B^+B^-$ | 0.0358 | 0.0261 | 0.0283 | 0.0199 |
| $B^0\overline{B^0}$ | 0.0247 | 0.0176 | 0.0238 | 0.0164 |
| $c\overline{c}$ | 0.280 | 0.165 | 0.835 | 0.461 |
| $\tau^+\tau^-$ | 0.0236 | 0.0209 | 0.0126 | 0.00384 |
| Signal MC | 16.2 | 16.4 | 12.3 | 12.7 |

of signal events over background events in order to clean the samples further for the likelihood analysis. The signal and background MC samples are used to identify such variables.

Combinatoric backgrounds are rejected by comparing reconstructed $D_s^\pm \to K^\pm\pi^0$ signal MC events with and without a truth match. The $D_s^\pm \to K^\pm\pi^0$ mode is used because historically it is the decay mode that motivated the analysis. An event is said to be truth matched if all particles in the decay chain are consistent with the particles in the original truth tree generated by the simulation. The truth matched distributions for each variable are compared with the equivalent distribution of each major background to determine how useful each discriminant is.

As mentioned above, the analysis is developed and optimised solely using reconstructed $D_s^\pm \to K^\pm\pi^0$ MC events. Where applicable the same cuts determined for this mode are applied to the other three reconstructed decay modes. There is no justification for this decision, other than the choice to have some consistency between the analyses.

### 3.4.1 $D_s^*$ Normalised Momentum

The characteristically fast $D_s^*$ mesons produced in $c\overline{c}$ fragmentation events provide the most powerful variable in this analysis for reducing the level of all backgrounds. The momentum of the $D_s^*$ candidate normalised to the available beam momentum,

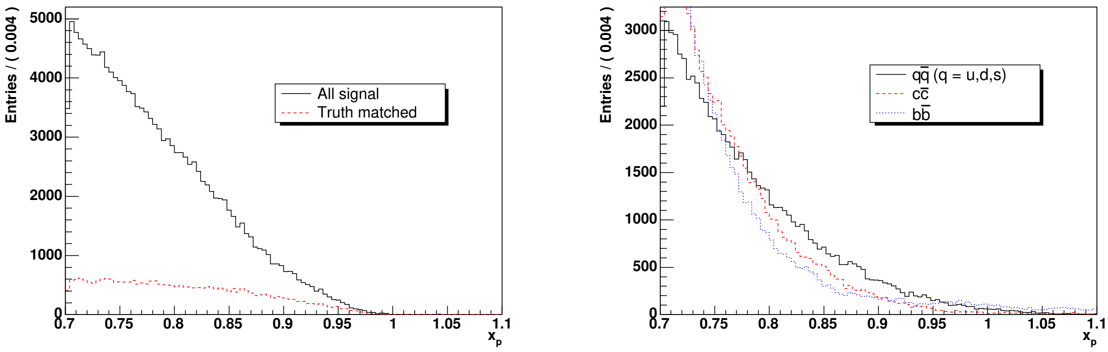


(a) Signal MC (b) Generic MC

**Figure** 3.3: Distribution of $x_p$ for $D_s^{\pm} \to K^{\pm}\pi^0$ signal MC events (a) and generic MC events (b). A high cut value dramatically reduces all background.

$x_p$, as defined by equation 1.25 is excellent for rejecting both combinatoric and light quark background. It is particularly efficient at rejecting $D_s^*$ mesons originating from $B$ decays.

Figure 3.3(a) shows the $x_p$ distribution for all reconstructed $D_s^{\pm} \to K^{\pm}\pi^0$ signal MC events and the subset that are consistent with the true decay tree. The true events have a much flatter distribution than the random combinations which increases as $x_p$ reduces. A cut at high values of $x_p$ can remove large amounts of the background as indicated by figure 3.3(b). At this stage the final cut value is unspecified because $x_p$ is chosen as one of the variables with which to optimise the likelihood analysis (see section 3.6).

### 3.4.2 $D_s$ Helicity Angle

The $D_s$ helicity is a useful variable for rejecting light and charm quark backgrounds, whose $\cos\theta_H$ distributions are strongly peaked at $\pm 1$ (figure 3.4(b)). The truth matched signal events form a flat distribution across the full range of $\cos\theta_H$ (figure 3.4(a)). Thus, to improve the signal to background ratio for these modes a cut is placed at $|\cos\theta_H| < 0.8$. Although $b\bar{b}$ background is not efficiently rejected by this cut, almost none remains after the $x_p$ cut has been applied.

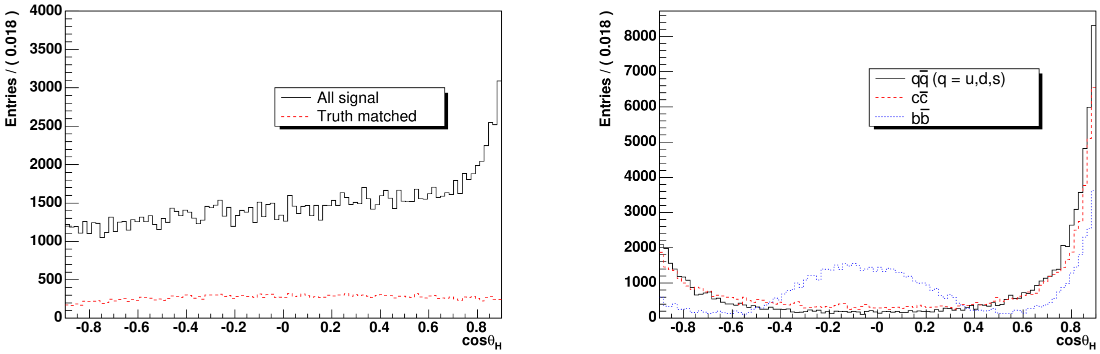


(a) Signal MC

(b) Generic MC

**Figure** 3.4: $D_s$ helicity angle distribution, $\cos\theta_H$, for $D_s^{\pm} \to K^{\pm}\pi^0$ signal MC events (a) and generic MC events (b). Cutting at $|\cos\theta_H| < 0.8$ reduces the light and charm quark backgrounds considerably, but has little effect on $b\bar{b}$ background.

### 3.4.3 Radiative $\gamma$ Selection

Detecting the photon emitted during the $D_s^*$ radiative decay is crucial for the rejection of non-signal events in this analysis. The number of single bumps measured in the EMC rises exponentially for decreasing deposited energy (figure 3.5). Cuts are placed on both the laboratory frame and centre of mass frame photon energies to remove most of this low energy background. Cutting on the centre of mass energy is motivated by the physics of the event. For example, the photon is mono-energetic in the rest frame of the $D_s^*$ candidate. However, this information is incorporated into the $\Delta M$ distribution which is later used in the likelihood analysis. In addition, the laboratory frame energy cut is useful for rejecting low energy background photons which are detected predominantly in the forward regionof the EMC due to the asymmetric beam energies. The final chosen photon energy cuts are $E_{lab} > 0.05$ GeV and $E_{cms} > 0.1$ GeV.

A candidate photon is also required to be inconsistent with originating from a $\pi^0$ in the following way: if, when combined with any other photon candidate in the event, the photon candidate in question produces a $\pi^0$ with a mass in the range $0.115 < M_{\pi^0} < 0.155$ GeV/$c^2$ and a centre of mass energy greater than 0.2 GeV, then the candidate photon is rejected.

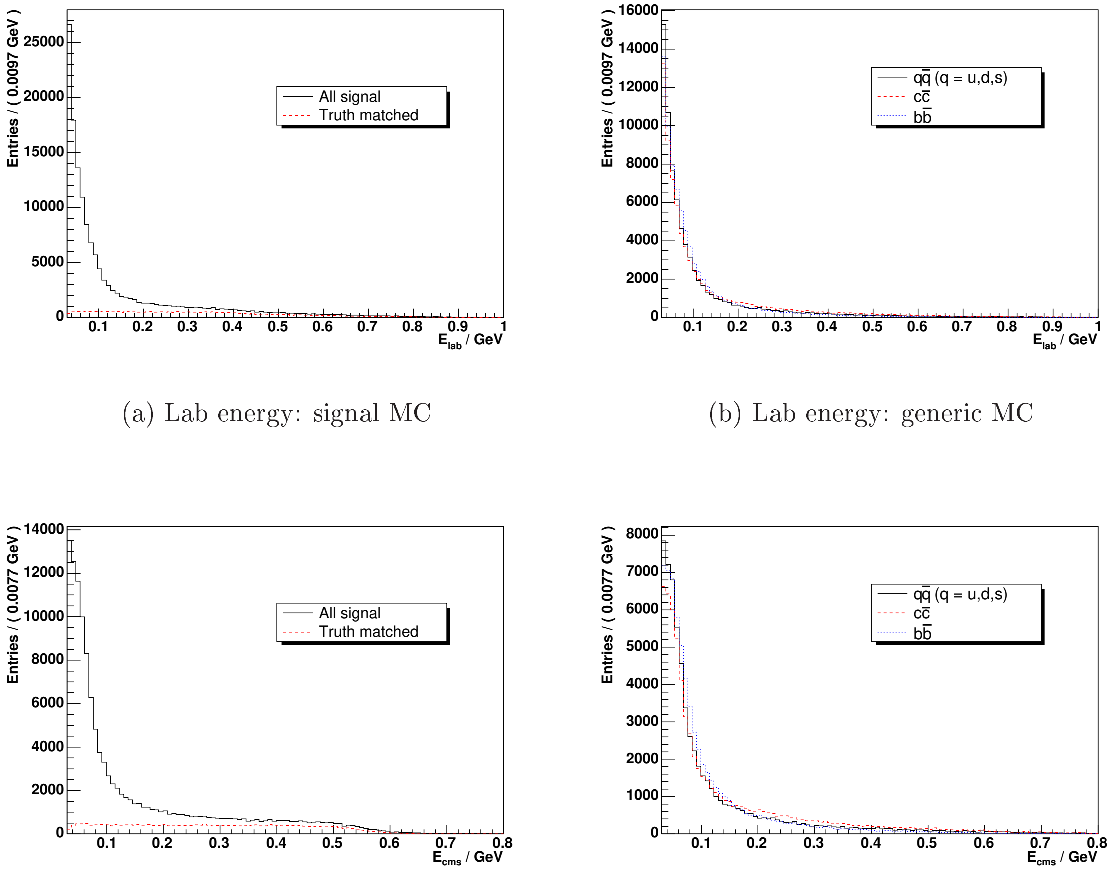


(a) Lab energy: signal MC

(b) Lab energy: generic MC

(c) Centre of mass energy: signal MC

(d) Centre of mass energy: generic MC

**Figure** 3.5: Reconstructed laboratory frame (top) and centre of mass frame (bottom) energy distributions of photons originating from the $D_s^{*\pm} \to D_s^{\pm}\gamma$ radiative process for $D_s^{\pm} \to K^{\pm}\pi^0$ signal MC (a,c) and generic MC (b,d).

The above selections aid in reducing the acceptance of low energy noise in the EMC and rejecting the small number of $D_s$ candidates originating from the strong decay $D_s^{*\pm} \to D_s^{\pm}\pi^0$.

### 3.4.4 Charged Track Particle Identification

Particle Identification (PID) for pions and kaons is achieved using a likelihood based selector [80] developed by the *BABAR* PID Working Group. The three charged particle detectors, namely the SVT, DCH and DIRC, all contribute to the likelihood

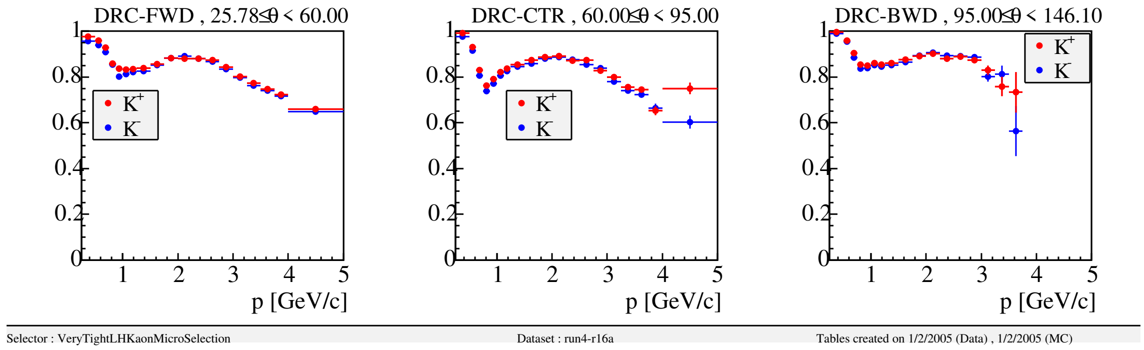


(a) Kaon selection efficiency

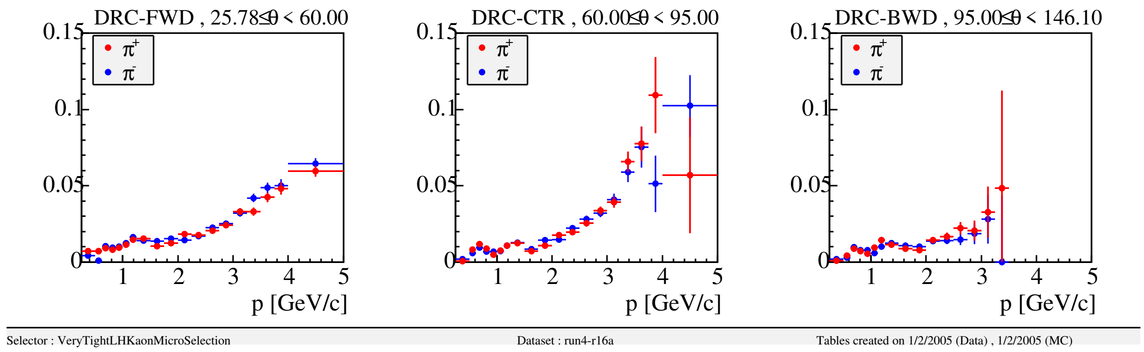


(b) Pion fake rate

**Figure** 3.6: The kaon selection efficiency (a) and pion fake rate (b) for the very tight kaon likelihood selector are shown as a function of both track momentum and polar angle. The plots are produced by the *BABAR* Particle ID Working Group at SLAC. The polar angle, $\theta$, is expressed in degrees.

value, $L$, multiplicatively (equation 3.1) and a value is computed for each of the $\pi/K/p$ particle hypotheses. The SVT and DCH contribute through energy loss measurements, $dE/dx$ of the particles that traverse them, while the DIRC contributes through measurements of a charged particle's Čerenkov angle.

$$L = L_{SVT} \times L_{DCH} \times L_{DIRC} \tag{3.1}$$

When selecting for a specific particle type, e.g. $K$, the ratios of likelihoods for the particle in question and the remaining two hypotheses are computed. Increasingly tighter cuts can be placed on these ratios to obtain purer kaon samples in

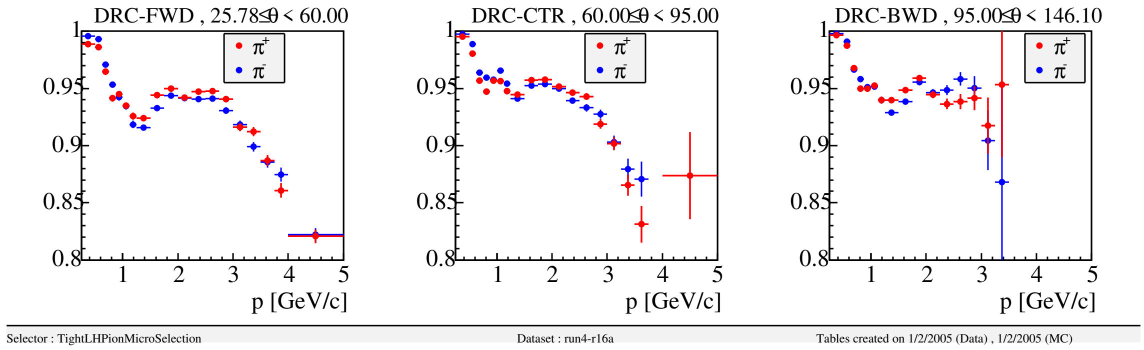


(a) Pion selection efficiency

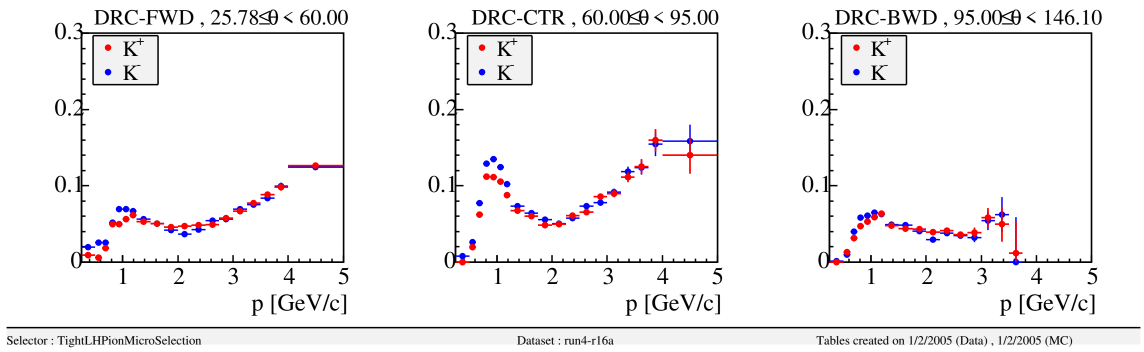


(b) Kaon fake rate

**Figure** 3.7: The pion selection efficiency (a) and kaon fake rate (b) for the tight pion likelihood selector are shown as a function of both track momentum and polar angle. The plots are produced by the *BABAR* Particle ID Working Group at SLAC. The polar angle, $\theta$, is expressed in degrees.

combination with optional electron and muon vetoes based on their respective selectors [81, 82].

The kaon PID selector chosen for this analysis is known as the very tight kaon likelihood selector. Performance plots for this selector as a function of both track momentum and polar angle can be seen in figures 3.6(a) and 3.6(b). Figure 3.6(a) shows the efficiency with which kaons are identified and figure 3.6(b) shows the rate at which pions are misidentified as kaons. Compared with other kaon selectors, the very tight selector has a lower pion fake rate and it achieves this at the expense of selection efficiency. The choice of this selector is sensible given the sizeable data sample available for this analysis.

For pion PID the chosen selector is the tight pion likelihood selector and is chosen for the same reasons outlined above in the case of kaon selection. The performance plots associated with this selector are shown in figures 3.7(a) and 3.7(b).

### 3.4.5 $K_S^0$ Selection

Reconstructed $K_S^0$ candidates provide a good means of rejecting background for the decay modes involving them. In addition to the good mass resolution (figure 3.8(a)), the decay length, $l$, is well measured at *BABAR* providing further enhancement of the signal to background ratio.

The decay length significance is defined as $l/\sigma_l$ where $\sigma_l$ is the error on the decay length as determined from the least squares fit to the decay tree. While a mass cut is good for reducing combinatoric background, the decay length provides an effective method to remove the background prevalent in the generic MC (figures 3.8(c) and 3.8(d)). The essentially Gaussian distribution of $l/\sigma_l$ centred around zero can be almost entirely removed with a well placed cut while retaining the vast majority of true $K_S^0$ candidates. Final cut values of $|M(K_S^0) - M(K_S^0)_{PDG}| < 0.01\ \text{GeV}/c^2$ and $l/\sigma_l > 3$ are chosen.

### 3.4.6 Decay Tree Sphericity

The largest source of background is that originating from light quark events. Event topology can be used to improve the signal to background ratio for this and $c\bar{c}$ background. The sphericity, $\mathcal{S}$, is the sum of the squares of the transverse momentum of each detected particle with respect to the event axis, and is defined [83] as

$$\mathcal{S} = \frac{3}{2}(\lambda_2 + \lambda_3) \tag{3.2}$$

where $\lambda_2$ and $\lambda_3$ are the second and third eigenvalues of the sphericity tensor respectively, which is defined as

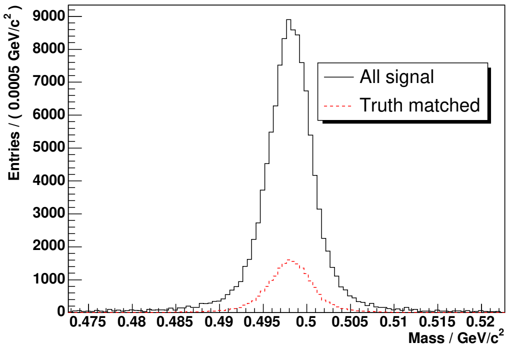


(a) $K_s^0$ mass: signal MC

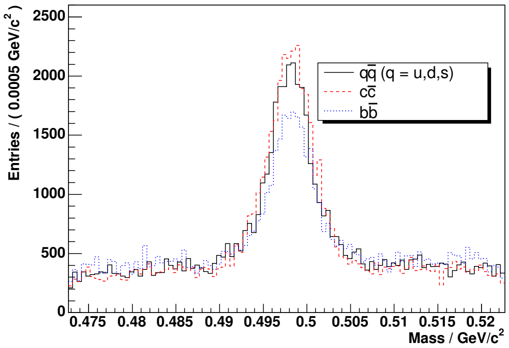


(b) $K_s^0$ mass: generic MC

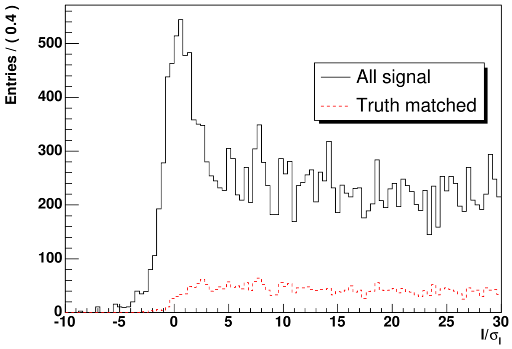


(c) $K_s^0$ decay length significance: signal MC

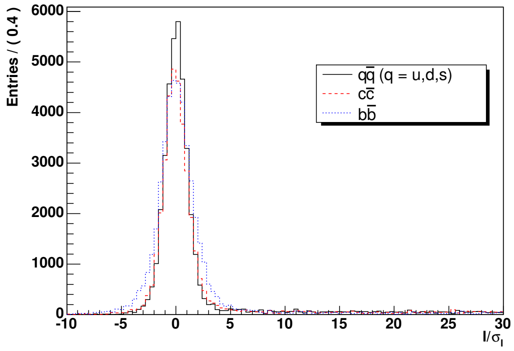


(d) $K_s^0$ decay length significance: generic MC

**Figure** 3.8: Reconstructed mass (top) and decay length significance (bottom) distributions of $K_s^0$ candidates in $D_s^\pm \to K^\pm K_s^0$ signal MC (a,c) and generic MC (b,d).

$$\mathcal{S}^{\alpha\beta} = \frac{\sum_{i=1}^{n} p_i^\alpha p_i^\beta}{\sum_{i=1}^{n} \mathbf{p}_i^2} \tag{3.3}$$

where $\alpha, \beta = 1, 2, 3$ represent the $x, y$ and $z$ components of the momentum vector $\mathbf{p}$, respectively. $\mathcal{S}$ is calculated with respect to the sphericity axis, which lies along the eigenvector corresponding to the largest eigenvalue of the sphericity tensor. For the analysis presented here, $\mathcal{S}$ of the decay tree is computed by only considering tracks and neutral objects used to reconstruct the full $D_s^*$ decay chain.

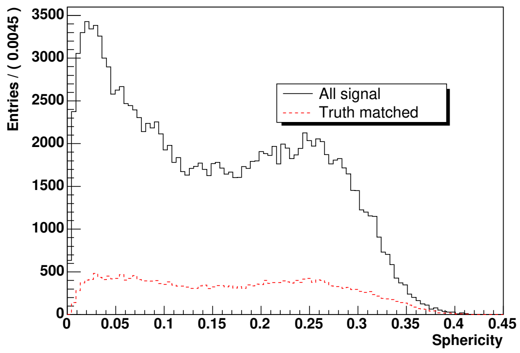


(a) Signal MC

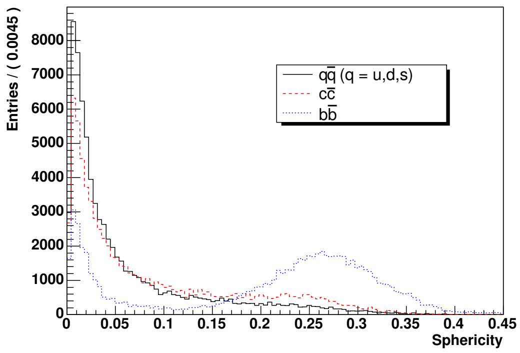


(b) Generic MC

**Figure** 3.9: The sphericity of all charged and neutral objects in the fully reconstructed decay tree for $D_s^{\pm} \to K^{\pm}\pi^0$ signal MC events (a) and generic MC events (b).

Typically, $q\overline{q}$ ($q = u, d, s$) events are jet-like and consequently their sphericity is strongly peaked close to zero as shown in figure 3.9(b). Conversely, signal events tend to be more isotropic (figure 3.9(a)) and some discrimination is achievable. A feature of $B$ decays at *BABAR* is their tendency to be isotropic (due to their production at the $\Upsilon(4S)$ threshold) and as a result the majority of $b\overline{b}$ events survive this selection. As with the $x_p$ cut, no cut value is decided at this stage because $\mathcal{S}$ is chosen as the second variable with which to optimise the likelihood analysis (see section 3.6).

### 3.4.7 Multiple Candidates

While each cut is placed on a single variable, they are not uncorrelated as indicated by the individual and combined cut selection efficiencies listed later in tables 3.9, 3.10, 3.11 and 3.12. After all cuts that have final values assigned are applied, the unavoidable issue of multiple candidates per event is addressed.

Table 3.5 lists the average number of multiple candidates per event and the fraction of events that contain more than one candidate. Numbers are included for all MC and data samples for reconstructed $D_s^{\pm} \to K^{\pm}\pi^0$ events. The key point here is

**Table** 3.5: The average number of multiple candidates per event together with the fraction of events that contain multiple candidates. Numbers shown here are for reconstructed $D_s^{\pm} \rightarrow K^{\pm}\pi^0$ events from both data and MC samples. All numbers are calculated with respect to the total number of events that survive after all final cuts have been applied.

| Sample | Average number of multiple candidates per event | Fraction of events containing multiple candidates |
|---|---|---|
| Signal MC | $1.133 \pm 0.021$ | $0.118 \pm 0.005$ |
| $q\overline{q}$ ($q = u, d, s$) MC | $1.163 \pm 0.055$ | $0.135 \pm 0.014$ |
| $B^+B^-$ MC | $1.102 \pm 0.093$ | $0.094 \pm 0.020$ |
| $B^0\overline{B^0}$ MC | $1.220 \pm 0.143$ | $0.182 \pm 0.040$ |
| $c\overline{c}$ MC | $1.136 \pm 0.040$ | $0.112 \pm 0.009$ |
| $\tau^+\tau^-$ MC | $1.083 \pm 0.434$ | $0.083 \pm 0.087$ |
| Data | $1.136 \pm 0.042$ | $0.115 \pm 0.010$ |

that the number of multiple candidates from MC events, averaged over all modes, evaluates to $\sim 1.15$ and is compatible with the number observed in data, hence this effect appears to be well described by the MC simulation.

The best candidate representing the head of the decay tree is chosen by taking the one with the maximum value of $x_p$. The maximum normalised momentum is used because $D_s^*$ mesons produced in $c\overline{c}$ fragmentation are expected to be fast. Additionally, all background levels reduce exponentially with increasing $x_p$ (figure 3.3(b)). An unavoidable result of selecting a best candidate in this manner is a distortion of the $x_p$ distribution, which could have the potential to introduce bias. However, the lack of knowledge of the $x_p$ spectrum is accounted for in the form of a systematic error which is described later in detail in section 4.7.2.

### 3.4.8 Significant Remaining Backgrounds

Of the generic non-peaking backgrounds, the light quark background ($q = u, d, s$) is the largest remaining after cut and best candidate selections have been applied. The statistical significance of a result depends largely on how well this background can be rejected. Both $b\overline{b}$ and $\tau^+\tau^-$ events are rejected with efficiencies over one and two orders of magnitude smaller than that of the light quark background, and as a result these events are largely insignificant.

The $c\bar{c}$ events surviving the selection process are the most challenging to accomodate. Their selection efficiency, as determined from MC samples, is approximately half that of the light quark background for all reconstructed modes. The challenge lies in modelling the peaking components of this sample in the variables chosen for the likelihood analysis: $M_{D_s}$ and $\Delta M$. Reconstructed events containing a genuine radiative decay of any $D^{*0}$, $D^{*\pm}$ or $D_s^{*\pm}$ meson will peak in $\Delta M$ and be indistinguishable from the signal channel in that variable. A similar peaking component is observed in the $M_{D_s}$ distribution, centred at the nominal $D_s$ mass. The most problematic of these fake $D_s$ mesons are those where a charged pion is misidentified as a kaon when fully reconstructing a genuine $D^{\pm}$ decay. The extra mass given to a charged pion, as a result of applying a kaon mass hypothesis, can shift a $D^+ \to \pi^+\pi^0$ or $D^{\pm} \to \pi^{\pm}K_S^0$ decay causing them to peak at the $D_s$ mass and fake a signal event. These issues are discussed in more detail and resolved in section 3.5.6.

## 3.5 Maximum Likelihood Analysis

### 3.5.1 The Likelihood Technique

The RooFit toolkit for data modeling [84] was developed at *BABAR* and is used here to perform the maximum likelihood analysis. In provides a convenient interface to ROOT [85], the object-oriented analysis framework developed at CERN, and utilises the Minuit [86] minimisation routines therein.

When analysing a data sample containing $N$ measurements $\{x_1, x_2, x_3, \ldots, x_N\}$, an estimator $\hat{a}$, which is a function of the $x_i$, can be used to determine numerical properties of the distribution. Here, the $x_i$ are assumed to be drawn from a known Probability Density Function (PDF), $P(x; a)$, where $a$ now represents some parameter of the PDF, for example the mean of a Gaussian function. If the $x_i$ are uncorrelated, the probability of the set $\hat{a}\{x_1, x_2, x_3, \ldots, x_N\}$ is given by the product of individual probabilities and is called the likelihood, defined as

$$\begin{aligned} L(x_1, x_2, \ldots, x_N; a) &= P(x_1; a)P(x_2; a) \cdots P(x_N; a) \\ &= \prod P(x_i; a) \end{aligned} \tag{3.4}$$

The procedure is to determine the value of $a$ that yields the maximum probability or likelihood given the data sample. Because it is more convenient, the natural logarithm of the likelihood is taken and the numerical routines used in this analysis minimise the quantity $-\ln L$.

Determination of event yields is achieved through the use of the extended maximum likelihood function. Instead of the normalised PDF $P(x; a)$, the function $Q(x; a)$ is used whose integral with respect to $x$ gives the expected number of events, $\nu$, instead of 1. Since $Q(x; a)$ predicts $\nu$ events, the likelihood is multiplied by the Poisson probability of obtaining $N$ events given a mean of $\nu$,

$$\begin{aligned} \ln L &= \ln(e^{-\nu}\nu^N) + \sum \ln P(x_i; a) \\ &= -\nu + \sum \ln[\nu P(x_i; a)] \\ &= -\nu + \sum \ln Q(x_i; a) \end{aligned} \tag{3.5}$$

where the $N!$ term has been dropped since it is not a function of $a$ or $\nu$. As the normalisation, $\nu$, of $Q(x_i; a)$ is increased, the first term in equation 3.5 decreases the likelihood, while the second increases it. The maximum $\ln L$ will yield the most probable value of $\nu$ given the set of $x_i$.

### 3.5.2 General Approach

Extracting the number of signal events from the final data samples is achieved using a 2D extended maximum likelihood fit. The fit is chosen to be two dimensional to improve the signal to background discrimation. This is particularly useful for discriminating between signal and peaking backgrounds since the former will peak in both dimensions while most of the latter will only peak in one or the other. For simplicity, fitting variables are chosen such that they are uncorrelated for background events and poorly reconstructed signal events.

The plane defined by the fitting variables is described using the product of two Probability Density Functions (PDF), each parameterising one of the variables. All signal and background components are parameterised individually from high statistics Monte Carlo samples, and are later combined to perform an extended likelihood fit to data.

### 3.5.3 Fitting Variables

The variables $M_{D_s}$ and $\Delta M$ are essentially uncorrelated for both reconstructed signal and background MC events (figure 3.10(a)) and as such are good choices of fitting variables. Well reconstructed signal events are distinguishable in the plane from the light quark background (figure 3.10(b)) which is flat across the whole region. In figure 3.10(a) the horizontal band is caused by events where a properly reconstructed $D_s$ is combined with a random photon. The less populated vertical band represents poorly reconstructed $D_s$ mesons combined with the correct photon from the radiative $D_s^*$ decay.

The $M_{D_s}$ and $\Delta M$ range over which the likelihood analysis is performed is chosen such that the signal is situated approximately in the centre of the plane, which is subsequently defined as $1.8 < M_{D_s} < 2.1$ GeV/$c^2$ and $0.1 < \Delta M < 0.2$ GeV/$c^2$. Throughout the analysis from this point onwards, all events falling outside this fitting region are ignored.

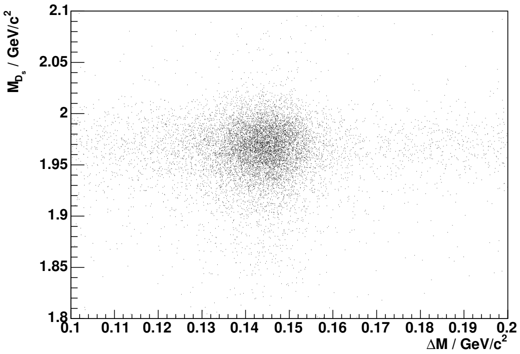


(a) Signal MC

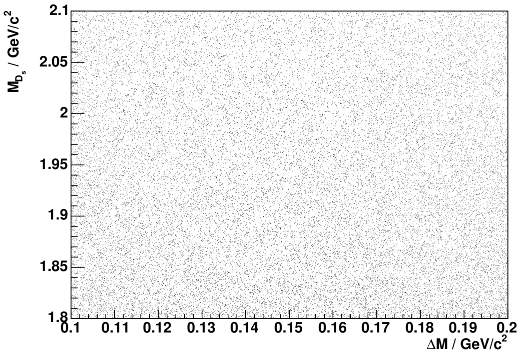


(b) Generic $q\overline{q}$ $(q = u, d, s)$ MC

**Figure** 3.10: Reconstructed $D_s^{\pm} \to K^{\pm}\pi^0$ signal MC events (a) in the $M_{D_s}$, $\Delta M$ plane. Well reconstructed events are concentrated in the dark, central region. The light quark background (b) is essentially featureless in the plane.

### 3.5.4 Signal Parameterisation

Reconstructed signal MC events for all modes are initially split into two categories: truth-matched and non-truth-matched. The truth-matched events have the extra property of each particle in the reconstructed decay chain being consistent with an original generated MC particle before the event passed through the simulation. As such, the truth-matched events are expected to describe those signal events that are well reconstructed.

Once parameterised, the PDF describing the truth-matched events has its parameters fixed. It now remains to parameterise the non-truth-matched events in the signal MC sample. The truth-matching algorithm is known to have an imperfect efficiency, therefore a small number of 'true' events populate the non-truth-matched sample. These true events are assumed to be well described by the truth-matched PDF defined previously. To accommodate these, the truth-matched signal PDF is added to a new PDF designed to describe the remainder of the non-truth-matched events which are termed self cross-feed (SCF). Consequently, the signal samples are now divided into two alternative sets of events called truth and SCF. The SCF component essentially describes partially reconstructed events which will not be considered as part of the signal yield from the fit to data.

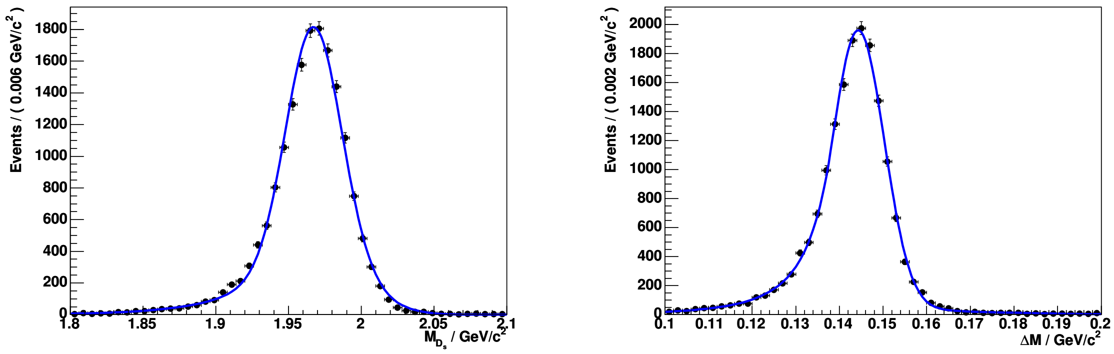


(a) (b)

**Figure** 3.11: PDFs (curves) describing $M_{D_s}$ (a) and $\Delta M$ (b) for truth-matched $D_s^\pm \to K^\pm\pi^0$ signal MC events (points). Each plot is a projection of the 2D PDF in the respective variable.

Parameterisations for truth-matched $D_s^\pm \to K^\pm\pi^0$ events are shown in figure 3.11. The $M_{D_s}$ PDF comprises primarily a function introduced by the Crystal Ball (CB) collaboration defined as

$$f_{CB} = \begin{cases} a\,(b - \frac{x-\mu}{\sigma})^{-n} & \text{if } (x-\mu)/\sigma \leqslant \alpha \\ \exp(-\frac{(x-\mu)^2}{2\sigma^2}) & \text{if } (x-\mu)/\sigma > \alpha \end{cases} \tag{3.6}$$

where $x$ is the dependent variable, $\mu$, $\sigma$, $n$ and $\alpha$ are free parameters and $a$ and $b$ are chosen such that the function and its first derivative are continuous at $(x-\mu)/\sigma = \alpha$. The CB function is used to describe the radiative tail introduced by the energy resolution of the EMC. A small Gaussian component accounts for the remainder and achieves a better combined PDF lineshape. Similarly, the $\Delta M$ distribution is described by a CB function and a Gaussian function, with the CB function representing the vast majority of the PDF. For both variables the Gaussian components share the mean of the CB function and essentially they are required to better describe the tails of the distributions. The combined 2D PDF in the plane is the multiplication of these two composite PDFs and is used to represent true signal events.

Non-truth-matched events for the $D_s^\pm \to K^\pm\pi^0$ mode are parameterised using a PDF defined as the sum of the truth-matched PDF with fixed parameters and a

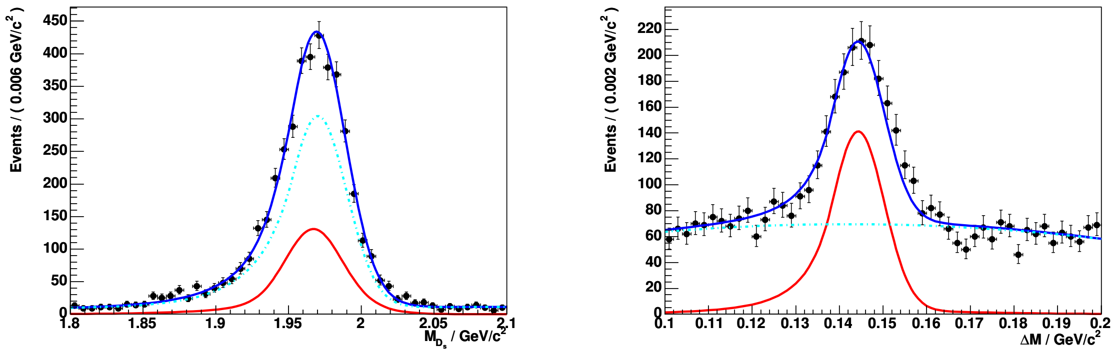


(a) (b)

**Figure** 3.12: PDFs (curves) describing $M_{D_s}$ (a) and $\Delta M$ (b) for non truth-matched $D_s^\pm \to K^\pm\pi^0$ signal MC events (points). The solid red line is the truth-matched PDF representing the true events in the non-truth-matched sample. The dot-dashed cyan line represents poorly reconstructed signal events which are labelled as SCF. The solid blue line is the sum of the two components.

SCF PDF that is to be determined. A $2^{nd}$ order polynomial added with a Gaussian describes the SCF events in $M_{D_s}$, which is multiplied by a $2^{nd}$ order polynomial used to describe $\Delta M$. The resulting fit (figure 3.12) implies that a significant number, $\sim 27\%$ (table 3.6), of well reconstructed signal are present in the non-truth-matched sample. The vast majority of SCF events have well reconstructed $D_s$ mesons in the decay tree but almost no well reconstructed $D_s^*$ mesons.

The method and PDF lineshapes used to fit the true signal and SCF components for the $D_s^\pm \to K^\pm\pi^0$ mode are also used for the $D_s^\pm \to \pi^\pm\pi^0$ decay mode. The results of these fits can be seen in figure 3.13. It is evident that the PDF projection in $M_{D_s}$ is not ideal in that the peak appears slightly shifted from the MC data points. However, this lineshape is a good description for the $D_s^\pm \to K^\pm\pi^0$ mode and a signal for the $D_s^\pm \to \pi^\pm\pi^0$ is not expected to be observed. Therefore to remain consistent this PDF is considered acceptable and no effort is made to improve it beyond its current form.

The same method is employed in describing the signal MC samples for the $D_s^\pm \to K^\pm K_S^0$ and $D_s^\pm \to \pi^\pm K_S^0$ modes as was used for the final states containing a $\pi^0$.

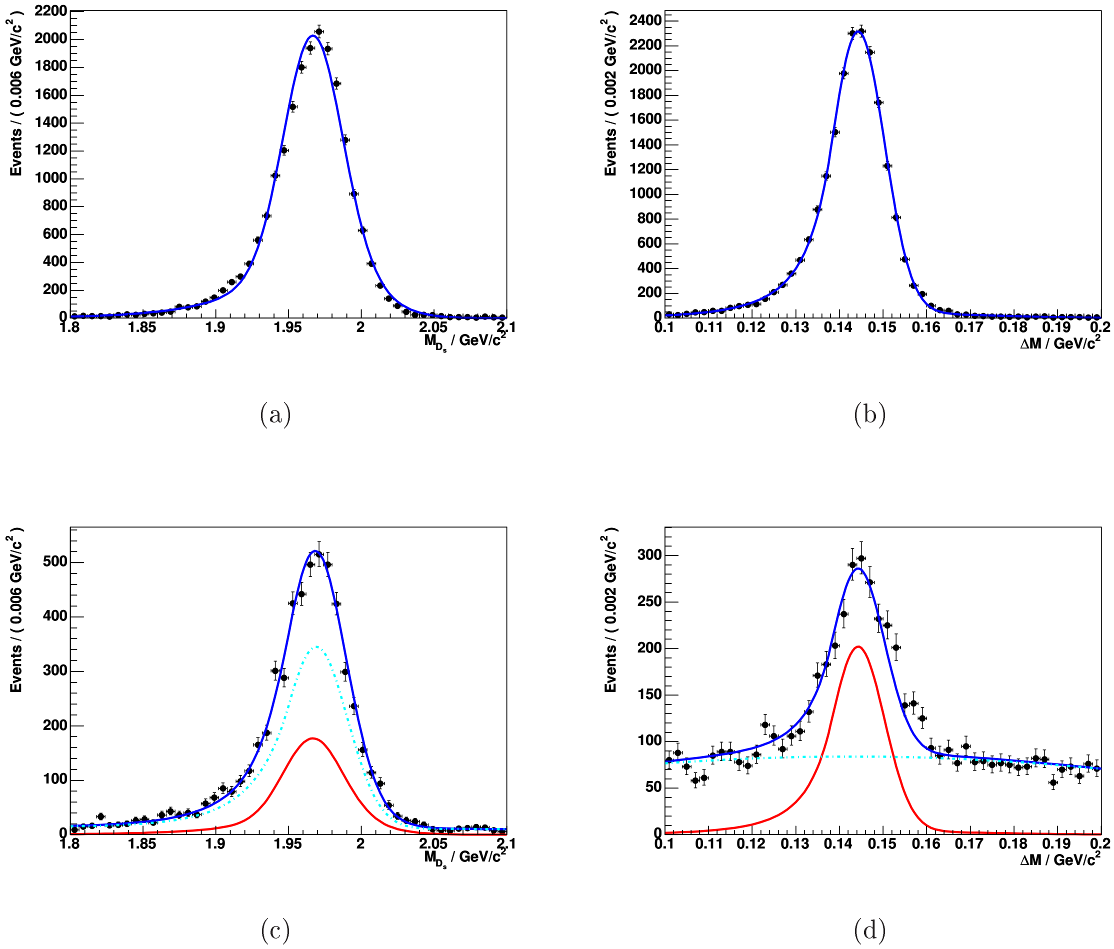


**Figure** 3.13: Figures (a) and (b) show PDFs for truth-matched $D_s^{\pm} \to \pi^{\pm}\pi^0$ signal MC events while figures (c) and (d) show the subsequent SCF parameterisation. The solid red line represents the PDF parameterised in figures (a) and (b) while the dot-dashed cyan line represents the SCF events.

However, there is a significant difference in that no radiative tail is present in the $M_{D_s}$ distribution and so the PDF for that variable is simply the sum of two Gaussians which share a common mean. The final parameterisations for $D_s^{\pm} \to K^{\pm}K_S^0$ and $D_s^{\pm} \to \pi^{\pm}K_S^0$ signal MC events are shown in figures 3.14 and 3.15 respectively.

Finally, all PDF components are fixed and an extended likelihood fit comprising truth and SCF components is performed on the full set of reconstructed signal MC events separately for each mode. The two yields from the fit are needed to define how many truth and SCF events should be generated for toy studies. The truth

**Table** 3.6: The percentage of events described by the truth PDF in the non-truth-matched signal MC sample and total signal MC sample for each signal channel.

| Mode | Percentage of events described by truth PDF / % | | Implied truth matching efficiency / % |
|---|---|---|---|
| | In non-truth-matched signal MC fit sample | In total signal MC fit sample | |
| $D_s^\pm \to K^\pm\pi^0$ | 27 | 85 | 93 |
| $D_s^\pm \to \pi^\pm\pi^0$ | 31 | 85 | 92 |
| $D_s^\pm \to K^\pm K_S^0$ | 14 | 82 | 96 |
| $D_s^\pm \to \pi^\pm K_S^0$ | 18 | 82 | 94 |

yield is also used in calculating the signal reconstruction efficiency.

The percentage of signal MC events described by the signal PDFs for all modes are shown in table 3.6. The first column presents the number of true events found in the non-truth-matched MC sample, the second presents the number found in the total signal MC sample, and the third presents the implied efficiency of the truth-matching algorithm. The truth-matching inefficiencies are believed to be largely due to photon reconstruction, but not entirely due to the $\gamma$ from the $D_s^*$ decay. The $\sim 2-3\%$ drop in efficiency when replacing a $K_S^0$ with a $\pi^0$, and hence two additional photons, appears to support this argument.

The most striking difference between the signal MC events for modes with and without a $\pi^0$ is the much improved $M_{D_s}$ resolution that is achieved when reconstructing the $D_s$ purely from charged tracks. As a result, the $D_s^\pm \to K^\pm\pi^0$ and $D_s^\pm \to \pi^\pm\pi^0$ decay modes will be more difficult to isolate in the data.

### 3.5.5 Smooth Background Parameterisation

As indicated by figure 3.10(b) the $M_{D_s}$, $\Delta M$ plane for $q\overline{q}$ ($q = u, d, s$) events is basically a smooth distribution with no peaking components. The same is also true for the $B^+B^-$, $B^0\overline{B}^0$ and $\tau^+\tau^-$ generic MC samples. As a result of low selection efficiencies for the generic $b\overline{b}$ and $\tau^+\tau^-$ events the statistics of such samples in the plane are limited and so the events are added to the light quark sample and a single

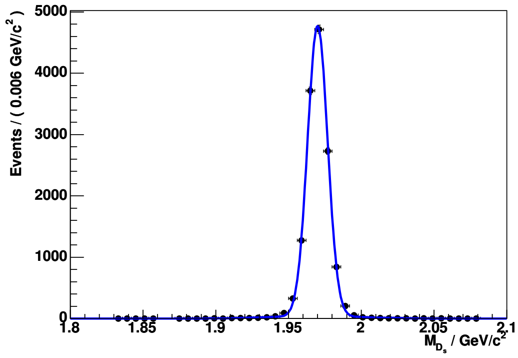


(a)

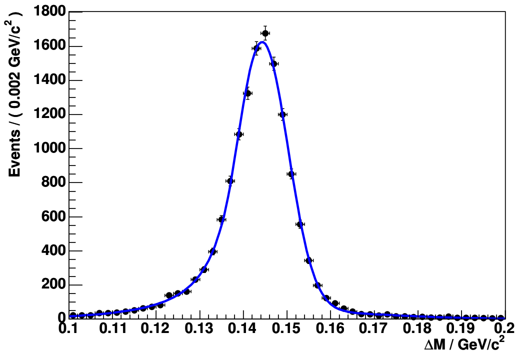


(b)

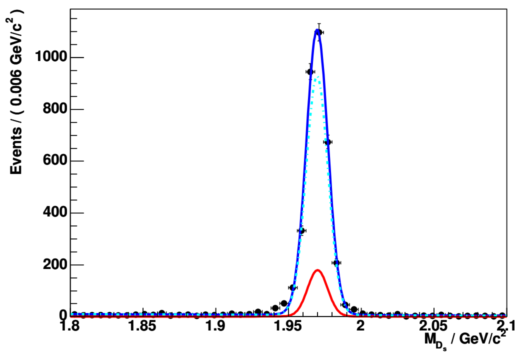


(c)

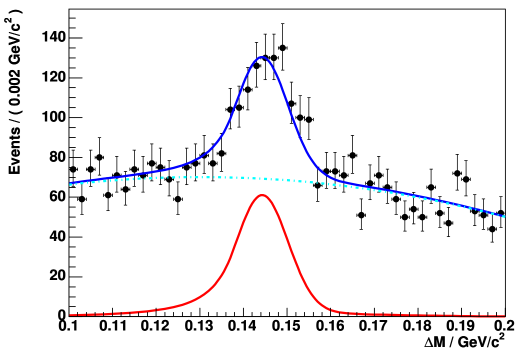


(d)

**Figure** 3.14: Figures (a) and (b) show PDFs for truth-matched $D_s^{\pm} \rightarrow K^{\pm}K_S^0$ signal Monte Carlo events while figures (c) and (d) show the subsequent SCF parameterisation. The solid red line represents the PDF parameterised in figures (a) and (b) while the dot-dashed cyan line represents the SCF events.

PDF is created to describe all four components. This is justified because it is not necessary to discriminate between these backgrounds when fitting the data.

A product of two $2^{nd}$ order polynomials is sufficient to parameterise the sample for all four reconstructed modes. Smooth backgrounds for modes containing a $\pi^0$ and $K_S^0$ are shown in figures 3.16 and 3.17 respectively. Obtaining a fixed PDF for the smooth background is required solely for the purpose of toy studies because in the final fit to data the four parameters of this particular PDF are allowed to float.

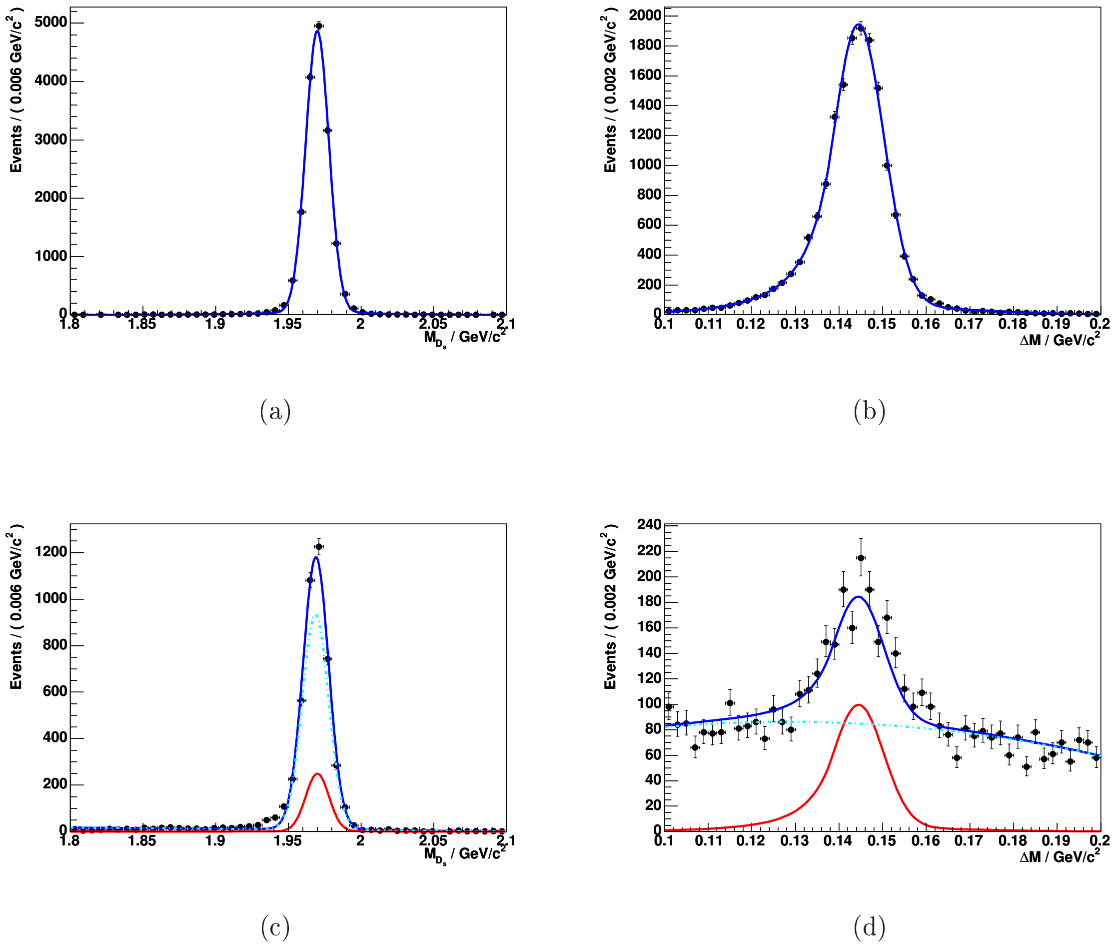


**Figure** 3.15: Figures (a) and (b) show PDFs for truth-matched $D_s^{\pm} \to \pi^{\pm} K_S^0$ signal Monte Carlo events while figures (c) and (d) show the subsequent SCF parameterisation. The solid red line represents the PDF parameterised in figures (a) and (b) while the dot-dashed cyan line represents the SCF events.

### 3.5.6 Peaking Background Parameterisation

Generic $c\bar{c}$ MC events are the cause of all peaking components in $M_{D_s}$ and $\Delta M$ in the analysis other than the poorly reconstructed signal events accounted for by the SCF PDFs (section 3.5.4). Features in the $c\bar{c}$ background mean it has to be treated differently for $K^{\pm}\pi^0$ and $\pi^{\pm}\pi^0$ final states and for those modes containing a $K_S^0$. For all reconstructed modes except for $D_s^{\pm} \to K^{\pm}\pi^0$, the generic $c\bar{c}$ MC data contains the signal decay channel. During processing these events are tagged and completely removed such that the $c\bar{c}$ background can be parameterised in the

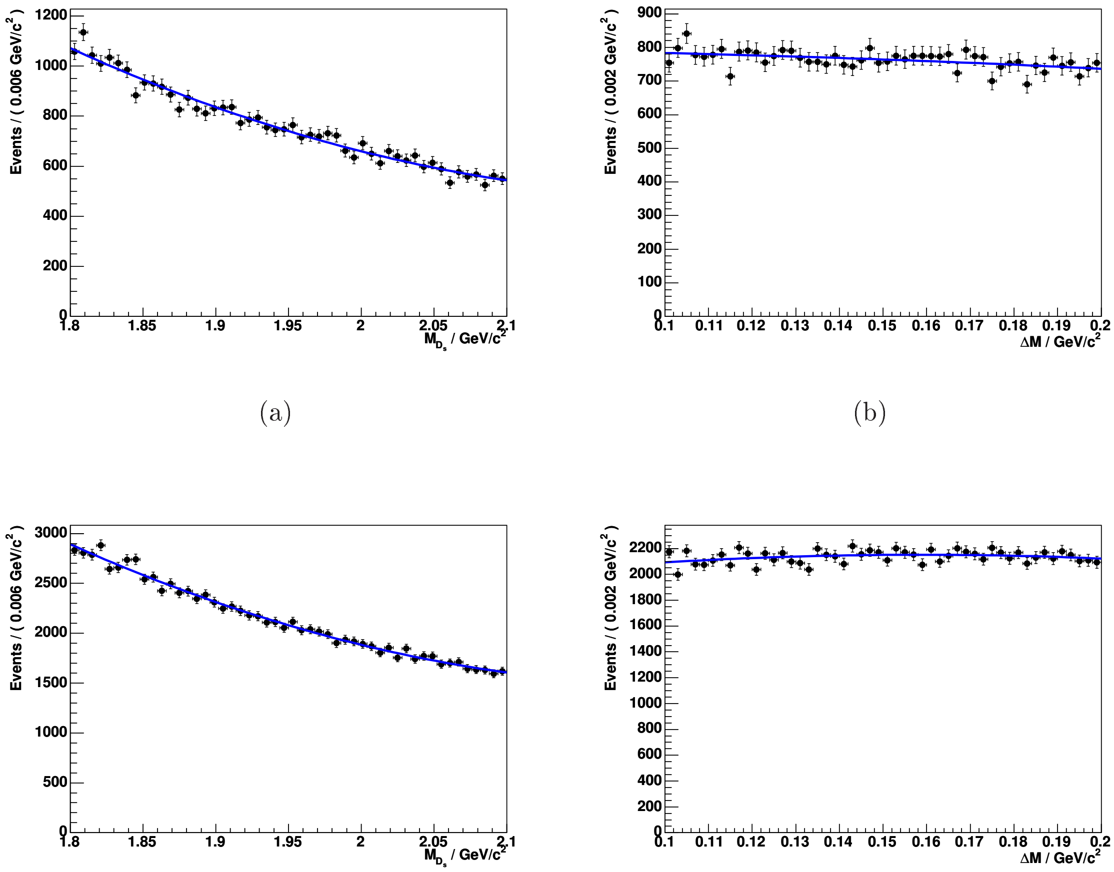


(a) (b)

(c) (d)

**Figure** 3.16: Parameterisations of the $q\overline{q}$ ($q = u, d, s$), $b\overline{b}$ and $\tau^+\tau^-$ smooth background components for $D_s^{\pm} \to K^{\pm}\pi^0$ ((a) and (b)) and $D_s^{\pm} \to \pi^{\pm}\pi^0$ ((c) and (d)).

absence of signal events. The distributions of $c\overline{c}$ events in the $M_{D_s}$, $\Delta M$ plane for all reconstructed modes are not smooth and so more sophisticated PDFs are required for their parameterisation compared to the smooth background case.

A significant peaking component in $\Delta M$ is observed for the $D_s^{\pm} \to K^{\pm}\pi^0$ and $D_s^{\pm} \to \pi^{\pm}\pi^0$ decay modes, situated at the same point as the expected signal component. An extra feature is that the relative size of this peak, compared to the underlying smooth $\Delta M$ distribution, is observed to change with $M_{D_s}$. Specifically, the peak gradually disappears for increasing $M_{D_s}$ and the relationship is found to be exponential. The events causing this peak are those that contain a genuine radiative decay of a $D_{(s)}^*$ meson where the $D_{(s)}$ has been incorrectly reconstructed. If these

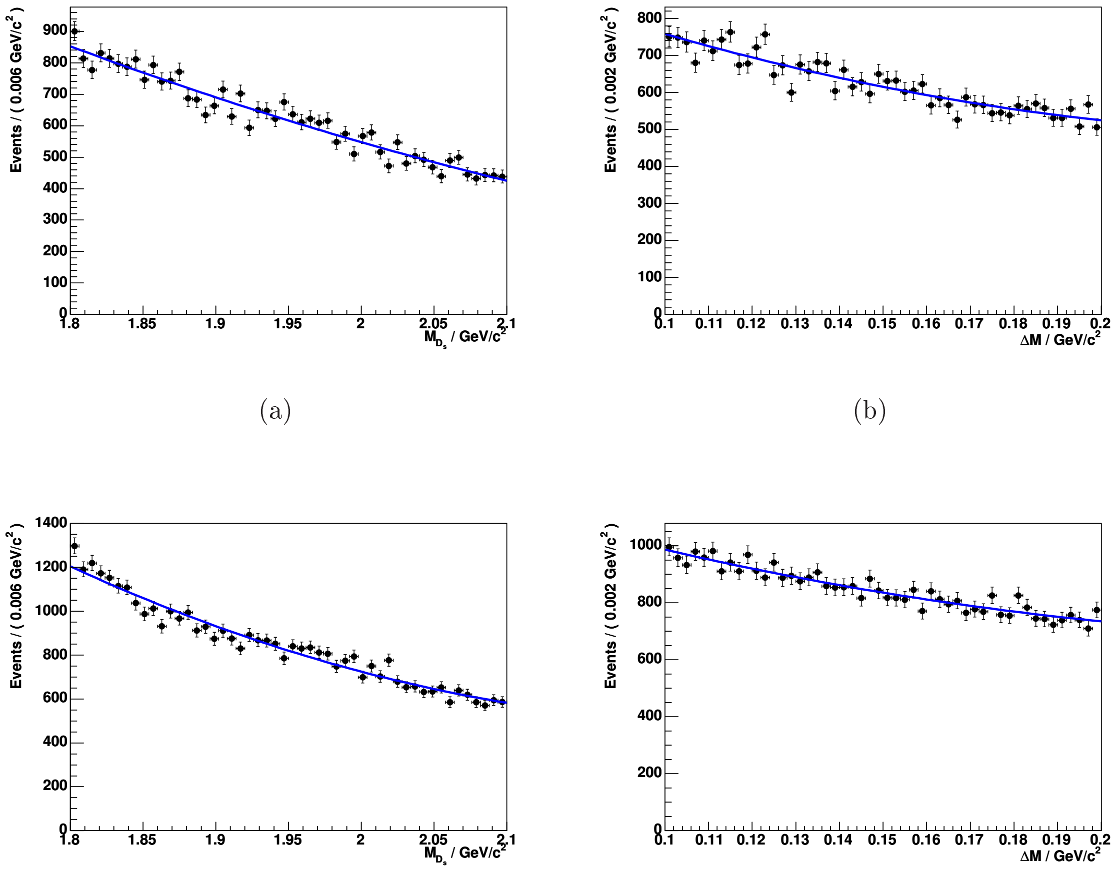


(a) (b) (c) (d)

**Figure** 3.17: Parameterisations of the $q\overline{q}$ ($q = u, d, s$), $b\overline{b}$ and $\tau^+\tau^-$ smooth background components for $D_s^\pm \to K^\pm K_S^0$ ((a) and (b)) and $D_s^\pm \to \pi^\pm K_S^0$ ((c) and (d)).

events were correctly reconstructed then a peak would be observable in $M_{D_s}$, but this is not the case. At lower values of $M_{D_s}$, many more random combinations exist that can be combined with photons from genuine radiative decays.

The PDF describing this background is the sum of two separate 2D PDFs. One component is a product of two polynomials to describe the underlying smooth background as in the case described in section 3.5.5. The second component is the product of a Gaussian in $\Delta M$ and an exponential in $M_{D_s}$. The parameter governing the relative amounts of each component in the composite PDF is allowed to float in the fit. Figure 3.18 shows the projection of the fitted PDF in each of the two fitting

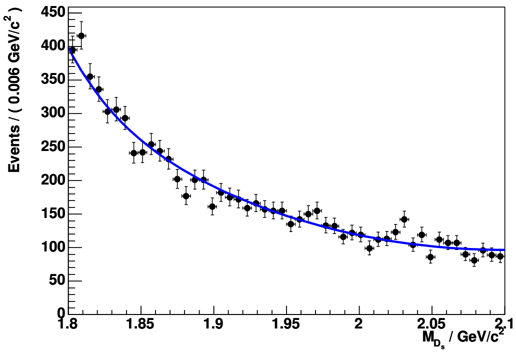


(a)

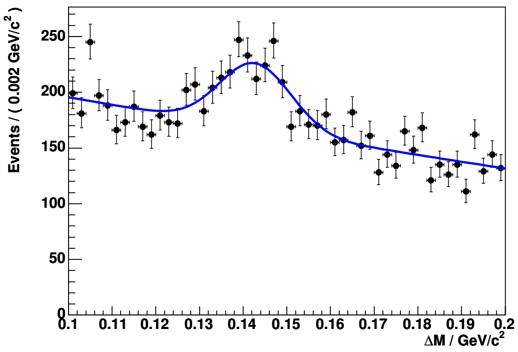


(b)

**Figure** 3.18: Projections in $M_{D_s}$ (a) and $\Delta M$ (b) of the PDF describing generic $c\bar{c}$ MC events when reconstructing the $D_s^{\pm} \to K^{\pm}\pi^0$ mode. There are two components to the PDF (not shown here) that represent the underlying smooth background and the peaking component separately.

variables for the $D_s^{\pm} \to K^{\pm}\pi^0$ case.

The model described above also applies when reconstructing $D_s^{\pm} \to \pi^{\pm}\pi^0$ decays in the generic $c\bar{c}$ MC sample. However, there exists an extra component in this case to describe the correct reconstruction of genuine $D^+ \to \pi^+\pi^0$ decays since the branching fraction of this process is measured to be $(1.33 \pm 0.22) \times 10^{-3}$ [17]. It is not present when reconstructing $D_s^{\pm} \to K^{\pm}\pi^0$ because the process $D^{\pm} \to K^{\pm}\pi^0$ is not known to occur at a significant level. The current experimental limit is $\mathcal{B}(D^{\pm} \to K^{\pm}\pi^0) < 4.2 \times 10^{-4}$ with 90% confidence [87]. The $D^+ \to \pi^+\pi^0$ component peaks at $\sim$ 1.87 GeV/$c^2$ in $M_{D_s}$ but the distribution of these events in $\Delta M$ is approximately smooth. This is due to the fact that the branching fraction $\mathcal{B}(D^{*\pm} \to D^{\pm}\gamma) = (1.6 \pm 0.4) \times 10^{-2}$ yielding an insignificant number of $D^+ \to \pi^+\pi^0$ events originating from a radiative decay of a $D^*$ meson.

The PDF for the $D^+ \to \pi^+\pi^0$ component is a product of a CB in $M_{D_s}$ and a $2^{nd}$ order polynomial in $\Delta M$. The events containing these decays can be identified and isolated within the charm sample such that the PDF can be parameterised independently from the PDF describing the remainder of the $c\bar{c}$ background. The full PDF, involving both the peaking $D$ decay component and the component representing the

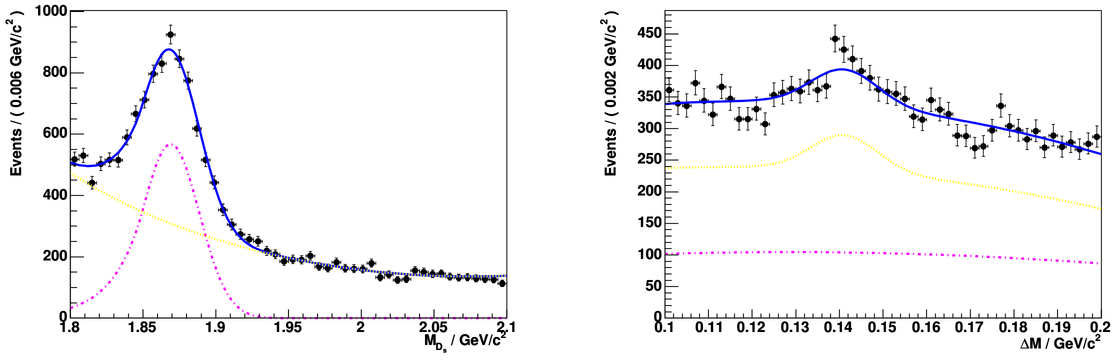


(a) (b)

**Figure** 3.19: Projections in $M_{D_s}$ (a) and $\Delta M$ (b) of the PDF describing generic $c\bar{c}$ MC events when reconstructing the $D_s^\pm \to \pi^\pm \pi^0$ mode. There are two components depicted; one representing well reconstructed genuine $D^+ \to \pi^+\pi^0$ decays (dot-dashed magenta line) and another representing poorly reconstructed $D_s$ mesons of which some are combined with a photon from a genuine radiative $D^*_{(s)}$ decay (dotted yellow line).

remaining $c\bar{c}$ events, can be seen in figure 3.19.

Modelling of the $c\bar{c}$ background must be performed differently from that described above for the two modes involving a $K_S^0$ in the final state. The major difficulty for modes involving a $K_S^0$ is that the $M_{D_s}$, $\Delta M$ plane has many more features that make it difficult to describe with a small number of PDFs. Instead, a non-parametric 2D PDF is constructed from the MC events. Like a parametric method, a non-parametric method is concerned with determining the parent distribution from which a set of data has been drawn. However, the non-parametric approach allows the model dependence to be removed in the PDF estimation. Each data point becomes a degree of freedom and is represented by a kernel with a Gaussian distribution, hence its influence on neighbouring data points decreases with increasing separation. Details pertaining to kernel estimation and the merits of non-parametric techniques can be found elsewhere [88].

For both the $D_s^\pm \to K^\pm K_S^0$ and $D_s^\pm \to \pi^\pm K_S^0$ modes their analogous decays involving $D$ mesons have significant branching fractions [17]. The $D$ decays are described by

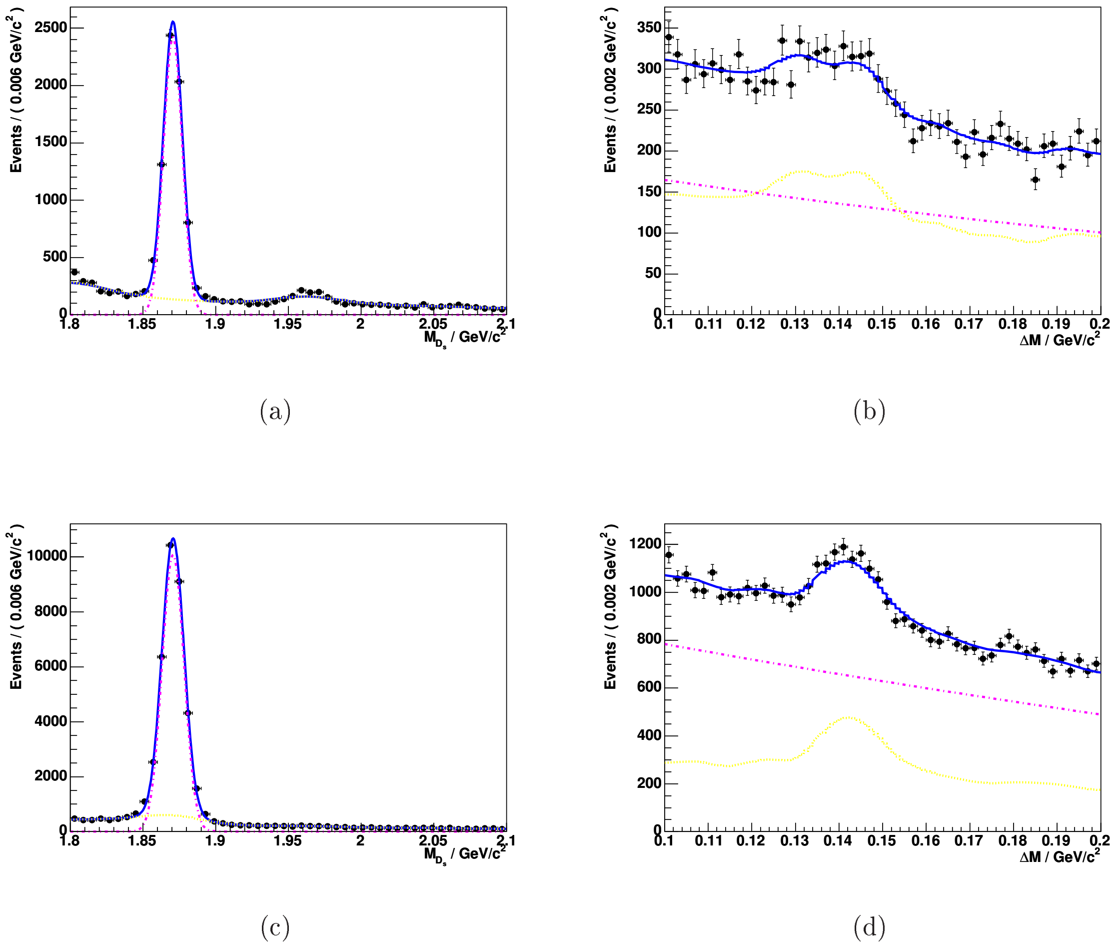


(a) (b)

(c) (d)

**Figure** 3.20: Projections in $M_{D_s}$ and $\Delta M$ of the PDF describing generic $c\bar{c}$ MC events when reconstructing the $D_s^\pm \to K^\pm K_S^0$ and $D_s^\pm \to \pi^\pm K_S^0$ decay modes. In each case there are two components drawn; one representing correctly reconstructed $D^\pm \to K^\pm K_S^0$ (a,b) and $D^\pm \to \pi^\pm K_S^0$ (c,d) decays (dot-dashed magenta lines) and the non-parametric PDF describing the remaining generic background (dotted yellow lines).

the product of a Gaussian in $M_{D_s}$ and a second order polynomial in $\Delta M$. The $c\bar{c}$ background for the $D_s^\pm \to K^\pm K_S^0$ and $D_s^\pm \to \pi^\pm K_S^0$ decay modes is then described by the sum of a non-parametric PDF added to the PDF describing the relevant $D$ decay mode (figure 3.20).

For all modes, it is crucial to consider backgrounds that could potentially mimic signal events. When reconstructing $D_s$ decay modes with a charged kaon some $D$ decays can peak at the $D_s$ mass. For example, if the decay $D^+ \to \pi^+\pi^0$ is correctly reconstructed but the pion is mis-identified and assigned a kaon mass hypothesis, the resultant composite candidate will be shifted from its true $D$ mass up near to the nominal $D_s$ mass. In the case of $D_s^{\pm} \to K^{\pm}\pi^0$, there is no observed peak at the $D_s$ mass for the generic $c\bar{c}$ MC events (figure 3.18(a)) implying that the number of $D^+ \to \pi^+\pi^0$ decays reconstructed in this manner is small for this analysis. However, if the $D$ mesons originate from $D^{*\pm} \to D^{\pm}\gamma$ decays then the events peak in both $M_{D_s}$ and $\Delta M$, and are therefore spurious signal events. The same is true when reconstructing $D_s^{\pm} \to K^{\pm}K_S^0$ where a small but significant population is seen to peak close to the $D_s$ mass (figure 3.20(a)) which arises from the correct reconstruction of $D^{\pm} \to \pi^{\pm}K_S^0$ with a pion mis-identified as a kaon. While the non-parametric PDF will attempt to model these events in the $M_{D_s}$, $\Delta M$ plane the result is not perfect. Although the overall effect here is expected to be small, the contribution of these events is estimated later in section 4.5.5 for inclusion in the systematic uncertainty.

Final states involving a charged pion do not suffer from the peaking background discussed above since a misidentification of a kaon in $D^{\pm} \to K^{\pm}\pi^0$ and $D^{\pm} \to K^{\pm}K_S^0$ events would shift the $D$ mass in the negative $M_{D_s}$ direction, well below the 1.8 GeV/$c^2$ cut off point. This is supported to some extent by the absence of any peaks at the $D_s$ mass in $M_{D_s}$ for the $D_s^{\pm} \to \pi^{\pm}\pi^0$ and $D_s^{\pm} \to \pi^{\pm}K_S^0$ modes in the generic $c\bar{c}$ sample (figures 3.19(a) and 3.20(c)).

A further source of peaking background is the decay of $D_s$ mesons that are produced directly from $c\bar{c}$ fragmentation and not from the decay of a $D_s^*$ meson. When reconstructed, these $D_s$ candidates peak in $M_{D_s}$ and form a smooth distribution in $\Delta M$ making them indistinguishable from SCF. No effort is made to extract the number of genuine SCF (those decays that involve a $D_s^*$) from this fake SCF. Hence, decays of this type will not contribute to the signal yield in the likelihood fit but will contribute to the SCF component.

## 3.6 Optimisation of the Likelihood Analysis

The MC samples used to parameterise PDFs and the data samples that will be fitted are optimised for the likelihood analysis. To reduce systematic errors, throughout the analysis the cut values are chosen to be identical wherever possible for each reconstructed mode. A choice is made to optimise the cuts for the $D_s^\pm \to K^\pm \pi^0$ extended likelihood fit.

The approximately uncorrelated variables $x_p$ and $\mathcal{S}$ are chosen for optimisation of the samples because as they increase all major backgrounds decrease exponentially while signal is approximately smooth (figures 3.3 and 3.9). On this argument another variable to include in the optimisation would be the $D_s$ helicity angle, but it is not for the following reason: it is significantly anti-correlated ($\rho \simeq -0.6$) with $\mathcal{S}$, therefore the gain from including it is not expected to be great. Similarly, the other discriminating variables used in the analysis exhibit some correlation with each other and the varibles mentioned above. Ideally all variables would be included in the optimisation but on practical grounds this was avoided due to the significant increase in computing time that would result from performing such a task.

For the optimisation procedure, the cut value placed on $x_p$ is varied across the region 0.70 to 0.85 in steps of 0.03. The $\mathcal{S}$ cut is varied from 0.0 to 0.2 in steps of 0.04.

At each point in the $x_p$, $\mathcal{S}$ cut value plane (defined by the cut values above) the sub-sample of MC events which pass the cuts for each background is selected. Each PDF component remains unchanged but their free parameters are redetermined with a fit to the new subsamples. Although it would be straightforward, this is not performed for the signal and SCF PDFs because to a good approximation their underlying distributions do not undergo any significant change and no further information is obtained. The new set of PDFs is used to generate a set of 100 toy MC samples using the method explained in section 3.7 and the branching fractions listed in table 3.7.

An extended likelihood fit is performed to extract the number of signal events from each toy sample and the negative log likelihood value is stored. A second fit is

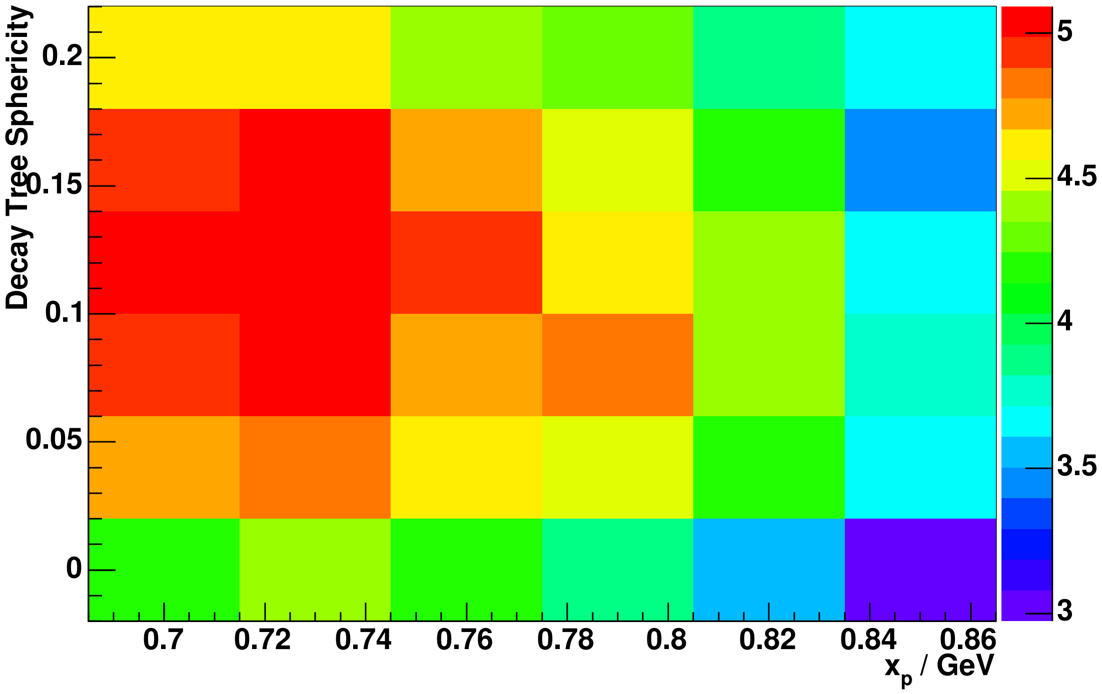


**Figure** 3.21: The statistical significance of a $D_s^{\pm} \to K^{\pm}\pi^0$ signal yield result for varying combinations of cuts in $x_p$ and $\mathcal{S}$. The significance at each point in the plane is a calculated average from 100 fits to a toy MC sample.

**Table** 3.7: Branching fractions used to calculate the number of events in the final data sample for the purpose of toy studies.

| Mode | Branching Fraction |
|---|---|
| $D_s^+ \to K^+\pi^0$ | $3.0 \times 10^{-4}$ |
| $D_s^+ \to \pi^+\pi^0$ | $3.0 \times 10^{-5}$ |
| $D_s^+ \to K^+K_S^0$ | $3.6 \times 10^{-2}$ |
| $D_s^+ \to \pi^+K_S^0$ | $3.6 \times 10^{-4}$ |

performed to the same sample with the number of signal events this time set constant and equal to zero, and once again the negative log likelihood value is stored. The quantity $\sqrt{|2\Delta(-\ln L)|}$ is subsequently calculated which represents the statistical significance of the fitted signal result. An average significance is extracted from a Gaussian fit to the distribution of the 100 values calculated from fits to the toy samples.

The routine described above is performed for each combination of $x_p$ and $\mathcal{S}$ cut

**Table** 3.8: Final efficiencies for all reconstructed modes with optimised cut values. Efficiencies are given for all MC samples. Errors on the signal efficiencies are $\mathcal{O}(0.03\%)$.

| Mode | Sample Specific Final Efficiencies / % | | | | | |
|---|---|---|---|---|---|---|
| | Signal | $q\overline{q}$ $(q = u, d, s)$ | $B^+B^-$ | $B^0\overline{B}^0$ | $c\overline{c}$ | $\tau^+\tau^-$ |
| $D_s^\pm \to K^\pm\pi^0$ | 4.62 | $5.12 \times 10^{-3}$ | $4.36 \times 10^{-4}$ | $1.65 \times 10^{-4}$ | $2.06 \times 10^{-3}$ | $9.81 \times 10^{-6}$ |
| $D_s^\pm \to \pi^\pm\pi^0$ | 5.54 | $1.38 \times 10^{-2}$ | $1.34 \times 10^{-3}$ | $8.58 \times 10^{-4}$ | $4.75 \times 10^{-3}$ | $1.94 \times 10^{-4}$ |
| $D_s^\pm \to K^\pm K_S^0$ | 3.86 | $4.46 \times 10^{-3}$ | $1.05 \times 10^{-4}$ | $8.02 \times 10^{-5}$ | $1.43 \times 10^{-2}$ | $2.88 \times 10^{-7}$ |
| $D_s^\pm \to \pi^\pm K_S^0$ | 4.67 | $5.63 \times 10^{-3}$ | $3.36 \times 10^{-4}$ | $3.36 \times 10^{-4}$ | $1.22 \times 10^{-2}$ | $5.19 \times 10^{-6}$ |

and the results are shown in figure 3.21. Evidently the cut on $x_p$ should not be too tight and is close to optimal already although some improvement can be gained through increasing its value. The background is falling off far quicker than the signal as a function of the $\mathcal{S}$ cut with the significance peaking at a value close to 0.1 and tailing off beyond that. The final cut values chosen for the analysis are $x_p > 0.73$ and $\mathcal{S} > 0.08$ which correspond to a statistical significance of $\sim 5.0$. The maximum significance of $\sim 5.1$ is found at $x_p > 0.70$ and $\mathcal{S} > 0.12$, however the important point is that the cut is placed in a region where the statistical significance is expected to be high. With this decision made, all PDF parameters for both signal and background components are re-fitted to the new optimised MC samples. The resultant overall efficiencies for each reconstruction mode are listed in table 3.8. The efficiencies for each individual cut for each mode are listed in tables 3.9, 3.10, 3.11 and 3.12. For each cut the denominator in the efficiency calculation is the number of events that have already passed both the skim and the refined event reconstruction for the relevant mode.

### 3.6.1 Extended Likelihood Fit

With all PDFs defined and parameterised, an extended likelihood fit is constructed from the list of components required by each reconstruction mode. In the case of $D_s^\pm \to K^\pm\pi^0$ there are four separate components: signal, SCF, $c\overline{c}$ background and smooth background. The extended fit yields a number of events that each component represents in the fitted dataset. For the remaining three modes the components are the same with the addition of a fifth, which represents the $D$ decay with the same final state as the $D_s$ decay in question.

**Table** 3.9: Final analysis cut values and their event selection efficiencies where the denominator is the number of events that have already passed the skim and the refined event reconstruction for the $D_s^\pm \to K^\pm K_S^0$ mode. Efficiencies are given for each MC sample.

| Cuts and Values | Sample Specific Cut Efficiencies / % | | | | | |
|---|---|---|---|---|---|---|
| | Signal | $q\overline{q}$ $(q = u, d, s)$ | $B^+B^-$ | $B^0\overline{B}^0$ | $c\overline{c}$ | $\tau^+\tau^-$ |
| $x_p > 0.73$ | 84.0 | 78.3 | 54.6 | 54.5 | 77.5 | 90.5 |
| $\lvert\cos\theta_H\rvert < 0.8$ | 89.5 | 68.6 | 89.1 | 91.4 | 81.6 | 36.1 |
| $\gamma\ E_{lab} > 0.05$ GeV | 98.0 | 93.1 | 96.5 | 95.2 | 95.6 | 80.4 |
| $\gamma\ E_{cms} > 0.1$ GeV | 85.1 | 66.1 | 73.7 | 69.9 | 75.2 | 47.1 |
| $\gamma$ not a $\pi^0$ | 96.5 | 91.7 | 90.3 | 90.9 | 90.9 | 96.2 |
| PID Likelihood | 76.2 | 21.6 | 14.2 | 10.6 | 19.7 | 1.75 |
| $1.8 < M(D_s) < 2.1$ GeV/$c^2$ | 98.3 | 75.1 | 74.1 | 74.2 | 76.8 | 57.9 |
| $0.1 < \Delta M < 0.2$ GeV/$c^2$ | 91.5 | 70.0 | 68.8 | 67.1 | 73.4 | 51.6 |
| $\mathcal{S} > 0.08$ | 77.7 | 48.1 | 90.6 | 92.8 | 70.8 | 23.9 |
| Good Fit Status | 99.8 | 99.8 | 99.3 | 99.2 | 99.7 | 99.5 |
| $\lvert M(K_S^0) - M(K_S^0)_{PDG}\rvert < 0.01$ GeV/$c^2$ | 96.1 | 61.9 | 52.9 | 58.7 | 65.0 | 41.4 |
| $K_S^0$ Flight Significance $> 3$ | 96.1 | 40.2 | 26.6 | 36.9 | 44.2 | 4.92 |
| Combination of Cuts | 31.3 | 0.639 | 0.372 | 0.337 | 1.72 | 0.00229 |

**Table** 3.10: Final analysis cut values and their event selection efficiencies where the denominator is the number of events that have already passed the skim and the refined event reconstruction for the $D_s^\pm \to \pi^\pm K_S^0$ mode. Efficiencies are given for each MC sample.

| Cuts and Values | Sample Specific Cut Efficiencies / % | | | | | |
|---|---|---|---|---|---|---|
| | Signal | $q\overline{q}$ $(q = u, d, s)$ | $B^+B^-$ | $B^0\overline{B}^0$ | $c\overline{c}$ | $\tau^+\tau^-$ |
| $x_p > 0.73$ | 83.6 | 77.8 | 54.2 | 54.0 | 77.8 | 72.0 |
| $\lvert\cos\theta_H\rvert < 0.8$ | 89.3 | 68.3 | 91.2 | 93.4 | 82.9 | 24.1 |
| $\gamma\ E_{lab} > 0.05$ GeV | 98.3 | 92.8 | 96.4 | 94.9 | 94.7 | 84.9 |
| $\gamma\ E_{cms} > 0.1$ GeV | 85.5 | 64.9 | 72.7 | 68.9 | 70.9 | 57.4 |
| $\gamma$ not a $\pi^0$ | 96.3 | 91.9 | 91.3 | 91.5 | 92.4 | 90.8 |
| PID Likelihood | 90.6 | 65.0 | 68.8 | 70.2 | 66.4 | 81.1 |
| $1.8 < M(D_s) < 2.1$ GeV/$c^2$ | 98.7 | 74.5 | 74.4 | 74.0 | 80.2 | 75.4 |
| $0.1 < \Delta M < 0.2$ GeV/$c^2$ | 91.7 | 69.4 | 68.0 | 66.7 | 72.6 | 51.1 |
| $\mathcal{S} > 0.08$ | 79.0 | 44.1 | 90.5 | 93.0 | 67.7 | 10.3 |
| Good Fit Status | 99.8 | 99.8 | 99.1 | 98.8 | 99.7 | 98.2 |
| $\lvert M(K_S^0) - M(K_S^0)_{PDG}\rvert < 0.01$ GeV/$c^2$ | 96.4 | 61.5 | 52.9 | 59.8 | 63.7 | 44.2 |
| $K_S^0$ Flight Significance $> 3$ | 96.9 | 39.4 | 27.3 | 38.4 | 41.8 | 14.1 |
| Combination of Cuts | 36.9 | 1.13 | 1.78 | 2.46 | 2.59 | 0.105 |

**Table** 3.11: Final analysis cut values and their event selection efficiencies where the denominator is the number of events that have already passed the skim and the refined event reconstruction for the $D_s^\pm \to K^\pm\pi^0$ mode. Efficiencies are given for each MC sample.

| Cuts and Values | Sample Specific Cut Efficiencies / % | | | | | |
|---|---|---|---|---|---|---|
| | Signal | $q\overline{q}$ $(q = u, d, s)$ | $B^+B^-$ | $B^0\overline{B}^0$ | $c\overline{c}$ | $\tau^+\tau^-$ |
| $x_p > 0.73$ | 83.5 | 76.2 | 63.8 | 65.3 | 69.4 | 74.7 |
| $\lvert\cos\theta_H\rvert < 0.8$ | 88.9 | 56.9 | 88.0 | 83.5 | 63.9 | 30.4 |
| $\gamma$ $E_{lab} > 0.05$ GeV | 97.8 | 91.9 | 95.5 | 95.3 | 95.8 | 84.8 |
| $\gamma$ $E_{cms} > 0.1$ GeV | 85.6 | 63.2 | 70.8 | 72.1 | 77.7 | 56.6 |
| $\gamma$ not a $\pi^0$ | 94.2 | 90.0 | 89.7 | 89.8 | 86.7 | 86.1 |
| PID Likelihood | 75.1 | 18.8 | 13.8 | 9.62 | 23.1 | 4.68 |
| $1.8 < M(D_s) < 2.1$ GeV/$c^2$ | 97.9 | 75.9 | 76.0 | 76.9 | 73.9 | 73.0 |
| $0.1 < \Delta M < 0.2$ GeV/$c^2$ | 92.7 | 70.1 | 74.3 | 76.0 | 71.2 | 58.1 |
| $\mathcal{S} > 0.08$ | 72.8 | 31.4 | 80.2 | 72.3 | 43.4 | 16.2 |
| Good Fit Status | 99.6 | 99.4 | 98.6 | 98.2 | 99.3 | 98.9 |
| Combination of Cuts | 28.6 | 0.488 | 1.28 | 0.699 | 0.802 | 0.0450 |

**Table** 3.12: Final analysis cut values and their event selection efficiencies where the denominator is the number of events that have already passed the skim and the refined event reconstruction for the $D_s^\pm \to \pi^\pm\pi^0$ mode. Efficiencies are given for each MC sample.

| Cuts and Values | Sample Specific Cut Efficiencies / % | | | | | |
|---|---|---|---|---|---|---|
| | Signal | $q\overline{q}$ $(q = u, d, s)$ | $B^+B^-$ | $B^0\overline{B}^0$ | $c\overline{c}$ | $\tau^+\tau^-$ |
| $x_p > 0.73$ | 83.2 | 75.3 | 63.5 | 65.7 | 68.0 | 70.6 |
| $\lvert\cos\theta_H\rvert < 0.8$ | 88.8 | 54.7 | 88.7 | 84.5 | 57.4 | 26.0 |
| $\gamma$ $E_{lab} > 0.05$ GeV | 97.9 | 91.9 | 95.3 | 95.3 | 95.6 | 85.5 |
| $\gamma$ $E_{cms} > 0.1$ GeV | 85.1 | 62.9 | 69.7 | 71.9 | 76.7 | 57.6 |
| $\gamma$ not a $\pi^0$ | 94.1 | 90.3 | 90.6 | 90.0 | 87.5 | 84.4 |
| PID Likelihood | 90.0 | 62.4 | 69.6 | 72.7 | 56.2 | 77.7 |
| $1.8 < M(D_s) < 2.1$ GeV/$c^2$ | 97.8 | 75.9 | 76.5 | 76.4 | 77.4 | 75.2 |
| $0.1 < \Delta M < 0.2$ GeV/$c^2$ | 92.4 | 69.6 | 74.5 | 76.0 | 70.4 | 57.2 |
| $\mathcal{S} > 0.08$ | 74.6 | 27.4 | 78.4 | 70.7 | 32.3 | 13.2 |
| Good Fit Status | 99.5 | 99.4 | 99.0 | 98.7 | 99.3 | 98.5 |
| Combination of Cuts | 33.7 | 1.92 | 4.80 | 4.91 | 2.92 | 1.05 |

## 3.7 Toy Studies

Using the PDFs defined previously in section 3.5, toy MC samples are generated and fitted in order to estimate the size and direction of any biases present in the likelihood technique. The expected number of events for each individual component in the fit is estimated using measured efficiencies (table 3.8) together with a set of approximate branching fractions which are listed in table 3.7. Expected event numbers are calculated using the following equation:

$$N = \sigma \times \mathcal{L}_{Int} \times \mathcal{B} \times \eta \tag{3.7}$$

where $\sigma$ is the $D_s$ production cross section, $\mathcal{L}_{Int}$ is the integrated luminosity, $\mathcal{B}$ is the branching fraction of the particular process (where applicable) and $\eta$ is the efficiency for selecting such events. A value of 210 fb$^{-1}$ is chosen for $\mathcal{L}_{Int}$.

For each of the four reconstructed modes the cross section is unknown and hence must be estimated to an order of magnitude accuracy in order for $N$ to represent a realistic expected number of signal events. The first step in doing this is to assume that all signal decays originate from $c\overline{c}$ fragmentation. During the fragmentation process the probability of a $s$ quark being produced and forming a bound state with a $c$ quark is estimated to be 0.1. It can be argued, through spin state counting, that of these $c\overline{s}$ states approximately 75% will be $D_s^*$ as opposed to $D_s$ mesons. The number of 0.75 is a first guess, while the value of 0.44 quoted in section 1.5 has been experimentally determined. Unfortunately, this number was not brought to the attention of the author until all toy studies had been completed. There is a factor of two increase in the expected number of $D_s^*$ mesons produced via $c\overline{c}$ fragmentation because either of the $c$ quarks can hadronise with a $s$ quark. Approximately 95% of these $D_s^*$ mesons will decay via the radiative process $D_s^{*\pm} \rightarrow D_s^{\pm}\gamma$. Therefore, to arrive at an approximate cross section for $D_s$ production via $D_s^*$ radiative decays, the $c\overline{c}$ cross section is multiplied by a factor of $\sim 0.14$. The factor is not required to be precise because it is the same for all four decay modes and hence its accuracy will not affect branching ratio measurements. The branching fraction for $K^0 \to K_S^0$ is not included here, but the branching fractions for $K_S^0 \to \pi^+\pi^-$ and $\pi^0 \to \gamma\gamma$ are taken into account in the efficiency, hence they are included in this approximation. Whether or not these processes are factored in is not important here because the numbers are not required to be exact. However, it is important that these experimentally determined values are included when calculating branching ratios with the results of the data fit.

A toy MC sample is generated for each component in the fit, containing the expected number of events smeared using Poisson statistics. The samples are added and together they represent a toy data sample. An extended likelihood fit is performed in the exact same manner as is performed on the real data, to extract the number of each component. This process is repeated 1000 times and a pull distribution is constructed for the signal yields, defined as

$$\text{Pull} = \frac{N_{fit} - N_{exp}}{\sigma_{N_{fit}}} \tag{3.8}$$

where $N_{fit}$ is the number extracted from the extended likelihood fit, $N_{exp}$ is the expected number of events before Poisson smearing and $\sigma_{N_{fit}}$ is the fit error on $N_{fit}$.

Fitting a Gaussian to the pull distributions for the signal yield identifies whether or not any fitting biases are present. For an unbiased analysis the mean and standard deviation of the pull are expected to be consistent with zero and one respectively. A shift in the mean indicates a preference to consistently select too many or too few signal events. A standard deviation less than or greater than one implies that the error on the fitted yield is being over- or under-estimated respectively.

Signal MC event statistics allow for the procedure to be repeated with the signal events sampled from the signal sample, instead of generated from the PDF. This provides an extra test of the signal PDF. However, this is not possible for $D_s^\pm \to K^\pm K_S^0$ where the expected number of events is larger than the number of signal MC events that survive the event selection.

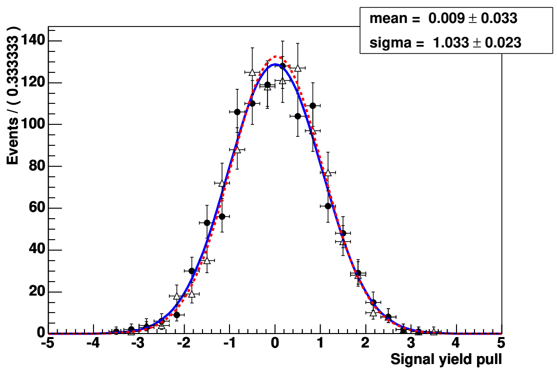


(a) $D_s^\pm \to K^\pm \pi^0$

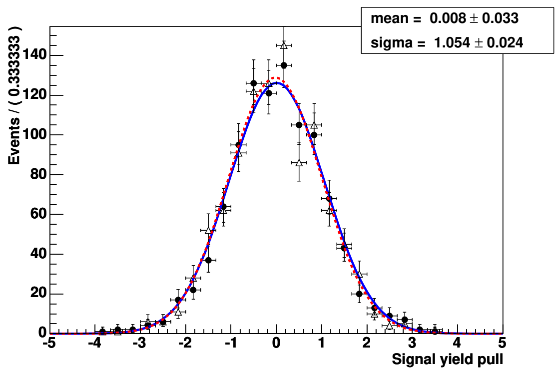


(b) $D_s^\pm \to \pi^\pm \pi^0$

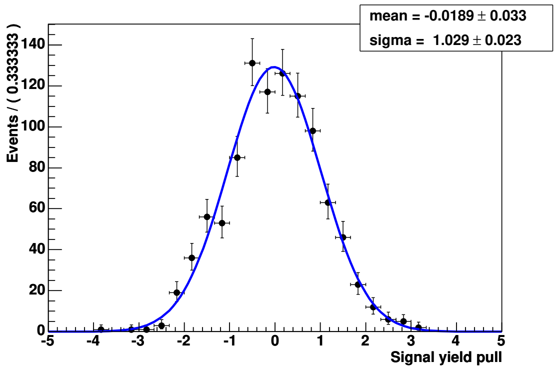


(c) $D_s^\pm \to K^\pm K_S^0$

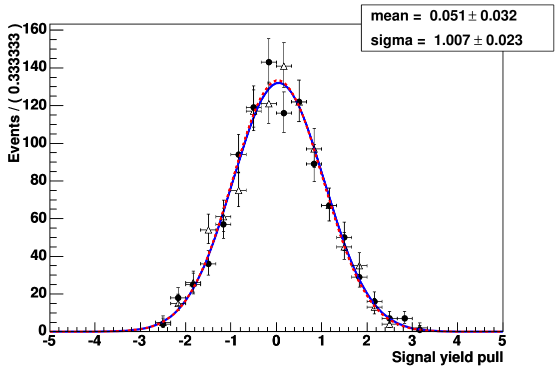


(d) $D_s^\pm \to \pi^\pm K_S^0$

**Figure** 3.22: Signal yield pulls from fits to 1000 toy MC samples for each reconstructed mode. The fit parameters indicate no significant biases are observed. Where relevant, the dashed red curve represents the result from toy fits where the signal events are sampled from the signal MC sample (triangular data points).

The results of the toy studies can be seen in figure 3.22. They indicate that no significant biases exist in the extended likelihood fit, when extracting the number of signal in the sample. Biases in the backgrounds are not considered because it does not matter if one background is preferred over another in the fit. Ultimately, the number of signal events is all that is required to be unbiased. An unbiased signal yield implies an unbiased total background yield, given that the total number of events selected is fixed.

# Chapter 4

# Results

## 4.1 Overview

The goal here is to calculate branching ratios and branching fractions for the three signal modes. Therefore this chapter describes all that is necessary to accomplish this task, including detailed descriptions of the statistical and systematic uncertainties present in the analysis.

The chapter begins by presenting the results of the fit to data for the $D_s^\pm \to K^\pm K_S^0$ reference mode. A subsequent toy study serves as a final check of the likelihood fit and an estimate of $\mathcal{B}(D_s^+ \to K^+\overline{K}^0)$ is evaluated for comparison with existing experimental data. A description follows of how aspects of the $D_s^\pm \to K^\pm K_S^0$ fit result feeds in to the signal mode fits to data. Fit results for the three signal modes are presented next. As with the reference mode, a final set of toy studies is performed for the signal modes following the fits to data.

Following the fit results, the sources of systematic uncertainty are discussed including how they are evaluated and how they affect the calculated results. Yields for the signal modes are then quoted with the systematic errors included. At this point a method is described for determining a 90% confidence level upper limit on signal yields that are consistent with zero.

Finally, all the numbers required in the branching ratio/fraction calculations are brought together and the final analysis results are evaluated and presented. In addition, an attempt is made to measure the charge asymmetry for decay modes where a statistically significant signal yield was observed. However, the asymmetry is not expected to be significant according to theoretical predictions.

## 4.2 Reference Mode

### 4.2.1 $D_s^{\pm} \to K^{\pm} K_S^0$ Fit To Data

When analysing the $D_s^{\pm} \to K^{\pm} K_S^0$ data sample a total of five event sample yields are extracted by the extended likelihood fit, the most important of which is the number of signal events, $N(D_s^{\pm} \to K^{\pm} K_S^0)$. There are a total of fifteen free parameters in the fit, each of which is listed in table 4.1 along with their fitted values and associated symmetric errors.

A signal event yield of

$$N(D_s^{\pm} \to K^{\pm} K_S^0) = 14281 \pm 168 \tag{4.1}$$

is extracted from the fit whose result is shown graphically in figure 4.1. A significant $D^{\pm} \to K^{\pm} K_S^0$ peak can also be seen centred around $\sim 1.87$ GeV/$c^2$ in the $M_{D_s}$ projection. There is an explicit background PDF contribution for this component and the fit returns a number of $D^{\pm} \to K^{\pm} K_S^0$ events, $N(D^{\pm} \to K^{\pm} K_S^0) = 4554 \pm 95$. The fitted number of SCF is significantly larger than the expected number implied from the fits to signal MC data. The SCF as a percentage of the sum of signal and SCF is $\sim 18\%$ from fits to signal MC samples compared with $\sim 43\%$ from the fit to data, where the number of SCF events, $N_{SCF}(D_s^{\pm} \to K^{\pm} K_S^0) = 10789 \pm 178$. The increase can be accredited to reconstructed $D_s^{\pm} \to K^{\pm} K_S^0$ events where the $D_s$ did not originate from a $D_s^*$ parent (section 3.5.6).

**Table** 4.1: Values returned by the minimisation routine for the floating parameters in the $D_s^{\pm} \to K^{\pm}K_S^0$ fit to data. The smooth background (Smooth bkg.) comprises $q\overline{q}$ ($q = u, d, s$), $B^+B^-$, $B^0\overline{B}^0$ and $\tau^+\tau^-$ events, and coefficients 1 and 2 represent the linear and quadratic coefficients of the relevant polynomial respectively.

| Fit Parameter | Value |
|---|---|
| Yields | |
| $N(D_s^{\pm} \to K^{\pm}K_S^0)$ | $(1.428 \pm 0.017) \times 10^4$ |
| $N_{SCF}(D_s^{\pm} \to K^{\pm}K_S^0)$ | $(1.079 \pm 0.018) \times 10^4$ |
| $N(D^{\pm} \to K^{\pm}K_S^0)$ | $(4.554 \pm 0.095) \times 10^3$ |
| $N(c\overline{c})$ | $(6.420 \pm 0.646) \times 10^3$ |
| $N$(Smooth bkg.) | $(1.356 \pm 0.065) \times 10^4$ |
| Shape Parameters | |
| $D_s^{\pm} \to K^{\pm}K_S^0$ $M_{D_s}$ mean | $1.9688 \pm 0.0001$ |
| $D_s^{\pm} \to K^{\pm}K_S^0$ $M_{D_s}$ width | $(7.134 \pm 0.065) \times 10^{-3}$ |
| $D_s^{\pm} \to K^{\pm}K_S^0$ $\Delta M$ mean | $(1.455 \pm 0.001) \times 10^{-1}$ |
| $D_s^{\pm} \to K^{\pm}K_S^0$ $\Delta M$ width | $(5.447 \pm 0.073) \times 10^{-3}$ |
| $D^{\pm} \to K^{\pm}K_S^0$ $M_{D_s}$ mean | $1.8703 \pm 0.0002$ |
| $D^{\pm} \to K^{\pm}K_S^0$ $M_{D_s}$ width | $(6.800 \pm 0.143) \times 10^{-3}$ |
| Smooth bkg. $M_{D_s}$ coeff. 1 | $(-7.113 \pm 0.189) \times 10^{-1}$ |
| Smooth bkg. $M_{D_s}$ coeff. 2 | $(1.533 \pm 0.068) \times 10^{-1}$ |
| Smooth bkg. $\Delta M$ coeff. 1 | $-4.579 \pm 0.259$ |
| Smooth bkg. $\Delta M$ coeff. 2 | $7.559 \pm 1.074$ |

The relatively large branching fraction of the reference mode allows the means and widths of the signal peak to be floated in the fit for both $M_{D_s}$ and $\Delta M$. The changes in these parameters compared to the numbers extracted from fits to signal MC data are calculated:

$$\begin{aligned}
\text{Absolute shift in } M_{D_s} \text{ mean} &= (-1.20 \pm 0.10) \times 10^{-3} \\
\text{Absolute shift in } \Delta M \text{ mean} &= (1.16 \pm 0.11) \times 10^{-3} \\
\text{Fractional change in } M_{D_s} \text{ width} &= 1.04 \pm 0.01 \\
\text{Fractional change in } \Delta M \text{ width} &= 0.92 \pm 0.02
\end{aligned}$$

Essentially the observed changes are a measure of how well the *BABAR* detector components are calibrated. For example, the shift in the $\Delta M$ peak mean value is largely due to the fact that the photon energy scale is not perfectly calibrated at *BABAR*. These observed changes are used to correct the signal PDFs for the three signal modes.

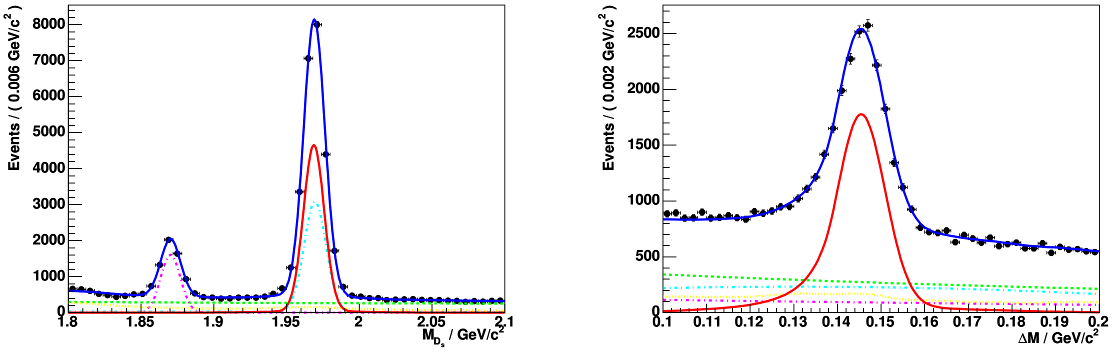


(a) (b)

**Figure** 4.1: Projections of $M_{D_s}$ and $\Delta M$ for the $D_s^\pm \to K^\pm K_S^0$ data fit. The solid red line represents the signal component, the dot-dashed cyan line represents SCF events, the dashed green line represents the smooth background, the dotted yellow line represents the $c\bar{c}$ background and the dot-dashed magenta line represents $D^\pm \to K^\pm K_S^0$ events.

The means of the signal mode peaks are shifted by the absolute observed change (in the same direction). The widths (standard deviations) are increased or decreased by the observed percentage change in the $D_s^\pm \to K^\pm K_S^0$ fit to data. All changes are applied to all three signal modes with the exception of the $M_{D_s}$ width change which is only applied to the $D_s^\pm \to \pi^\pm K_S^0$ fit. Because the modes containing a $\pi^0$ in the final state have a broader resolution in $M_{D_s}$ (when compared with modes reconstructed exclusively from charged tracks) it is not deemed appropriate to apply this shift. The systematic error associated with these actions is detailed in section 4.5.3.

### 4.2.2 Additional Toy Studies

The results from the fit to data are used to perform a secondary toy study which serves two purposes. Firstly, it checks again whether there are any biases in the selection of signal over background, when using the yields extracted from the data fit. Secondly, the likelihood value from the data fit can be compared with the mean likelihood value from the set of toy fits for consistency. This is the final check before the three signal data samples are analysed.

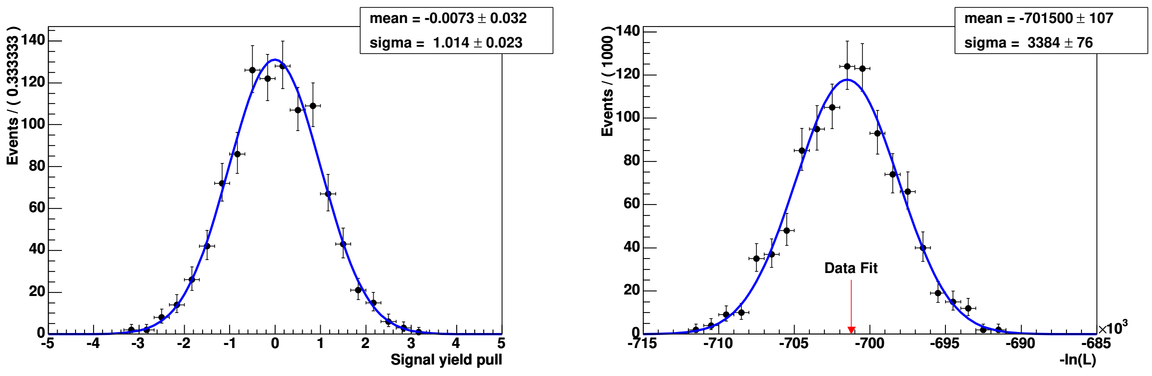


(a) (b)

**Figure** 4.2: Toy study results for $D_s^\pm \to K^\pm K_S^0$ using yields extracted from the data fit. The signal pull is found to be unbiased (a). The right hand plot shows a fit to the distribution of $-\ln L$ from the toy fits for the purposes of comparison with the data fit result, the value of which is indicated by the red arrow.

The signal yield is again found to be unbiased from toy studies and the pull is well described by a Gaussian PDF (figure 4.2(a)). The negative log likelihood value from the $D_s^\pm \to K^\pm K_S^0$ fit to data is $-\ln L = -701188$, which is consistent with the mean value from the toy studies of $-701500 \pm 3384$. The results indicate that the fit is well behaved.

### 4.2.3 $\mathcal{B}(D_s^+ \to K^+\overline{K}^0)$ Cross Check

It is possible to calculate a rough estimate of $\mathcal{B}(D_s^+ \to K^+\overline{K}^0)$ using some sensible estimates for the unknown quantities. Although the result is not accurate, a rough calculation does provide some form of sanity check for the analysis if the value can be shown to be of the correct order of magnitude when compared with the value in equation 1.30. Such an estimate can be calculated using the following equation:

$$\mathcal{B}(D_s^+ \to K^+\overline{K}^0) \simeq \frac{2 \times N(D_s^\pm \to K^\pm K_S^0)}{\epsilon(D_s^\pm \to K^\pm K_S^0) \times \mathcal{L}_{Int} \times \sigma_{c\overline{c}} \times 2 \times f_{s\overline{s}} \times P_V} \tag{4.2}$$

where $\mathcal{L}_{Int}$ is the integrated luminosity, $\sigma_{c\overline{c}}$ is the $c\overline{c}$ cross section at the $\Upsilon(4S)$ mass, $f_{s\overline{s}}$ is the fraction representing the probability of a strange quark produced during $c\overline{c}$

fragmentation forming a bound state with a $c$ quark, and $P_V$ is the production rate of $D_s^*$ compared to $D_s$ mesons. The efficiency with which the full decay chain $D_s^{*\pm} \rightarrow D_s^{\pm}\gamma$ followed by $D_s^{\pm} \rightarrow K^{\pm}K_S^0$ and $K_S^0 \rightarrow \pi^+\pi^-$ is reconstructed is represented by $\epsilon(D_s^{\pm} \rightarrow K^{\pm}K_S^0)$. A factor of two is required in the numerator to account for the ignored $K_L^0$ component of the $K^0$, and another factor of two is required in the denominator to account for the fact that a $c$ and a $\overline{c}$ quark are produced during fragmentation and either could hadronise with an $\overline{s}$ or $s$ quark respectively.

Taking $\mathcal{L}_{Int} = 229$ fb$^{-1}$, $\sigma_{c\overline{c}} = 1.3$ nb, $f_{s\overline{s}} = 0.1$ and $P_V = 0.44$, yields a value for the $D_s^+ \rightarrow K^+\overline{K}^0$ branching fraction (ignoring errors) of

$$\mathcal{B}(D_s^+ \rightarrow K^+\overline{K}^0) \simeq 3\%. \tag{4.3}$$

There is significant uncertainty associated with both the value of $f_{s\overline{s}}$ and the unknown $D_s^*$ spectrum (the latter affects the efficiency). Moreover, the value of $P_V$ used here could be very different in the regime satisfying $x_p > 0.73$. Given the apparent lack of knowledge, the estimate is not too far away from the nominal $\sim 4\%$ value, i.e. it is the correct order of magnitude. However, it is nothing more than an indication that the analysis is returning sensible results.

## 4.3 Signal Modes

The results given by the $D_s^{\pm} \rightarrow K^{\pm}K_S^0$ fit have shown the extended likelihood fit to be performing well. Fits to the three remaining signal modes, whose branching fractions are unknown, are performed in exactly the same manner with the major difference being there are fewer floating parameters.

In the fit to data each signal mode has its signal PDF parameters fixed. However, as described above, differences in the means and standard deviations of the signal peaks between the result of the $D_s^{\pm} \rightarrow K^{\pm}K_S^0$ fit to data and the fit to the signal MC sample are observed (section 4.2.1) and this information is subsequently used to alter the means and standard deviations of the $M_{D_s}$ and $\Delta M$ peaks.

**Table** 4.2: Values returned by the minimisation routine for the floating parameters in the $D_s^\pm \to K^\pm\pi^0$ fit to data. The smooth background (Smooth bkg.) comprises $q\overline{q}$ ($q = u, d, s$), $B^+B^-$, $B^0\overline{B}^0$ and $\tau^+\tau^-$ events, and coefficients 1 and 2 represent the linear and quadratic coefficients of the relevant polynomial respectively.

| Fit Parameter | Value |
|---|---|
| Yields | |
| $N(D_s^\pm \to K^\pm\pi^0)$ | $(8.984 \pm 0.684) \times 10^2$ |
| $N_{SCF}(D_s^\pm \to K^\pm\pi^0)$ | $(7.497 \pm 1.607) \times 10^2$ |
| $N(c\overline{c})$ | $(5.027 \pm 0.791) \times 10^3$ |
| $N$(Smooth bkg.) | $(2.641 \pm 0.085) \times 10^4$ |
| Shape Parameters | |
| Smooth bkg. $M_{D_s}$ coeff. 1 | $(-6.971 \pm 0.059) \times 10^{-1}$ |
| Smooth bkg. $M_{D_s}$ coeff. 2 | $(1.274 \pm 0.024) \times 10^{-1}$ |
| Smooth bkg. $\Delta M$ coeff. 1 | $4.998 \pm 0.731$ |
| Smooth bkg. $\Delta M$ coeff. 2 | $(-2.049 \pm 0.258) \times 10^1$ |

### 4.3.1 $D_s^\pm \to K^\pm\pi^0$ Fit To Data

The equivalent of the $D^\pm \to K^\pm K_S^0$ channel in the $D_s^\pm \to K^\pm\pi^0$ fit would be $D^\pm \to K^\pm\pi^0$ but this is a DCS process. Hence for the $D_s^\pm \to K^\pm\pi^0$ fit there is no explicit component for the as yet unobserved $D^\pm \to K^\pm\pi^0$ channel. Therefore, there are a total of eight floating parameters in the fit: four shape parameters of the non-peaking backgrounds and four yields. Table 4.2 lists the parameters returned by the fit to data for the $D_s^\pm \to K^\pm\pi^0$ signal mode. The likelihood fit returns a signal yield of

$$N(D_s^\pm \to K^\pm\pi^0) = 898 \pm 68. \tag{4.4}$$

The projection of the fit result in $M_{D_s}$ and $\Delta M$ is shown in figure 4.3, where the solid red curve represents the signal component in each dimension. The SCF yield from the fit is 749 $\pm$ 161 which equates to an amount of SCF as a percentage of signal and SCF of $\sim 45\%$. This is significantly higher than the $\sim 15\%$ determined from fits to signal MC and, like the $D_s^\pm \to K^\pm K_S^0$ fit, the excess is attributed to the decays of $D_s$ mesons via the signal channel that do not originate from a $D_s^*$.

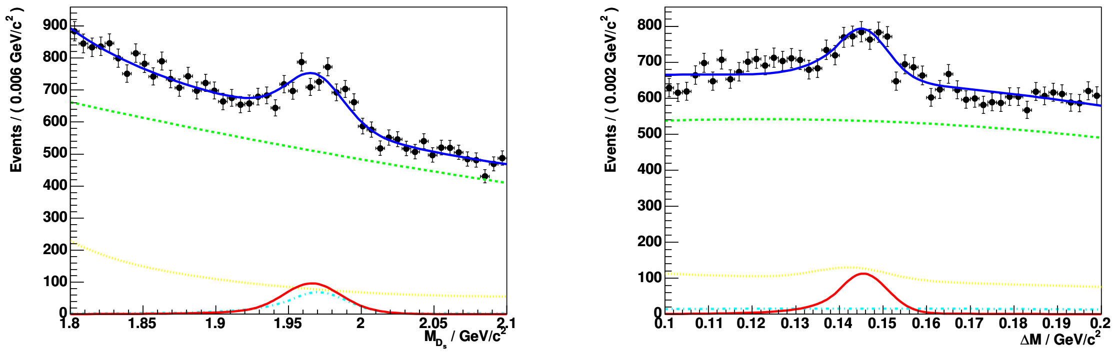


(a) (b)

**Figure** 4.3: Projections of $M_{D_s}$ and $\Delta M$ for the $D_s^\pm \to K^\pm\pi^0$ data fit. The solid red line represents the signal component, the dot-dashed cyan line represents SCF events, the dashed green line represents the smooth background and the dotted yellow line represents the $c\bar{c}$ background.

The final task of the likelihood fit is to determine the statistical significance of the observation. This is accomplished by setting the parameter $N(D_s^\pm \to K^\pm\pi^0)$ constant and equal to zero. The data is then refitted and the new likelihood value is compared with the value returned when $N(D_s^\pm \to K^\pm\pi^0)$ was allowed to float. The change in the likelihood, $\Delta(-\ln L)$, is calculated and the quantity $\sqrt{|2\Delta(-\ln L)|}$ represents the statistical significance in units of standard deviations. Performing these steps results in a significance of 13.8 for the first observation of the decay process $D_s^\pm \to K^\pm\pi^0$.

### 4.3.2 $D_s^\pm \to \pi^\pm\pi^0$ Fit To Data

There is a significant sideband contribution from the decay $D^+ \to \pi^+\pi^0$ in the $D_s^\pm \to \pi^\pm\pi^0$ fit to data. Therefore, there is an extra component in the extended likelihood fit compared to the $D_s^\pm \to K^\pm\pi^0$ fit making a total of nine floating parameters: four shape parameters for the smooth background and five component yields. The numerical results of the fit to data are listed in table 4.3. The parameters of the $D^+ \to \pi^+\pi^0$ PDF are fixed because the number of $D^+ \to \pi^+\pi^0$ events in the

**Table** 4.3: Values returned by the minimisation routine for the floating parameters in the $D_s^\pm \to \pi^\pm\pi^0$ fit to data. The smooth background (Smooth bkg.) comprises $q\overline{q}$ ($q = u, d, s$), $B^+B^-$, $B^0\overline{B}^0$ and $\tau^+\tau^-$ events, and coefficients 1 and 2 represent the linear and quadratic coefficients of the relevant polynomial respectively.

| Fit Parameter | Value |
|---|---|
| Yields | |
| $N(D_s^\pm \to \pi^\pm\pi^0)$ | $(-1.085 \pm 1.046) \times 10^2$ |
| $N_{SCF}(D_s^\pm \to \pi^\pm\pi^0)$ | $(7.182 \pm 3.405) \times 10^2$ |
| $N(D^+ \to \pi^+\pi^0)$ | $(2.184 \pm 0.272) \times 10^3$ |
| $N(c\overline{c})$ | $(6.816 \pm 1.983) \times 10^3$ |
| $N$(Smooth bkg.) | $(9.237 \pm 0.225) \times 10^4$ |
| Shape Parameters | |
| Smooth bkg. $M_{D_s}$ coeff. 1 | $(-2.243 \pm 0.378) \times 10^{-1}$ |
| Smooth bkg. $M_{D_s}$ coeff. 2 | $(-6.411 \pm 1.534) \times 10^{-2}$ |
| Smooth bkg. $\Delta M$ coeff. 1 | $2.646 \pm 1.369$ |
| Smooth bkg. $\Delta M$ coeff. 2 | $(-1.047 \pm 0.474) \times 10^1$ |

data is not large enough for the parameters to be reliably floated and the fit becomes unstable. The likelihood fit returns a $D_s^\pm \to \pi^\pm\pi^0$ signal yield of

$$N(D_s^\pm \to \pi^\pm\pi^0) = -108 \pm 105. \tag{4.5}$$

The signal yield is approximately one standard deviation away from, and hence consistent with, zero. Projections of the fit result in $M_{D_s}$ and $\Delta M$ are shown in figure 4.4, where the solid red line represents the signal component. The number of SCF in this instance is approximately two standard deviations away from zero $718 \pm 341$, which is not a significant result. Therefore this decay channel of the $D_s$ meson has not been observed in any form. Because no observation has been made there has been no attempt to determine $\sqrt{|2\Delta(-\ln L)|}$ by fitting with $N(D_s^\pm \to \pi^\pm\pi^0)$ set constant and equal to zero.

Table 4.3 indicates a significant number of $D^+ \to \pi^+\pi^0$ events are present in the data sample: $N(D^+ \to \pi^+\pi^0) = 2184 \pm 272$. This component is depicted by the dot-dashed magenta line in figure 4.4. The position of the dotted green line in the figure indicates that the vast majority of the data sample is non-peaking in both dimensions.

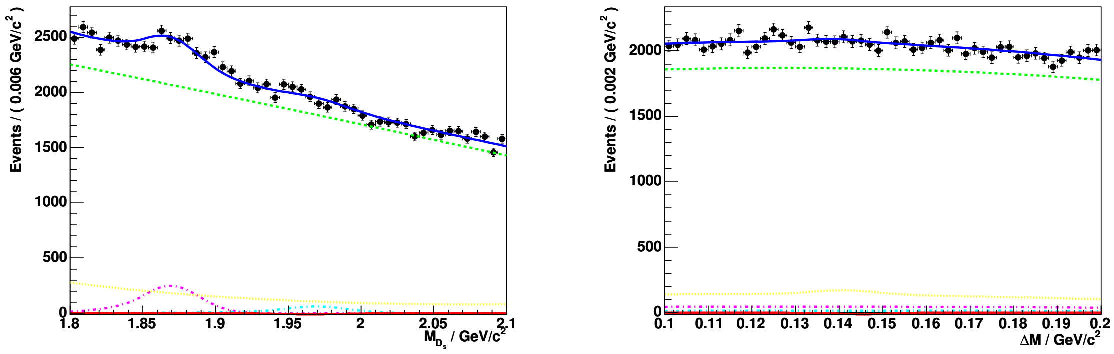


(a) (b)

**Figure** 4.4: Projections of $M_{D_s}$ and $\Delta M$ for the $D_s^\pm \to \pi^\pm\pi^0$ data fit. The solid red line represents the signal component, the dot-dashed cyan line represents SCF events, the dashed green line represents the smooth background, the dotted yellow line represents the $c\bar{c}$ background and the dot-dashed magenta line represents $D^+ \to \pi^+\pi^0$ events. The signal yield is consistent with zero.

### 4.3.3 $D_s^\pm \to \pi^\pm K_S^0$ Fit To Data

The branching fraction for $D^\pm \to \pi^\pm K_S^0$ is sufficiently large that the mean and standard deviation in the $M_{D_s}$ variable can be well determined from the fit to data and so these parameters are floated in the fit. When combined with the four shape parameters of the smooth background and five yields, they result in a total of 11 floating parameters. Table 4.4 lists the final parameter results of the likelihood fit and their associated errors. The $D_s^\pm \to \pi^\pm K_S^0$ signal yield from the fit is

$$N(D_s^\pm \to \pi^\pm K_S^0) = 1436 \pm 64. \tag{4.6}$$

The result is inconsistent with zero signal events and projections of the fit result in $M_{D_s}$ and $\Delta M$ are shown in figure 4.5, where the solid red line represents the signal component. The SCF yield of $1225 \pm 103$ equates to an amount of SCF as a percentage of signal and SCF of $\sim 46\%$. Like the $D_s^\pm \to K^\pm K_S^0$ fit, this value is larger than the expected $\sim 15\%$. These events are again accredited to those signal decays where the $D_s$ meson does not originate from a $D_s^*$ decay. The number of

**Table** 4.4: Values returned by the minimisation routine for the floating parameters in the $D_s^{\pm} \to \pi^{\pm} K_S^0$ fit to data. The smooth background (Smooth bkg.) comprises $q\overline{q}$ ($q = u, d, s$), $B^+B^-$, $B^0\overline{B}^0$ and $\tau^+\tau^-$ events, and coefficients 1 and 2 represent the linear and quadratic coefficients of the relevant polynomial respectively.

| Fit Parameter | Value |
|---|---|
| Yields | |
| $N(D_s^{\pm} \to \pi^{\pm} K_S^0)$ | $(1.436 \pm 0.064) \times 10^3$ |
| $N_{SCF}(D_s^{\pm} \to \pi^{\pm} K_S^0)$ | $(1.225 \pm 0.103) \times 10^3$ |
| $N(D^{\pm} \to \pi^{\pm} K_S^0)$ | $(2.719 \pm 0.021) \times 10^4$ |
| $N(c\overline{c})$ | $(7.416 \pm 0.701) \times 10^3$ |
| $N$(Smooth bkg.) | $(3.264 \pm 0.066) \times 10^4$ |
| Shape Parameters | |
| $D^{\pm} \to \pi^{\pm} K_S^0$ $M_{D_s}$ mean | $1.8701 \pm 0.0001$ |
| $D^{\pm} \to \pi^{\pm} K_S^0$ $M_{D_s}$ width | $(7.751 \pm 0.057) \times 10^{-3}$ |
| Smooth bkg. $M_{D_s}$ coeff. 1 | $(-8.584 \pm 0.020) \times 10^{-1}$ |
| Smooth bkg. $M_{D_s}$ coeff. 2 | $(1.919 \pm 0.008) \times 10^{-1}$ |
| Smooth bkg. $\Delta M$ coeff. 1 | $-5.926 \pm 0.154$ |
| Smooth bkg. $\Delta M$ coeff. 2 | $(1.344 \pm 0.063) \times 10^1$ |

$D^{\pm} \to \pi^{\pm} K_S^0$ events in the data is large, $N(D^{\pm} \to \pi^{\pm} K_S^0) = 27186 \pm 209$, and they are represented by the dot-dashed magenta line in figure 4.5.

As in the case of the $D_s^{\pm} \to K^{\pm}\pi^0$ fit to data, a significant signal has been observed

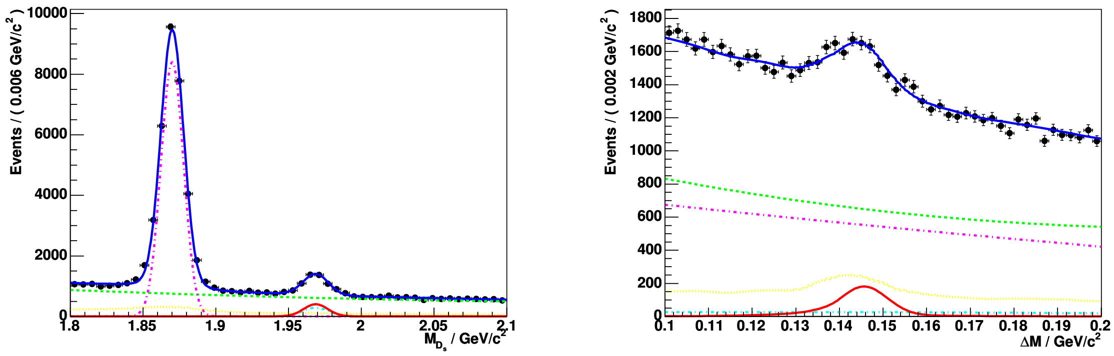


(a) (b)

**Figure** 4.5: Projections of $M_{D_s}$ and $\Delta M$ for the $D_s^{\pm} \to \pi^{\pm} K_S^0$ data fit. The solid red line represents the signal component, the dot-dashed cyan line represents SCF events, the dashed green line represents the smooth background, the dotted yellow line represents the $c\overline{c}$ background and the dot-dashed magenta line represents $D^{\pm} \to \pi^{\pm} K_S^0$ events.

**Table** 4.5: Negative log likelihood values determined from toy studies and fits to data. For each specific signal mode the two values are consistent with one another which indicates the fits are behaving well.

| | Negative log likelihood value | |
|---|---|---|
| Signal Mode | from data fit | from toy studies |
| $D_s^\pm \to K^\pm\pi^0$ | $-427895$ | $-428174 \pm 2499$ |
| $D_s^\pm \to \pi^\pm\pi^0$ | $-1433080$ | $-1435632 \pm 4721$ |
| $D_s^\pm \to \pi^\pm K_S^0$ | $-988090$ | $-988867 \pm 3954$ |

for $D_s^\pm \to \pi^\pm K_S^0$. The statistical significance of this first observation is determined in the same manner as before. Setting the parameter $N(D_s^\pm \to \pi^\pm K_S^0)$ constant and equal to zero and refitting the data yields a value of $\sqrt{|2\Delta(-\ln L)|} = 26.2$. Again, this quantity is in units of standard deviations.

### 4.3.4 Additional Toy Studies

Once all signal decay channel yields have been extracted from the fits to data, a final set of toy studies are performed for these modes. The purpose is to check for the existence of any biases in the fits when the yields determined in the data fits are used as inputs to a toy study. The exact same method is used as the one described in section 4.2.2.

The results of these studies are illustrated in figure 4.6. Pull distributions for the signal yields of each decay mode are shown in the left hand plots. The dotted lines in these plots correspond to a fit to the triangular data points, which represent toy study results where signal events are not generated, but sampled from the relevant signal MC sample. All curves show the means and standard deviations of the pulls to be consistent with 0 and 1 respectively. This implies no bias is present and errors are not being over- or under-estimated. The distributions of negative log likelihoods for the toy studies are shown in the right hand plots. Table 4.5 lists the negative log likelihood values with their standard deviations from the toy studies, and the corresponding values from the fits to data for comparison. Values determined in the fits to data are consistent with those determined via toy studies.

It should be noted that it is not possible to generate a negative number of events, as is observed in the signal yield result of the $D_s^{\pm} \to \pi^{\pm}\pi^0$ fit to data. For this mode alone the number of generated signal events is chosen to be zero (with the usual Poisson fluctuation). This approximation is deemed appropriate because the result quoted in equation 4.5 is compatible with zero.

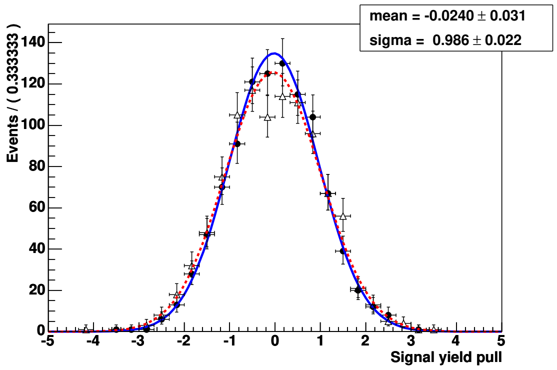


(a) $D_s^\pm \to K^\pm \pi^0$ toy signal pull.

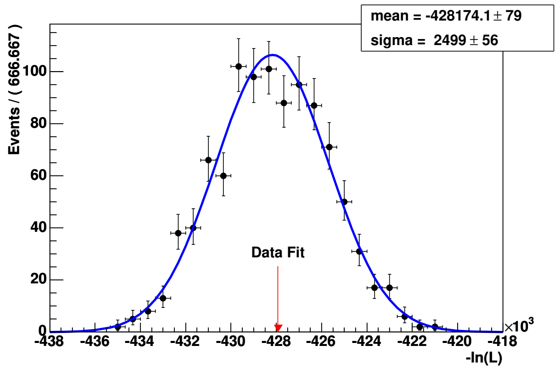


(b) $D_s^\pm \to K^\pm \pi^0$ toy negative log likelihood.

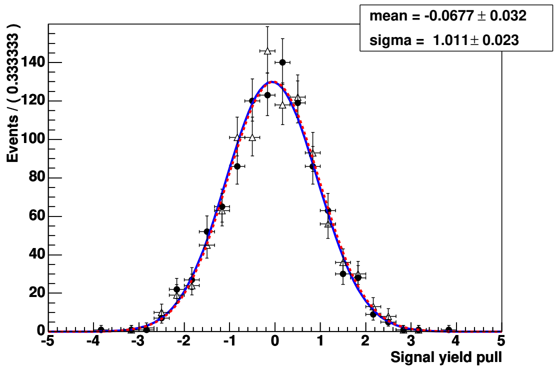


(c) $D_s^\pm \to \pi^\pm \pi^0$ toy signal pull.

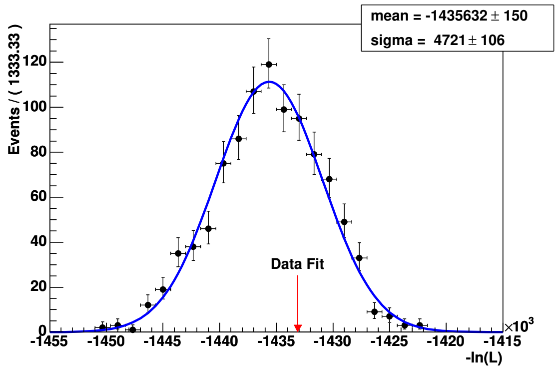


(d) $D_s^\pm \to \pi^\pm \pi^0$ toy negative log likelihood.

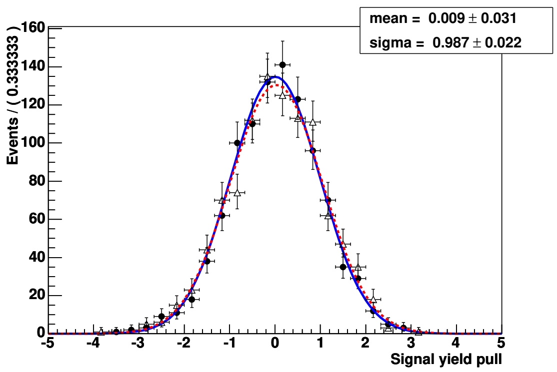


(e) $D_s^\pm \to \pi^\pm K_S^0$ toy signal pull.

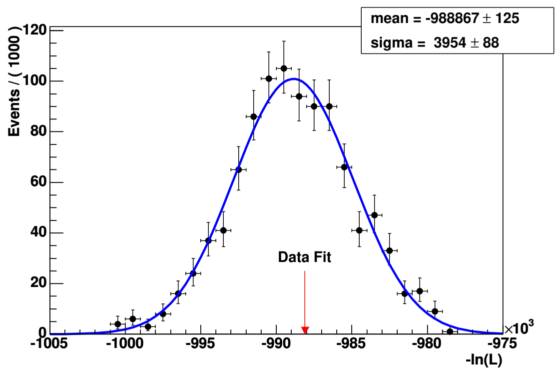


(f) $D_s^\pm \to \pi^\pm K_S^0$ toy negative log likelihood.

**Figure** 4.6: Toy study results for the $D_s^\pm \to K^\pm \pi^0$, $D_s^\pm \to \pi^\pm \pi^0$ and $D_s^\pm \to \pi^\pm K_S^0$ modes using the yields extracted from the fits to data. The signal pulls are found to be unbiased. The dashed red curves represent the results from toy fits where the signal events are sampled from the relevant signal MC sample (triangular data points). The right hand plots show fits to the distributions of $-\ln L$ from the toy fits, for the purposes of comparison with the data fit results (red arrows).

## 4.4 Systematic Uncertainties

Systematic errors are a significant source of uncertainty in the results of the analysis. They are split into three categories:

1. those that have a direct impact upon the signal yield from the fits,
2. those that introduce uncertainty in the branching ratio calculations, and
3. those that affect only the branching fraction calculation.

Numbers are quoted for errors that simply require the assignment of standard, predetermined values, while the methods of evaluation are outlined for those errors that require a direct data and MC sample comparison. All but one of the systematic errors fall into categories 1 and 2 listed above. The systematic error comprising category 3 is introduced via the uncertainty on $\mathcal{B}(D_s^+ \to K^+\overline{K}^0)$. After all systematic errors have been discussed, their values (where relevant) are listed in table 4.6.

## 4.5 Event Yield Systematic Errors

### 4.5.1 *BABAR* Mass and Energy Scale

There is uncertainty in the central values of $M_{D_s}$ and $\Delta M$ that is independent from the fit. Given the large statistics of the $D_s^\pm \to K^\pm K_S^0$ mode in the data, the choice was made to float these numbers in the fit to data for this mode. Subsequently, corrections to the central values for the three signal modes were made based on the differences observed between results from the fits to data and signal MC samples. The errors on these corrections, $\sigma_{\delta_{M_{D_s}}}$ and $\sigma_{\delta_{\Delta M}}$, represent the source of the systematic error and are due to the statistical error of the $D_s^\pm \to K^\pm K_S^0$ fit to data. The systematic is quantified by varying the mean of the $M_{D_s}$ $(\Delta M)$ signal PDF by

$\pm\sigma_{\delta_{M_{D_s}}}$ ($\pm\sigma_{\delta_{\Delta M}}$), observing the change in the signal yield and taking the maximum observed change as the systematic error.

Only the three signal modes are affected by this systematic. The percentage errors on the signal yield associated with the $M_{D_s}$ ($\Delta M$) peak are 0.1% (1.2%), 0.8% (0.4%) and 0.4% (1.1%) for the $D_s^{\pm} \to K^{\pm}\pi^0$, $D_s^{\pm} \to \pi^{\pm}\pi^0$ and $D_s^{\pm} \to \pi^{\pm}K_S^0$ modes respectively.

### 4.5.2 *BABAR* Mass and Energy Resolution

The $D_s$ and $\Delta M$ signal peak resolution differences between data and MC events are also determined from fits to data using the reference mode. Floating the parameter governing the standard deviation of the relevant peak in the $D_s^{\pm} \to K^{\pm}K_S^0$ data fit gives an estimate of disagreement between simulation and data regarding the resolution. The observed changes are applied to the data fits for the remaining three reconstruction modes, where applicable. The errors on these corrections are used to evaluate the associated systematic errors. Each corrected value is varied by $\pm 1\sigma$, where $\sigma$ represents the standard deviation of the measured correction, and the change in the signal yield is observed from a subsequent fit to the data. The largest change is taken as the systematic error.

The source of the $\Delta M$ difference is the radiative photon from the $D_s^*$ decay, implying the correction is the same for all modes. The measured $D_s$ resolution shift, however, is only applied to the $D_s^{\pm} \to \pi^{\pm}K_S^0$ mode since the resolution is much broader for modes involving a $\pi^0$. For the latter, a conservative estimate for the $\pi^0$ modes is to double the systematic associated with the $\Delta M$ resolution which is caused by the final state photon, since the reconstructed $D_s$ contains two photons in the $D_s^{\pm} \to K^{\pm}\pi^0$ and $D_s^{\pm} \to \pi^{\pm}\pi^0$ analyses.

As in the case of the *BABAR* mass and energy scale systematic error described in the previous section, the resolution systematic only affects the three signal modes. The percentage errors on the signal yield associated with the $M_{D_s}$ ($\Delta M$) resolution are

2.5% (1.2%), 1.0% (0.5%) and 0.4% (1.9%) for the $D_s^{\pm} \to K^{\pm}\pi^0$, $D_s^{\pm} \to \pi^{\pm}\pi^0$ and $D_s^{\pm} \to \pi^{\pm}K_S^0$ modes respectively.

### 4.5.3 MC Statistical Fit Effects

All fixed parameters in the final fit that are determined from fitting to MC events have associated errors, which arise due to the finite statistics of the MC samples used. In order to evaluate their systematic effects each parameter is varied by $\pm 1\sigma$ (where $\sigma$ is the error associated with the parameter) and the signal yield in the data is refitted. The largest deviation in signal yield from the two fits is taken to be the systematic error associated with that parameter. The systematic errors for each variable are added in quadrature to provide a combined error.

The above prescription assumes the error of each fixed PDF parameter to be uncorrelated with that of every other parameter, and is therefore only valid if this is true. However, it is well known that polynomial coefficients have a significant correlation factor, and in this analysis the two parameters common to each $2^{nd}$ order polynomial are found to be strongly anti-correlated. As a reasonable approximation, the correlation factor is taken to be $-1$ which results in an over-estimation of the systematic error but is far better than if they were treated as uncorrelated. In evaluating the systematic for polynomial parameters, the quadratic coefficient is shifted by $\mp 1\sigma$ when the linear coefficient of the corresponding polynomial is shifted by $\pm 1\sigma$.

The systematic errors, summed in quadrature over all fit parameters, as percentages of signal yield are evaluated as 2.8%, 18.1%, 2.5% and 1.3% for the $D_s^{\pm} \to K^{\pm}\pi^0$, $D_s^{\pm} \to \pi^{\pm}\pi^0$, $D_s^{\pm} \to \pi^{\pm}K_S^0$ and $D_s^{\pm} \to K^{\pm}K_S^0$ respectively.

Since it has no parameters, a separate method must be used to evaluate the systematic error associated with the non-parametric PDF. The sample used to construct the PDF is split into two sub-samples containing roughly equal numbers of events to make two new, separate PDFs. Each of the two new PDFs are then used in the data fit and the change in $N_{sig}$ is observed. These errors are combined to determine the systematic error for the non-parameteric PDF used in the real data fit. When the errors are combined a factor of $\frac{1}{\sqrt{2}}$ is used to account for the fact that each sub-sample has approximately half the number of events that were used to form the non-parametric PDF for the data fit. The non-parametric PDF only applies to decay modes with a $K_S^0$ in the final state and the systematic errors associated with them are found to be 0.4% and 0.1% for the $D_s^\pm \to \pi^\pm K_S^0$ and $D_s^\pm \to K^\pm K_S^0$ modes respectively.

### 4.5.4 Background Modelling

A systematic is introduced due to the background shapes differing in data and MC samples. To measure this difference, background data and MC samples are created for the modes $D_s^\pm \to K^\pm K_S^0$ and $D_s^\pm \to \pi^\pm \pi^0$. The effect of particle ID is considered negligible, allowing the observed difference for the $D_s^\pm \to K^\pm K_S^0$ samples to be applied to the $D_s^\pm \to \pi^\pm K_S^0$ mode. Similiarly, the observed difference for $D_s^\pm \to \pi^\pm \pi^0$ events can be applied to $D_s^\pm \to K^\pm \pi^0$ events.

Background data samples for the $D_s^\pm \to K^\pm K_S^0$ mode are identified by keeping events that do not contain a good $K_S^0$. The $K_S^0$ mass is required to not lie in the region 0.485 to 0.510 GeV/$c^2$. The lower and upper bounds on these sidebands are 0.473 GeV/$c^2$ and 0.523 GeV/$c^2$ respectively. Apart from this, all selections are identical to the optimised signal selections. For $D_s^\pm \to \pi^\pm \pi^0$ background an analogous method using the $\pi^0$ mass cannot be performed since the value has a reasonably tight cut prior to signal event reconstruction. Instead, the signal data sample is used since no signal is measured.

Histograms constructed for data and MC events can be seen in the upper plots of figures 4.7 and 4.8 for the $D_s^\pm \to K^\pm K_S^0$ and $D_s^\pm \to \pi^\pm \pi^0$ modes respectively. After this stage their integrals are set equal. Dividing the two and performing a likelihood fit on the result using a $1^{st}$ order polynomial, yields a measure of how much the two distributions disagree. These results, together with the linear fit (solid black line) are shown in the lower plots of figures 4.7 and 4.8 for the $D_s^\pm \to K^\pm K_S^0$ and

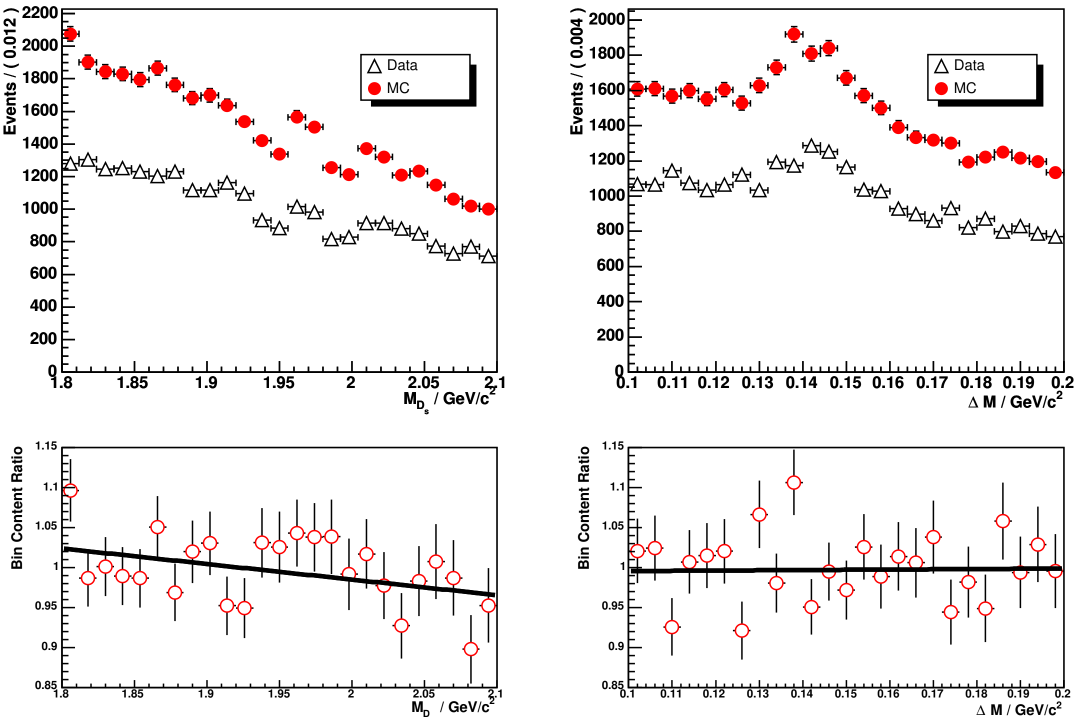


**Figure** 4.7: The plots represent background data and MC samples using $D_s^\pm \to K^\pm K_S^0$ samples. The upper plots in are histograms for evaluating the systematic error associated with background modelling of modes containing a $K_S^0$ candidate. The lower plots are the result of setting the histogram integrals equal and dividing the data by the MC sample. The solid black lines represent linear fits to the points in the plots.

$D_s^\pm \to \pi^\pm\pi^0$ modes respectively. This is performed for both $M_{D_s}$ and $\Delta M$ and a 2D PDF is constructed using the two gradients. Each background PDF that is not floated in the data fit is multiplied by the 2D PDF and the resultant change in the signal yield from the data fit is observed.

Multiplying each background individually by the correction and adding the sum of the signal yield changes in quadrature results in systematic errors of 0.07%, 1.94%, 0.10% and 0.02% for the $D_s^\pm \to K^\pm\pi^0$, $D_s^\pm \to \pi^\pm\pi^0$, $D_s^\pm \to \pi^\pm K_S^0$ and $D_s^\pm \to K^\pm K_S^0$ respectively. The values represent the percentage change in the signal yield.

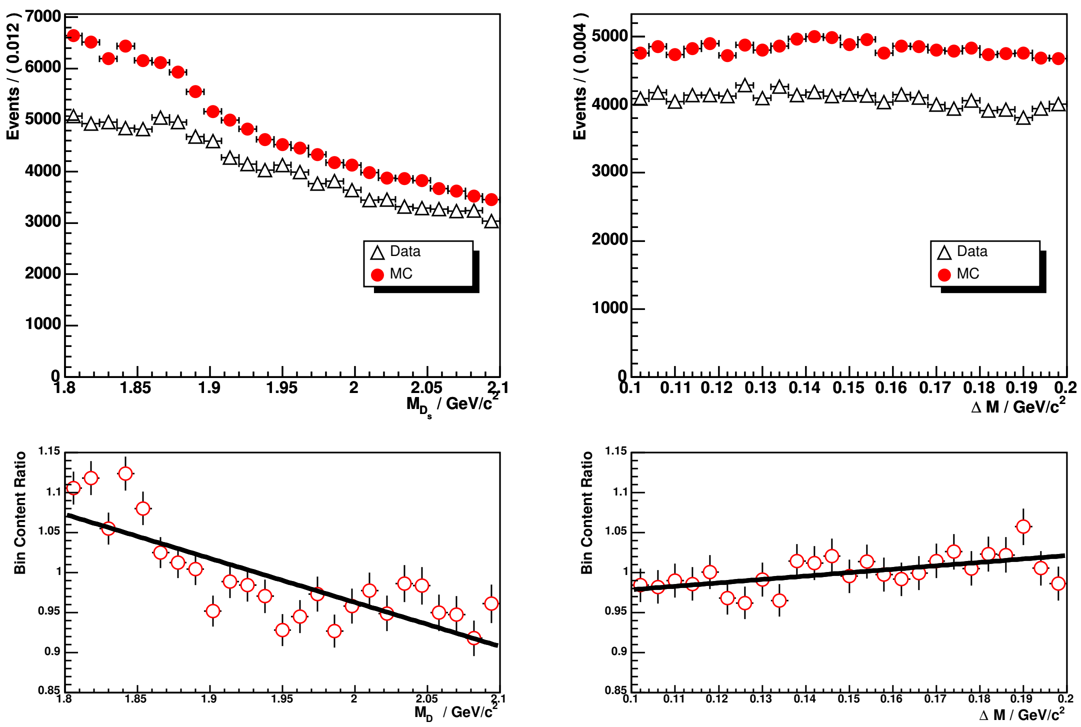


**Figure** 4.8: The plots represent background data and MC samples using $D_s^{\pm} \to \pi^{\pm}\pi^0$ samples. The upper plots in are histograms for evaluating the systematic error associated with background modelling of modes containing a $\pi^0$ candidate. The lower plots are the result of setting the histogram integrals equal and dividing the data by the MC sample. The solid black line represents a linear fit to the data points.

### 4.5.5 Fake Signal Peaks

In section 3.5.6 the modes containing a charged kaon in the final state were said to potentially suffer from a fake peak in $M_{D_s}$ at the nominal $D_s$ mass. It is a result of mis-identifying the pion from a $D$ decay as a kaon. Therefore, the decay $D^+ \to \pi^+\pi^0$ feeds into the $D_s^{\pm} \to K^{\pm}\pi^0$ signal yield and the decay $D^{\pm} \to \pi^{\pm}K_S^0$ feeds into the $D_s^{\pm} \to K^{\pm}K_S^0$ signal yield. However, the $D$ decays will only feed into the signal yield if the events peak in both $M_{D_s}$ and $\Delta M$. Therefore, the $D$ meson must originate from a $D^{*\pm} \to D^{\pm}\gamma$ decay. An estimate of the number of these fake signal decays is evaluated by considering a number of factors:

1. Ratio of $D^{*\pm}$ to $D_s^{*\pm}$ production at *BABAR*,

2. Ratio of $\mathcal{B}(D^{*\pm} \to D^{\pm}\gamma)$ to $\mathcal{B}(D_s^{*\pm} \to D_s^{\pm}\gamma)$,

3. Ratio of pion mis-identification rate to kaon selection efficiency, and

4. Branching fraction ratios $\mathcal{B}(D_s^+ \to K^+\overline{K}^0)/\mathcal{B}(D^+ \to \pi^+\overline{K}^0)$ and $\mathcal{B}(D_s^+ \to K^+\pi^0)/\mathcal{B}(D^+ \to \pi^+\pi^0)$.

The first ratio is evaluated by approximating the ratio of $d$ to $s$ quark production in $c\overline{c}$ fragmentation as 4:1. The second is simply calculated using the branching fractions of the Particle Data Group [17]:

$$\frac{\mathcal{B}(D^{*\pm} \to D^{\pm}\gamma)}{\mathcal{B}(D_s^{*\pm} \to D_s^{\pm}\gamma)} = (1.70 \pm 0.43) \times 10^{-2}. \tag{4.7}$$

From tables 3.9 and 3.11 the kaon selection efficiency can be taken as approximately $\sim 76\%$. The pion mis-identification rate is provided by measurements of the Particle Identification analysis tools group at *BABAR* [89]. Although the value is dependent on the track momentum, the value is taken at the high end of the range where the fake rate is around 5%.

Multiplying the first three ratios together yields a factor for genuine signal to fake peaking signal of $\sim 221 : 1$. This is applicable to both the $D_s^{\pm} \to K^{\pm}\pi^0$ and $D_s^{\pm} \to K^{\pm}K_S^0$ decay modes. The fourth ratio in the list differs for each decay mode. The value of $\mathcal{B}(D_s^+ \to K^+\overline{K}^0)$ (equation 1.30) is combined with $\mathcal{B}(D^+ \to \pi^+\overline{K}^0)$ [17] to give

$$\frac{\mathcal{B}(D_s^+ \to K^+\overline{K}^0)}{\mathcal{B}(D^+ \to \pi^+\overline{K}^0)} = 1.6 \pm 0.3. \tag{4.8}$$

There is no measurement for $\mathcal{B}(D_s^+ \to K^+\pi^0)$ and so an average of 0.153% is calculated from the theoretical predictions for this decay mode listed in table 1.2. Combining this with the following measurement [17]

$$\mathcal{B}(D^+ \to \pi^+\pi^0) = (1.33 \pm 0.22) \times 10^{-3} \tag{4.9}$$

gives a branching fraction ratio of

$$\frac{\mathcal{B}(D_s^+ \to K^+\pi^0)}{\mathcal{B}(D^+ \to \pi^+\pi^0)} = 1.15 \pm 0.19. \tag{4.10}$$

Neglecting the errors on the branching fraction ratios and assuming comparable efficiencies for the $D_s$ and $D$ decays yields genuine to fake signal event ratios of $354 : 1 (0.28\%)$ and $254 : 1 (0.39\%)$ for the $D_s^{\pm} \to K^{\pm}K_S^0$ and $D_s^{\pm} \to K^{\pm}\pi^0$ analyses respectively. These are conservatively taken to be uncertain by an amount equal to their value.

The percentage errors are applied as symmetric systematic errors on the signal yields.

## 4.6 Fit Yields

All the systematics listed in table 4.6 that affect the signal yields can now be combined and added to the systematic error resulting in final event yields for all four $D_s$ decay modes:

$$\begin{aligned} N(D_s^{\pm} \to K^{\pm}\pi^0) &= 898 \pm 68 \pm 37 \\ N(D_s^{\pm} \to \pi^{\pm}\pi^0) &= -108 \pm 105 \pm 20 \\ N(D_s^{\pm} \to K^{\pm}K_S^0) &= 14281 \pm 168 \pm 195 \\ N(D_s^{\pm} \to \pi^{\pm}K_S^0) &= 1436 \pm 64 \pm 49 \end{aligned}$$

where the first and second errors are statistical and systematic respectively in all cases. In the case of $D_s^{\pm} \to \pi^{\pm}\pi^0$ where the signal yield is negative, the percentage errors for the systematic errors affecting the signal yield quoted in table 4.6 are calculated with respect to the absolute value of the $D_s^\pm \to \pi^\pm\pi^0$ signal event yield. The numbers are tabulated as percentages rather than absolute event numbers for the purposes of combining the systematic errors affecting signal yields and branching ratios.

### 4.6.1 Yield Limit Calculation

The above result for the $D_s^\pm \to \pi^\pm\pi^0$ yield is consistent with zero. The sensitivity of the measurement is calculated by considering what the upper limit, with 90% confidence, on the yield would be if the result of the likelihood fit had been exactly zero. In this case, assuming Gaussian errors, the sensitivity, $S$, is calculated to be

$$S = 1.28\sqrt{105^2 + 20^2} = 137\,\text{events}. \tag{4.11}$$

A conservative method is developed with which to calculate an upper limit on the signal yield with 90% confidence. This is achieved by finding the upper allowed limit for $N(D_s^\pm \to \pi^\pm\pi^0)$ from the likelihood fit. This technique was not developed by the author and the recipe described in [90, 91] is followed here.

It is assumed that the signal event yield has Gaussian errors such that the likelihood, $\mathcal{L}$, of a value, $x$, is given by

$$\mathcal{L} = \mathcal{L}_{max} \exp\Big( - \frac{(x-\mu)^2}{2\sigma^2} \Big) \tag{4.12}$$

where $\sigma$ represents the statistical uncertainty associated with the likelihood fit and $\mathcal{L}_{max}$ is the maximum likelihood at which the most likely value of $x$ occurs. Here, $x$ represents the signal yield.

A scan of the likelihood curve is produced as a function of signal event yield. This can be seen in figure 4.9 (solid blue curve). The $y$-axis has units of $-2\ln(\mathcal{L}/\mathcal{L}_{max})$ which is usually termed the likelihood $\chi^2$ given by

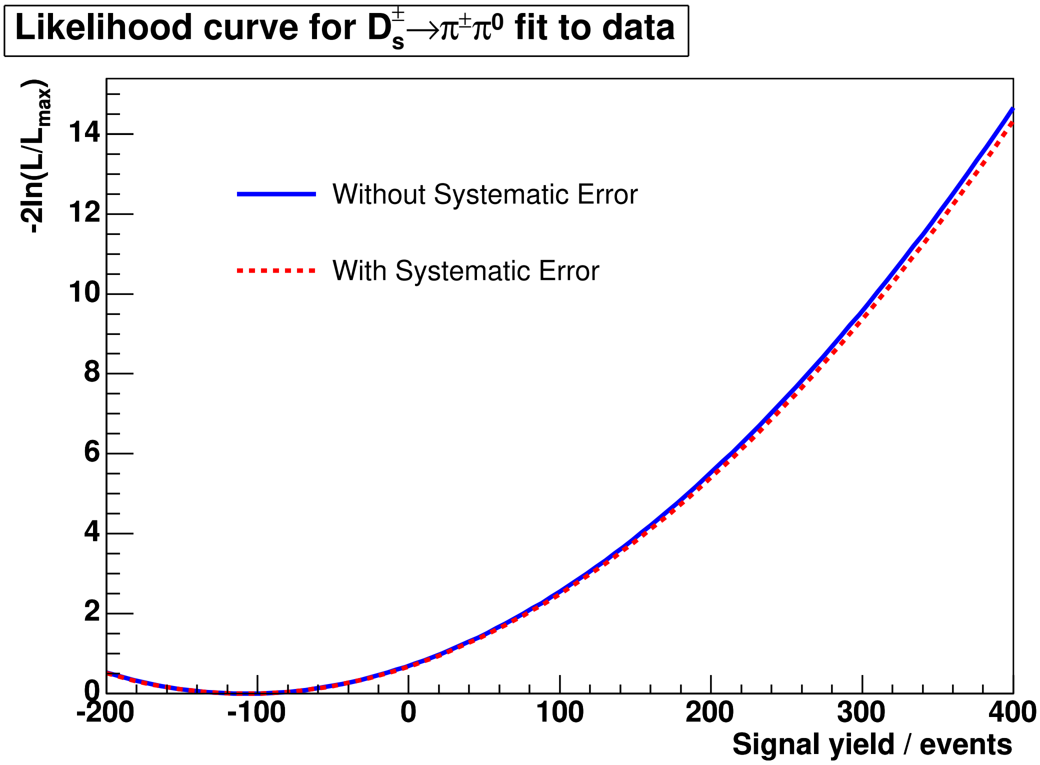


**Figure** 4.9: A scan of the likelihood curve is shown for the $D_s^{\pm} \to \pi^{\pm}\pi^0$ fit to data as a function of the signal event yield. The $y$-axis is in units of standard deviations. The solid (blue) curve represents the raw likelihood curve, while the dashed (red) curve represents the raw likelihood curve convoluted with a Gaussian function whose width is equal to the combined systematic error on the event yield (see text).

$$\begin{aligned} \chi^2 &= -2\ln\left(\frac{\mathcal{L}}{\mathcal{L}_{max}}\right) \\ &= \frac{(x-\mu)^2}{\sigma^2} \end{aligned} \tag{4.13}$$

To calculate the limit properly the combined systematic error on the event yield must be incorporated into the likelihood curve. A Gaussian function with a width equal to the systematic error on the event yield is convoluted with the likelihood parabola to achieve this. Essentially the new parabola is a Gaussian likelihood curve with $\sigma^2 = \sigma^2_{stat.} + \sigma^2_{syst.}$ where $\sigma^2_{stat.}$ is the original error from the likelihood fit. The $\chi^2$ then becomes

$$\chi^2 = \frac{\chi^2_{stat.}.\chi^2_{syst.}}{\chi^2_{stat.} + \chi^2_{syst.}} \tag{4.14}$$

where $\chi^2_{stat.} = (x-\mu)^2/\sigma^2_{stat.}$ and $\chi^2_{syst.} = (x-\mu)^2/\sigma^2_{syst.}$. This has the effect of broadening the original likelihood curve, the result of which is shown by the red dashed line in figure 4.9.

The new curve can now be used to calculate $\mathcal{L}(x)/\mathcal{L}_{max}$ which in turn can be integrated to give an upper limit with a desired confidence. By requiring the integral over all $x$ to be equal to 1, an upper limit with 90% confidence can be obtained by finding the value of $x$ that satisfies

$$\int_{-\infty}^{x} \frac{\mathcal{L}(x)}{\mathcal{L}_{max}} dx = 0.9 \tag{4.15}$$

Before this is performed, the upper limit can be rendered more conservative by taking a Bayesian approach and including a prior PDF, $\pi(x)$, which represents the prior knowledge that the value of $x$ should never be less than zero. A simple form is used in this case given by

$$\pi(x) = \begin{cases} 0 & ; x < 0 \\ 1 & ; x \geqslant 0 \end{cases} \tag{4.16}$$

which results in changing the lower limit on the integral in equation 4.15 from $-\infty$ to zero. A plot of the curve to be integrated is shown in figure 4.10. The red arrow in the plot indicates the value of $x$ that satisfies the integral. From this the upper limit on the signal yield is found to be

$$N(D_s^{\pm} \rightarrow \pi^{\pm}\pi^0) < 163 \qquad \mathrm{CL} = 90\%. \tag{4.17}$$

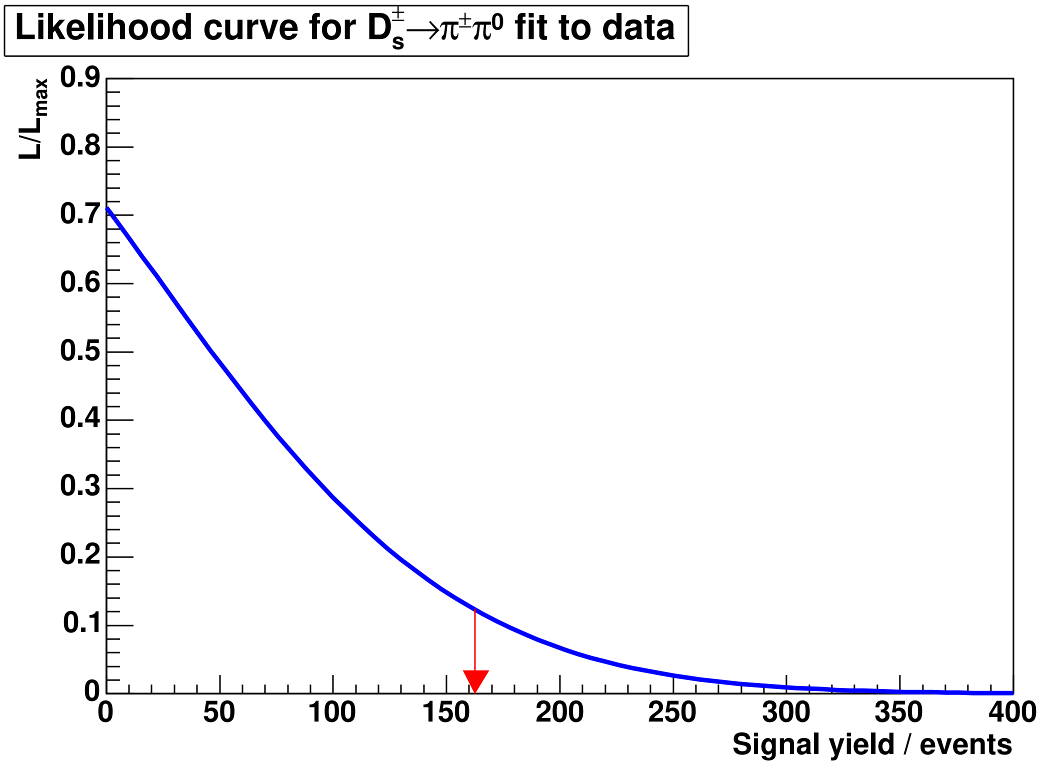


**Figure** 4.10: A curve representing $\mathcal{L}(x)/\mathcal{L}_{max}$ is shown for the $D_s^{\pm} \to \pi^{\pm}\pi^0$ fit to data as a function of the signal event yield. The 90% confidence upper limit on the signal yield is indicated by the red arrow.

## 4.7 Branching Ratio Systematic Errors

As stated at the beginning of the chapter, a principal goal of this analysis is to calculate the branching ratios of the three signal decay modes of the $D_s$ meson with respect to the reference mode. The following sections detail the systematic errors that are present in the analysis. The calculation of branching ratios, discussed later in detail, allows certain sytematics to be completely removed for certain decay modes. It is made explicit in the text which systematics affect which signal decay modes.

### 4.7.1 Signal MC Statistical Fit Effects

Efficiencies for the reconstructed modes are determined from signal MC samples. The finite statistics used here introduce a systematic error in the calculated efficiencies. All four mode efficiencies are comparable in size (table 3.8) and hence the systematic turns out to be the same for each mode: 0.03%.

### 4.7.2 Spectral Effects

At *BABAR* the $D_s^*$ mesons produced through $c\overline{c}$ fragmentation are not mono-energetic (unlike the case for $B$ mesons). It is therefore feasible that the $x_p$ spectrum generated by the simulation is not the same as that in the data. In addition, the selection efficiency may be a non-constant function of $x_p$. Absolute efficiencies are not important here since only efficiency ratios are required to calculate branching ratios with respect to the reference mode. Therefore, the systematic errors are evaluated on the ratios only.

In estimating the systematic error associated with these effects, it is assumed that some fraction, $f < 1$, of the error is due to an incorrect spectrum in the simulation and a fraction $1 - f$ is due to the $x_p$ dependence of the selection efficiency. The calculated efficiency ratios can be written as

$$R_{D_s^\pm \to X^\pm Y} = \frac{\epsilon_{D_s^\pm \to X^\pm Y}}{\epsilon_{D_s^\pm \to K^\pm K_S^0}} = \frac{\int \epsilon_{D_s^\pm \to X^\pm Y}(x_p) S_{Data}(x_p)\,\mathrm{d}x_p}{\int \epsilon_{D_s^\pm \to K^\pm K_S^0}(x_p) S_{Data}(x_p)\,\mathrm{d}x_p} \tag{4.18}$$

where $\epsilon$ is efficiency, $S$ is the spectrum and '$(x_p)$' indicates that the preceeding quantity is a function of $x_p$. Efficiency and spectral effects cannot be independently determined and so a choice is made to assume that the entire systematic is due to the spectral difference between the simulation and data. Performing the following argument for the efficiency separately would, in effect, result in double-counting of the systematic error. Letting $S_{Data}(x_p) = S_{MC}(x_p) + \delta S_{MC}(x_p)$ and approximating the change as a linear function of $x_p$ to first order gives $S_{Data}(x_p) = S_{MC}(x_p) \cdot (a + bx_p)$, where $a$ and $b$ are parameters to be determined. Equation 4.18 now implies

$$R'_{D_s^\pm \to X^\pm Y} = \frac{a \int \epsilon_{D_s^\pm \to X^\pm Y} S_{MC}\,\mathrm{d}x_p + b \int \epsilon_{D_s^\pm \to X^\pm Y} S_{MC} x_p\,\mathrm{d}x_p}{a \int \epsilon_{D_s^\pm \to K^\pm K_S^0} S_{MC}\,\mathrm{d}x_p + b \int \epsilon_{D_s^\pm \to K^\pm K_S^0} S_{MC} x_p\,\mathrm{d}x_p} \tag{4.19}$$

where $R'$ is the corrected efficiency ratio and it is assumed $\epsilon$ and $S$ are functions of $x_p$. Knowing the linear dependence on $x_p$ to be a small effect, the right hand term in the denominator is considered small compared to the left hand term. This fact allows a subsequent binomial expansion of the denominator giving

$$R'_{D_s^\pm \to X^\pm Y} = \left( a \int \epsilon_{D_s^\pm \to X^\pm Y} S_{MC} \, \mathrm{d}x_p + b \int \epsilon_{D_s^\pm \to X^\pm Y} S_{MC} x_p \, \mathrm{d}x_p \right) \times \left( \frac{1}{a \int \epsilon_{D_s^\pm \to K^\pm K_S^0} S_{MC} \, \mathrm{d}x_p} + \frac{b \int \epsilon_{D_s^\pm \to K^\pm K_S^0} S_{MC} x_p \, \mathrm{d}x_p}{(a \int \epsilon_{D_s^\pm \to K^\pm K_S^0} S_{MC} \, \mathrm{d}x_p)^2} \right) \tag{4.20}$$

and, retaining only leading order terms, after some algebra

$$\begin{aligned} R'_{D_s^\pm \to X^\pm Y} &= \frac{a \int \epsilon_{D_s^\pm \to X^\pm Y} S_{MC} \, \mathrm{d}x_p}{a \int \epsilon_{D_s^\pm \to K^\pm K_S^0} S_{MC} \, \mathrm{d}x_p} \cdot \left( 1 + \frac{b \int \epsilon_{D_s^\pm \to X^\pm Y} S_{MC} x_p \, \mathrm{d}x_p}{a \int \epsilon_{D_s^\pm \to X^\pm Y} S_{MC} \, \mathrm{d}x_p} \right. \\ &\qquad \left. - \frac{b \int \epsilon_{D_s^\pm \to K^\pm K_S^0} S_{MC} x_p \, \mathrm{d}x_p}{a \int \epsilon_{D_s^\pm \to K^\pm K_S^0} S_{MC} \, \mathrm{d}x_p} \right) \\ &= R_{D_s^\pm \to X^\pm Y} \cdot \left( 1 + \frac{b \int \epsilon_{D_s^\pm \to X^\pm Y} S_{MC} x_p \, \mathrm{d}x_p}{a \int \epsilon_{D_s^\pm \to X^\pm Y} S_{MC} \, \mathrm{d}x_p} \right. \\ &\qquad \left. - \frac{b \int \epsilon_{D_s^\pm \to K^\pm K_S^0} S_{MC} x_p \, \mathrm{d}x_p}{a \int \epsilon_{D_s^\pm \to K^\pm K_S^0} S_{MC} \, \mathrm{d}x_p} \right) \end{aligned} \tag{4.21}$$

implying that the efficiency ratio is modified by a correction factor, given here by the terms within the brackets.

Determining the correction factor, $f$, involves two stages. Firstly, the parameters $a$ and $b$ must be determined and secondly, the integrals must be evaluated. The former is achieved through a direct comparison of the $x_p$ spectra for $D_s^\pm \to K^\pm K_S^0$ signal MC and data events. A simple background subtraction is conducted on the data sample to acquire an approximately pure signal $D_s^\pm \to K^\pm K_S^0$ sample. The $x_p$ distributions for data and MC events are normalised by setting their integrals equal, and the data distribution is divided by the MC sample distribution to yield

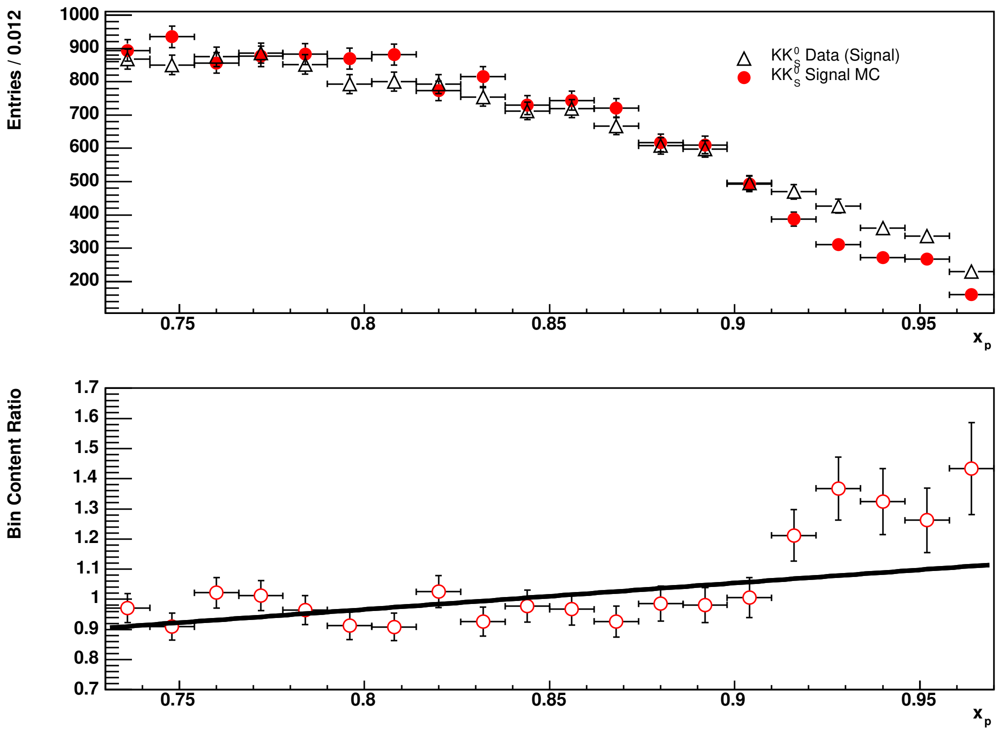


**Figure** 4.11: A comparison of $x_p$ distributions for $D_s^\pm \to K^\pm K_S^0$ signal MC events (circular points) and background subtracted data events (triangular points) is shown in the upper plot. The signal data events are isolated using a simple linear background subtraction technique. The ratio of the distributions is shown in the lower plot, including a linear fit (solid line) to the data points.

the result in figure 4.11. A linear fit to the ratio of the resultant histograms yields the parameters $a$ and $b$ with associated errors.

The integrals appearing in equation 4.21 are evaluated by simply counting the events appearing in the relevant $x_p$ distribution. The integrals appearing as numerators are evaluated by summing, over all bins, the product of the bin content and the bin's central $x_p$ value.

The associated systematic is introduced via the error on the determined correction factor, $f$. Letting $x$ and $y$ represent the integral ratios appearing in equation 4.21 gives the upper and lower limits on $R'_{D_s^\pm \to X^\pm Y}$ as

$$R'^{\pm}_{D_s^{\pm}\to X^{\pm}Y} = R_{D_s^{\pm}\to X^{\pm}Y} \cdot \left[1 + \left(\frac{b}{a} \pm \sigma_{\frac{b}{a}}\right) x - \left(\frac{b}{a} \pm \sigma_{\frac{b}{a}}\right) y\right] \tag{4.22}$$

where $\sigma_{\frac{b}{a}}$ is the error associated with the quantity $\frac{b}{a}$. The fractional change of $R'_{D_s^{\pm}\to X^{\pm}Y}$ is then determined by calculating

$$\begin{aligned} \Delta R'_{D_s^{\pm}\to X^{\pm}Y} &= \frac{R'^{\pm}_{D_s^{\pm}\to X^{\pm}Y} - R'_{D_s^{\pm}\to X^{\pm}Y}}{R'_{D_s^{\pm}\to X^{\pm}Y}} \\ &= \frac{\pm\sigma_{\frac{b}{a}}\, x \mp \sigma_{\frac{b}{a}}\, y}{1 + \frac{b}{a}\, x - \frac{b}{a}\, y} \end{aligned} \tag{4.23}$$

Taking the modulus of the numerator and calculating $\Delta R'_{D_s^{\pm}\to X^{\pm}Y}$ yields the systematic error associated with the efficiency ratio calculation. The percentage errors on the signal yields are calculated as 0.87%, 0.92% and 0.15% for the $D_s^{\pm} \to K^{\pm}\pi^0$, $D_s^{\pm} \to \pi^{\pm}\pi^0$ and $D_s^{\pm} \to \pi^{\pm}K_S^0$ modes respectively.

### 4.7.3 Particle Identification

Corrections are made to the MC samples such that particle identification efficiencies more closely match data. The process is known as PID killing and is described elsewhere [92]. A systematic error for particle identification efficiency is then taken from a prior analysis that assigns a conservative estimate based on a detailed study [93] involving a high statistics data sample of $D^0$ candidates decaying to $K\pi$, $K\pi\pi^0$ and $K\pi\pi\pi$ final states. A value of 0.5% is assigned per pion or kaon identification. Since branching fraction ratios are calculated, in the case of the $D_s^{\pm} \to K^{\pm}\pi^0$ mode this systematic cancels with itself and does not apply. However, this error does apply to the $D_s^{\pm} \to \pi^{\pm}\pi^0$ and $D_s^{\pm} \to \pi^{\pm}K_S^0$ modes. The cause of the error also determines whether or not it will apply. If it is due to the solid angle coverage of the DCH and DIRC being incorrectly known then the errors for each particle identification are correlated and hence cancel each other out. If it is due purely to the statistics of the samples used to evaluate the 0.5% then the errors for each identification are uncorrelated and must be summed in quadrature. The cause is unknown, therefore the errors are treated as uncorrelated and the systematic is conservatively found to be 0.71% for the modes to which it applies.

### 4.7.4 Charged Track Efficiencies

The standard systematic error on the track reconstruction efficiency per single track at *BABAR* is 0.8% as determined from a thorough study conducted by the *BABAR* Tracking Working Group [94]. Charged track efficiencies are evaluated by looking at detected tracks from multi-hadron events in the SVT and counting how often a matching track is identified in the DCH and vice versa. This is followed by a direct data and MC sample comparison. The systematic for $K_S^0$ particles in the final state, where the composite candidate decays to two tracks, is computed by combining the errors for the individual tracks. Where the signal modes contain a single charged track and a $\pi^0$, this systematic error is entirely due to the error associated with the reconstructed $K_S^0$ candidate in the $D_s^\pm \to K^\pm K_S^0$ mode. For the $D_s^\pm \to \pi^\pm K_S^0$ mode all tracking systematics cancel in the branching ratio calculation.

### 4.7.5 Neutral Cluster Efficiencies

Studies have been conducted at *BABAR* on photon detection efficiencies resulting in standard errors that are applied [95]. The study involves a comparison between data and a large statistics MC sample of $\tau$ decays to final states containing neutral pions to determine detection efficiencies for neutral particles in the EMC. A 3.0% systematic is assigned per $\pi^0$, combined with a further 1.8% per photon not originating from a $\pi^0$. The efficiency correction for single photons is valid up to an energy of 2 GeV in the laboratory frame. This gives a systematic error of 3% for the decay modes $D_s^\pm \to K^\pm \pi^0$ and $D_s^\pm \to \pi^\pm \pi^0$. However, since all modes contain a single photon from a radiative $D_s^*$ decay, the systematic error cancels in the branching ratio calculation. There is therefore no error associated with the $D_s^\pm \to \pi^\pm K_S^0$ mode.

**Table** 4.6: List of systematic error sources and their values for each reconstruction mode where relevant. Values are tabulated as percentages for the purposes of combining the errors from different sources with the denominator in each calculation being the signal yield from the relevant fit to data. In the case of $D_s^\pm \to \pi^\pm\pi^0$, where the fit yield is negative, the absolute value of the yield is used.

| | Mode Specific Systematic Errors / % | | | |
|---|---|---|---|---|
| | $D_s^\pm \to K^\pm\pi^0$ | $D_s^\pm \to \pi^\pm\pi^0$ | $D_s^\pm \to K^\pm K_S^0$ | $D_s^\pm \to \pi^\pm K_S^0$ |
| Errors Affecting Signal Yield | | | | |
| BABAR Mass Scale | 1.22 | 0.86 | - | 1.18 |
| BABAR Resolution | 2.79 | 1.15 | - | 1.98 |
| MC Statistics | 2.77 | 18.1 | 1.34 | 2.57 |
| Background Modelling | 0.07 | 1.94 | 0.02 | 0.10 |
| Fake Signal Peaks | 0.39 | - | 0.28 | - |
| Errors Affecting Efficiency Ratios | | | | |
| MC Statistics | 0.03 | 0.03 | 0.03 | 0.03 |
| $x_p$ Spectrum | 0.87 | 0.92 | - | 0.15 |
| Particle ID | - | 0.71 | - | 0.71 |
| Tracking Efficiency | 1.13 | 1.13 | - | - |
| Neutrals Efficiency | 3.00 | 3.00 | - | - |
| Errors Above Combined | 5.30 | 18.6 | 1.37 | 3.53 |
| Errors Affecting Branching Fraction | | | | |
| $\mathcal{B}(D_s^+ \to K^+\overline{K}^0)$ | 20.8 | 20.8 | - | 20.8 |

## 4.8 Branching Ratio Calculation

The event yields quoted in this chapter are for the reconstructed $D_s$ decay channels $D_s^\pm \to K^\pm\pi^0$, $D_s^\pm \to \pi^\pm\pi^0$, $D_s^\pm \to \pi^\pm K_S^0$ and $D_s^\pm \to K^\pm K_S^0$. Using these yields the branching ratios relative to the $D_s^\pm \to K^\pm K_S^0$ reference mode can be calculated using the following equation:

$$\frac{\mathcal{B}(D_s^\pm \to X^\pm Y)}{\mathcal{B}(D_s^\pm \to K^\pm K_S^0)} = \frac{N(D_s^\pm \to X^\pm Y)}{N(D_s^\pm \to K^\pm K_S^0)} \cdot \frac{\epsilon(D_s^\pm \to K^\pm K_S^0)}{\epsilon(D_s^\pm \to X^\pm Y)} \cdot f_{\epsilon(D_s^\pm \to X^\pm Y)} \tag{4.24}$$

where $\mathcal{B}$ and $\epsilon$ are the branching fraction and reconstruction efficiency of the process within the brackets, respectively, $D_s^\pm \to X^\pm Y$ represents any reconstructed signal mode, and $f_{\epsilon(D_s^\pm \to X^\pm Y)}$ represents the efficiency ratio correction determined in section 4.7.2.

The signal MC efficiencies listed in table 3.8 represent the reconstruction efficiency for truth and SCF events combined, and therefore have to be altered. The efficiencies are corrected by using the fraction of events in the signal MC sample that are described by the truth PDF (table 3.6). The corrected efficiencies that are used in the branching ratio calculations are:

$$\begin{aligned}
\epsilon(D_s^\pm \to K^\pm \pi^0) &= (3.88 \pm 0.03)\% \\
\epsilon(D_s^\pm \to \pi^\pm \pi^0) &= (4.69 \pm 0.03)\% \\
\epsilon(D_s^\pm \to K^\pm K_S^0) &= (3.17 \pm 0.03)\% \\
\epsilon(D_s^\pm \to \pi^\pm K_S^0) &= (3.84 \pm 0.03)\%
\end{aligned}$$

Despite the slight drop in efficiency here the error does not change significantly, therefore the systematic errors introduced in section 4.7.1 still apply.

Several factors now have to be taken into account in order to calculate the ratios for $D_s^+ \to K^+\pi^0$, $D_s^+ \to \pi^+\pi^0$ and $D_s^+ \to \pi^+K^0$ with respect to $D_s^+ \to K^+\overline{K}^0$, where charge conjugation is now implied in all cases. Because $K^0$ and $\pi^0$ candidates are only reconstructed from $\pi^+\pi^-$ and $\gamma\gamma$ final states respectively, and $K_L^0$ mesons are ignored completely, the factors to be included in principle are:

- $\mathcal{B}(K^0 \to K_S^0)$,
- $\mathcal{B}(K_S^0 \to \pi^+\pi^-)$, and
- $\mathcal{B}(\pi^0 \to \gamma\gamma)$.

However, the signal MC events (table 3.2) generated for this analysis did not force the decays of $K_S^0$ and $\pi^0$ mesons through the reconstruction channels during the production. Therefore the signal reconstruction efficiencies have been calculated with the effects of $\mathcal{B}(K_S^0 \to \pi^+\pi^-)$ and $\mathcal{B}(\pi^0 \to \gamma\gamma)$ already taken into account. As a result, it only remains to account for $\mathcal{B}(K^0 \to K^0_S)$ which is a forced decay during the production of $D^\pm_s \to K^\pm K^0_S$ and $D^\pm_s \to \pi^\pm K^0_S$ signal MC data.

The neutral kaon system comprises 50% $K^0_S$ and 50% $K^0_L$. The branching ratio with respect to $D^+_s \to K^+\overline{K}^0$ is calculated by simply multiplying the measured branching ratio by a factor of 2. Moreover, this correction does not apply for the $D^+_s \to \pi^+K^0$ ratio since the effect cancels out in the ratio calculation.

Using equation 4.24 and applying the above correction (where applicable), the branching ratios for the three signal modes with respect to the reference mode are calculated:

$$\frac{\mathcal{B}(D^+_s \to K^+\pi^0)}{\mathcal{B}(D^+_s \to K^+\overline{K}^0)} = (2.54 \pm 0.20 \pm 0.14) \times 10^{-2}$$

$$\frac{\mathcal{B}(D^+_s \to \pi^+K^0)}{\mathcal{B}(D^+_s \to K^+\overline{K}^0)} = (8.28 \pm 0.38 \pm 0.32) \times 10^{-2}$$

$$\frac{\mathcal{B}(D^+_s \to \pi^+\pi^0)}{\mathcal{B}(D^+_s \to K^+\overline{K}^0)} = (-0.25 \pm 0.24 \pm 0.05) \times 10^{-2}$$

where the first and second errors in each case are statistical and systematic respectively.

### 4.8.1 Ratio Limit Calculation

The result of the signal yield limit for the $D^\pm_s \to \pi^\pm\pi^0$ fit to data is now modified to take into account the systematic error affecting the branching ratio with respect to $D^+_s \to K^+\overline{K}^0$. This results in the likelihood curve being shifted further and hence a larger upper limit on branching ratio than would otherwise be calculated. The modified upper limit on the yield is 164 and can be combined with the calculations described above to translate it into a branching ratio upper limit of

$$\frac{\mathcal{B}(D_s^+ \to \pi^+\pi^0)}{\mathcal{B}(D_s^+ \to K^+\overline{K}^0)} < 3.83 \times 10^{-3} \qquad \text{CL} = 90\%. \tag{4.25}$$

## 4.9 Branching Fraction Systematic Error

The branching fractions for $D_s^+ \to K^+\pi^0$, $D_s^+ \to \pi^+\pi^0$ and $D_s^+ \to \pi^+K^0$ are calculated with respect to the reference mode $D_s^+ \to K^+\overline{K}^0$. Using the value for $\mathcal{B}(D_s^+ \to K^+\overline{K}^0)$ quoted in equation 1.30, the experimental error associated with the reference mode is calculated to be $\sim 21\%$. This is the largest systematic error in the analysis.

## 4.10 Branching Fraction Calculation

Using the results quoted in section 4.8 in conjunction with $\mathcal{B}(D_s^+ \to K^+\overline{K}^0)$ (equation 1.30) the absolute branching fractions for the three signal modes are calculated:

$$\mathcal{B}(D_s^+ \to K^+\pi^0) = (1.12 \pm 0.09 \pm 0.24) \times 10^{-3}$$

$$\mathcal{B}(D_s^+ \to \pi^+K^0) = (3.64 \pm 0.17 \pm 0.76) \times 10^{-3}$$

$$\mathcal{B}(D_s^+ \to \pi^+\pi^0) = (-0.11 \pm 0.11 \pm 0.03) \times 10^{-3}$$

where the first and second errors quoted are statistical and systematic respectively. For the case of $D_s^+ \to \pi^+\pi^0$, the upper allowed limit on the branching fraction is calculated by broadening the $D_s^+ \to \pi^+\pi^0$ likelihood curve further still using the systematic error introduced by the uncertainty on $\mathcal{B}(D_s^+ \to K^+\overline{K}^0)$. This results in the upper limit on the yield increasing to 167 and leads to an upper limit on $\mathcal{B}(D_s^+ \to \pi^+\pi^0)$ of

$$\mathcal{B}(D_s^+ \to \pi^+\pi^0) < 1.72 \times 10^{-4} \qquad \mathrm{CL} = 90\%. \tag{4.26}$$

## 4.11 Charge Asymmetry Measurement

Although $CP$ asymmetries are expected to be small (section 1.4.1) the data are refitted to determine an asymmetry measurement and to serve as a cross-check that the maximum likelihood analysis is consistent. To achieve this, the data samples are split into two subsamples according to the electric charge of the $D_s$ meson. This is done for all modes where a significant signal yield is observed, i.e. $D_s^+ \to K^+\pi^0$, $D_s^+ \to K^+\overline{K}^0$ and $D_s^+ \to \pi^+K^0$. The yields returned by the fit for the positively charged samples are

$$\begin{aligned} N(D_s^+ \to K^+\pi^0) &= 425 \pm 48 \\ N(D_s^+ \to K^+K_S^0) &= 7297 \pm 119 \\ N(D_s^+ \to \pi^+K_S^0) &= 677 \pm 45 \end{aligned}$$

and the corresponding yields for the negatively charged samples are

$$\begin{aligned} N(D_s^- \to K^-\pi^0) &= 478 \pm 50 \\ N(D_s^- \to K^-K_S^0) &= 6977 \pm 119 \\ N(D_s^- \to \pi^-K_S^0) &= 760 \pm 45. \end{aligned}$$

The separate yields for each decay mode are now combined to check that they agree with the yields presented in section 4.6. The sums of the positive and negative yields for each decay mode are

$$\begin{aligned}N_{CP}(D_s^\pm \to K^\pm\pi^0) &= 903 \pm 69\\ N_{CP}(D_s^\pm \to K^\pm K_S^0) &= 14274 \pm 168\\ N_{CP}(D_s^\pm \to \pi^\pm K_S^0) &= 1437 \pm 64\end{aligned}$$

where $N_{CP}$ implies the yield has been calculated from charge asymmetry measurements to differentiate it from a yield quoted in section 4.6. Comparing these values with those appearing in section 4.6 shows that they are consistent with one another. This is a further indication that the likelihood fit is performing as it should.

The asymmetry, $A_{CP}$, of the different charged samples is defined as

$$A_{CP} = \frac{\mathcal{A}_+ - \mathcal{A}_-}{\mathcal{A}_+ + \mathcal{A}_-} \tag{4.27}$$

where the process amplitudes $\mathcal{A}_\pm \propto N(D_s^\pm \to X^\pm Y)$, where $D_s^\pm \to X^\pm Y$ is any relevant decay mode. Therefore the charge asymmetry in the decay modes can be determined from the following equation:

$$A_{CP}(D_s^\pm \to X^\pm Y) = \frac{N_{CP}(D_s^+ \to X^+Y) - N_{CP}(D_s^- \to X^-Y)}{N_{CP}(D_s^+ \to X^+Y) + N_{CP}(D_s^- \to X^-Y)}. \tag{4.28}$$

The charge asymmetry measurements for each mode where a significant signal is observed are

$$\begin{aligned}A_{CP}(D_s^\pm \to K^\pm\pi^0) &= -0.059 \pm 0.077\\ A_{CP}(D_s^\pm \to K^\pm K_S^0) &= 0.022 \pm 0.012\\ A_{CP}(D_s^\pm \to \pi^\pm K_S^0) &= -0.058 \pm 0.044\end{aligned}$$

where no measurement yields a significant charge asymmetry.

# Chapter 5

# Conclusions

## 5.1 Overview

In this final chapter the results of the maximum likelihood analysis are discussed. It begins with a brief summary of the analysis results. Following this is a comparison between the significant results presented in this thesis and the current experimental status of these processes as listed by the Particle Data Group [17] (PDG). Comparisons are also drawn between topologically similar $D^+$ and $D^0$ decays as a quantitative test of the quark spectator model. It is also important to test the results against current theoretical predictions to either rule out or support the theoretical models on which the predictions are based. Finally, some comments are made on the future of charm physics with regard to the subject of this thesis and how new measurements will contribute to the improved accuracy of the results presented here.

## 5.2 Results Summary

To summarise, two statistically significant first observations are reported in this thesis for the processes $D_s^+ \to K^+\pi^0$ and $D_s^+ \to \pi^+K^0$. The branching fractions of these processes are found to be $\mathcal{B}(D_s^+ \to K^+\pi^0) = (1.12 \pm 0.09 \pm 0.24) \times 10^{-3}$

and $\mathcal{B}(D_s^+ \to \pi^+ K^0) = (3.64 \pm 0.17 \pm 0.76) \times 10^{-3}$ where the first and second errors quoted are statistical and systematic respectively. No evidence is found for the process $D_s^+ \to \pi^+\pi^0$. An upper limit on the branching fraction, with 90% confidence, is calculated to be $\mathcal{B}(D_s^+ \to \pi^+\pi^0) < 1.72 \times 10^{-4}$ with a sensitivity of $1.41 \times 10^{-4}$.

## 5.3 Comparison with Experimental Data

### 5.3.1 Branching Fractions

To the best of the author's knowledge, there is currently no experimental data for $\mathcal{B}(D_s^\pm \to K^\pm\pi^0)$ and $\mathcal{B}(D_s^\pm \to \pi^\pm\pi^0)$ in the literature and so comparisons with prior measurements cannot be drawn. The PDG lists a branching fraction limit for the decay $D_s^+ \to \pi^+ K^0$ of

$$\mathcal{B}(D_s^+ \to \pi^+ K^0) < 8 \times 10^{-3} \qquad \mathrm{CL} = 90\%. \tag{5.1}$$

This is compatible with the corresponding experimental result presented in section 4.10. It is further evidence that the analysis is returning sensible results.

### 5.3.2 Quark Spectator Model

Decays of mesons, charmed or otherwise, are often described in terms of the spectator model. It is an approximation stating that the lightest of the meson's constituent quarks plays no part in its decay. For example, the decays $D_s^+ \to K^+\pi^0$ and $D_s^+ \to \pi^+ K^0$ (figures 1.3(a) and 1.3(c)) involve the weak decay of the charm quark while the $\overline{s}$ quark merely spectates before hadronising with another quark in the final state.

The applicability of the spectator model to charmed mesons can be tested by comparing processes with Feynman diagrams that differ only by the flavour of the spectator quark. Replacing the $\overline{s}$ quark in figures 1.3(a) and 1.3(c) with a $\overline{d}$ or $\overline{u}$ changes the $D_s^+$ into a $D^+$ or $D^0$ respectively and changes one of the mesons in the final state. Therefore, in the spectator model the equivalent decays for $D_s^+ \to K^+\pi^0$ are $D^+ \to \pi^+\pi^0$ and $D^0 \to \pi^0\pi^0$. Similarly, the equivalent decays for $D_s^+ \to \pi^+K^0$ are $D^+ \to \pi^+\pi^0$ and $D^0 \to \pi^+\pi^-$. The $D^+$ final state is the same in each case because it has both an internal and external $W$-emission diagram which presents problems when making direct comparisons with this decay mode.

Partial decay widths for the processes listed above can now be compared. Comparison of the partial widths (and not the branching fractions) is required because the lifetimes, $\tau$, of the $D_s^+$, $D^+$ and $D^0$ are all different. Using $\Gamma_i = \mathcal{B}_i\Gamma$, where $\Gamma$ is the full width, $\Gamma_i$ is the partial width, $\mathcal{B}_i$ is the branching fraction and $i$ denotes a particular process, and taking the full width as $1/\tau$, then the partial width ratios, $R_{ij}$, can be calculated using

$$R_{ij} = \frac{\Gamma_i}{\Gamma_j} = \frac{\mathcal{B}_i}{\tau_i} \cdot \frac{\tau_j}{\mathcal{B}_j} \tag{5.2}$$

where $\tau_{i(j)}$ denotes the lifetime of the charmed meson in process $i(j)$. If the spectator model holds then the partial width ratios should be compatible with unity. Using the branching fractions presented in section 4.10 for the statistically significant measurements, the partial width ratios are calculated:

$$\frac{\Gamma_{D_s^+ \to K^+\pi^0}}{\Gamma_{D^+ \to \pi^+\pi^0}} = 1.79 \pm 0.51$$
$$\frac{\Gamma_{D_s^+ \to K^+\pi^0}}{\Gamma_{D^0 \to \pi^0\pi^0}} = 1.69 \pm 0.59$$
$$\frac{\Gamma_{D_s^+ \to \pi^+K^0}}{\Gamma_{D^+ \to \pi^+\pi^0}} = 2.90 \pm 0.79$$
$$\frac{\Gamma_{D_s^+ \to \pi^+K^0}}{\Gamma_{D^0 \to \pi^+\pi^-}} = 3.63 \pm 1.23$$

**Table** 5.1: Summary of theoretical predictions and the experimental results presented in this thesis for the branching fractions of the signal decay modes of interest.

| Source | Branching Fractions / % | | |
|---|---|---|---|
| | $\mathcal{B}(D_s^+ \to K^+\pi^0)$ | $\mathcal{B}(D_s^+ \to \pi^+K^0)$ | $\mathcal{B}(D_s^+ \to \pi^+\pi^0)$ |
| Chau and Cheng [23] | - | - | 0 |
| Bucella *et al.* [25] | 0.16 | 0.43 | - |
| Lusignoli and Pugliese [28] | 0.146 | 0.373 | - |
| Experimental Result | $0.112 \pm 0.026$ | $0.364 \pm 0.078$ | $< 0.017$ |

These results imply the spectator model to be applicable to a factor of 2 or 3 in all cases. It is known that the spectator model is not completely accurate for describing the decays of charmed mesons. The spectator model is expected to be accurate to roughly an order of magnitude, therefore the partial width ratios measured here are within expectations.

## 5.4 Comparison with Theoretical Predictions

Comparison of experimental data with theoretical predictions is important in that theories need to be verified with experiment. The measurements presented in this thesis can be compared with the predictions listed in table 5.1.

Comparison of the statistically significant absolute branching fraction measurements presented in section 4.10 and the theoretical predictions mentioned above shows the numbers to be compatible. For $\mathcal{B}(D_s^\pm \to K^\pm\pi^0)$ the experimental and theoretical values differ by less than two standard deviations, while for $\mathcal{B}(D_s^+ \to \pi^+K^0)$ the values are within one standard deviation. Therefore, the theoretical models used to determine the estimates cannot be discounted. Although there is no prediction for $\mathcal{B}(D_s^+ \to \pi^+\pi^0)$, the zero contribution from the quark level diagrams in the scheme of Chau and Cheng [23] was used to infer a value of zero for the branching fraction. The limit presented in section 4.10 for $\mathcal{B}(D_s^+ \to \pi^+\pi^0)$ is consistent with this inferred value.

A comparison can also be drawn for the branching ratio $\mathcal{B}(D_s^+ \to \pi^+K^0)/\mathcal{B}(D_s^+ \to K^+\pi^0)$ which is independent of the reference mode. Using the relevant yields and ratios, together with the applicable systematics in table 4.6, the branching ratio is calculated to be

$$\frac{\mathcal{B}(D_s^+ \to \pi^+ K^0)}{\mathcal{B}(D_s^+ \to K^+ \pi^0)} = 3.23 \pm 0.28 \pm 0.21 \tag{5.3}$$

where the first and second errors quoted are statistical and systematic respectively. This result is within two standard deviations of the average ratio of 2.63 computed from the predictions listed in table 5.1.

## 5.5 Future Measurements

The absolute branching fractions presented here have systematic errors that are dominated by the existing error on $\mathcal{B}(D_s^+ \to K^+ \overline{K}^0)$, while the branching ratios measured with respect to this mode are known to a greater degree of accuracy. This is unavoidable due to insufficient available information with which to calculate the original number of $D_s$ or $D_s^*$ mesons produced by the $e^+e^-$ annihilations of the PEP-II machine. However, the CLEO [58] collaboration plan to investigate $e^+e^-$ annihilations at the $D_s^+ \, D_s^-$ production threshold in the near future [96] which will greatly improve the measurement of $\mathcal{B}(D_s^+ \to K^+ \overline{K}^0)$ and other $D_s$ decay modes. The statistics of the *BABAR* experiment will still be far superior to that of the CLEO experiment, hence the measurements of singly Cabibbo and doubly Cabibbo suppressed $D_s$ decay modes at *BABAR* will complement the precision measurements of Cabbibo allowed $D_s$ processes by the CLEO collaboration for the foreseeable future.

# References

[1] F. Halzen and A. D. Martin, New York, Usa: Wiley (1984) 396p.

[2] I. J. R. Aitchison and A. J. G. Hey, Bristol, UK: IOP (2003) 406p.

[3] C.-N. Yang and R. L. Mills, Phys. Rev. **96**, 191 (1954).

[4] S. L. Glashow, Nucl. Phys. **22**, 579 (1961).

[5] S. Weinberg, Phys. Rev. Lett. **19**, 1264 (1967).

[6] A. Salam and J. C. Ward, Phys. Rev. **B136**, 763 (1964).

[7] P. W. Higgs, Phys. Lett. **12**, 132 (1964).

[8] G. 't Hooft, Nucl. Phys. **B33**, 173 (1971).

[9] SNO, Q. R. Ahmad *et al.*, Phys. Rev. Lett. **89**, 011301 (2002).

[10] Super-Kamiokande, Y. Fukuda *et al.*, Phys. Rev. Lett. **81**, 1562 (1998).

[11] N. Cabibbo, Phys. Rev. Lett. **10**, 531 (1963).

[12] S. L. Glashow, J. Iliopoulos, and L. Maiani, Phys. Rev. **D2**, 1285 (1970).

[13] E598, J. J. Aubert *et al.*, Phys. Rev. Lett. **33**, 1404 (1974).

[14] SLAC-SP-017, J. E. Augustin *et al.*, Phys. Rev. Lett. **33**, 1406 (1974).

[15] G. Goldhaber *et al.*, Phys. Rev. Lett. **37**, 255 (1976).

[16] L.-L. Chau, Phys. Rept. **95**, 1 (1983).

[17] Particle Data Group, S. Eidelman *et al.*, Phys. Lett. **B592**, 1 (2004).

[18] M. Gorn, Nucl. Phys. **B191**, 269 (1981).

[19] P. F. Bedaque, A. K. Das, and V. S. Mathur, Phys. Rev. **D49**, 1339 (1994).

[20] K. G. Wilson, Phys. Rev. **179**, 1499 (1969).

[21] M. Bauer, B. Stech, and M. Wirbel, Z. Phys. **C34**, 103 (1987).

[22] e. Buras, A. J. and e. Lindner, M., Singapore, Singapore: World Scientific (1992) 785p. (Advanced series on directions in high energy physics, 10).

[23] L.-L. Chau and H.-Y. Cheng, Phys. Rev. **D36**, 137 (1987).

[24] L.-L. Chau and H.-Y. Cheng, Phys. Lett. **B333**, 514 (1994).

[25] F. Buccella, M. Lusignoli, G. Miele, A. Pugliese, and P. Santorelli, Phys. Rev. **D51**, 3478 (1995).

[26] F. Buccella, M. Lusignoli, and A. Pugliese, Phys. Lett. **B379**, 249 (1996).

[27] M. Neubert, Phys. Rept. **245**, 259 (1994).

[28] M. Lusignoli and A. Pugliese, (2002), hep-ph/0210071.

[29] F. E. Close and H. J. Lipkin, Phys. Lett. **B551**, 337 (2003).

[30] B. Bajc, S. Fajfer, R. J. Oakes, and S. Prelovsek, (1997), hep-ph/9708277.

[31] CLEO, R. A. Briere *et al.*, Phys. Rev. **D62**, 072003 (2000).

[32] *BABAR*, B. Aubert *et al.*, Phys. Rev. **D71**, 091104 (2005).

[33] *BABAR*, B. Aubert *et al.*, Nucl. Instrum. Meth. **A479**, 1 (2002).

[34] PEP-II: An Asymmetric B Factory. Conceptual Design Report. SLAC-R-418.

[35] *BABAR*, e. Harrison, P. F. and e. Quinn, Helen R., The *BABAR* physics book: Physics at an asymmetric B factory.

[36] *BABAR*, D. Boutigny *et al.*, Letter of intent for the study of CP violation and heavy flavor physics at PEP-II, SLAC-0443.

[37] E. Bloom *et al.*, Presented at 4th European Particle Accelerator Conference (EPAC 94), London, England, 27 Jun - 1 Jul 1994.

[38] J. Seeman *et al.*, Presented at 9th European Particle Accelerator Conference (EPAC 2004), Lucerne, Switzerland, 5-9 Jul 2004.

[39] M. Sullivan, Talk given at 17th IEEE Particle Accelerator Conference (PAC 97): Accelerator Science, Technology and Applications, Vancouver, Canada, 12-16 May 1997.

[40] Y. Nosochkov, Y. Cai, J. Irwin, M. Sullivan, and E. Forest, Presented at 16th IEEE Particle Accelerator Conference (PAC 95) and International Conference on High Energy Accelerators, Dallas, Texas, 1-5 May 1995.

[41] W. Kozanecki *et al.*, Presented at the 9th European Particle Accelerator Conference (EPAC 2004), Lucerne, Switzerland, 5-9 Jul 2004.

[42] T. Mattison *et al.*, To appear in the proceedings of IEEE Particle Accelerator Conference (PAC 99), New York, New York, 29 Mar - 2 Apr 1999.

[43] W. Kozanecki, Nucl. Instrum. Meth. **A446**, 59 (2000).

[44] *BABAR*, D. Boutigny *et al.*, *BABAR* technical design report, SLAC-R-0457.

[45] D. Barbieri *et al.*, Nuovo Cim. **A112**, 113 (1999).

[46] V. Re *et al.*, Nucl. Instrum. Meth. **A409**, 354 (1998).

[47] J. Beringer *et al.*, (2000), *BABAR* Note 518.

[48] R. Claus *et al.*, Presented at 11th IEEE NPSS Real Time Conference (Santa Fe 99), Santa Fe, NM, 14-18 Jun 1999.

[49] A. Boucham *et al.*, Nucl. Instrum. Meth. **A409**, 46 (1998).

[50] G. Sciolla *et al.*, Nucl. Instrum. Meth. **A419**, 310 (1998).

[51] Luma Metall AB, Kalmar, Sweden.

[52] J. Albert *et al.*, IEEE Trans. Nucl. Sci. **46**, 2027 (1999).

[53] P. Coyle *et al.*, Nucl. Instrum. Meth. **A343**, 292 (1994).

[54] Spectrosil is a trademark of TSL Group PCL, Wallsend, Tyne on Wear, NE28 6DG, England; Sold in the USA by Quartz Products Co., Louisville, KY, USA.

[55] Electron Tubes Limited (formerly: Thorn EMI Electron Tubes), Ruislip, Middlesex, England.

[56] P. Bourgeois, M. Karolak, and G. Vasseur, Nucl. Instrum. Meth. **A442**, 105 (2000).

[57] M. Benkebil, R. Cizeron, S. Plaszczynski, M. H. Schune, and G. Wormser, Nucl. Instrum. Meth. **A442**, 364 (2000).

[58] T. Swarnicki, Performance of the CLEO-II CsI(Tl) Calorimeter, *Proceedings of Workshop on B Factories*, Stanford, CA, USA (1992).

[59] BELLE, A. Bondar, Nucl. Instrum. Meth. **A408**, 64 (1998).

[60] Fluorinert (polychlorotrifluoro-ethylene) is manufactured by 3M Corporation, St. Paul, MN, USA.

[61] S-2744-08 PIN diode by Hamamatsu Photonics, K. K., Hamamatsu City, Japan.

[62] G. M. Haller and D. R. Freytag, IEEE Trans. Nucl. Sci. **43**, 1610 (1996).

[63] P. Fabbricatore *et al.*, IEEE Trans. Magnetics **32**, 2210 (1996).

[64] E. Antokhin *et al.*, Nucl. Instrum. Meth. **A432**, 24 (1999).

[65] C. Newman-Holmes, E. E. Schmidt, and R. Yamada, Nucl. Instrum. Meth. **A274**, 443 (1989).

[66] R. Santonico and R. Cardarelli, Nucl. Instrum. Meth. **187**, 377 (1981).

[67] L. Lista, Object Oriented Reconstruction Software for the IFR Detector of *BABAR* Experiment, *Proceedings of the Conference on Computing in High Energy Physics*, Padova, Italy (2000).

[68] N. Cavallo *et al.*, Nucl. Instrum. Meth. **A409**, 297 (1998).

[69] N. Cavallo *et al.*, Nucl. Phys. Proc. Suppl. **61B**, 545 (1998).

[70] G. Crosetti *et al.* Data Acquisition System for the RPC Detector of the *BABAR* Experiment, *Proceedings of the International Workshop on Resistive Plate Chambers and Related Detectors*, Naples, Italy (1997).

[71] M. De Giorgi *et al.*, Nucl. Instrum. Meth. **A378**, 472 (1996).

[72] ALEPH, D. Decamp *et al.*, Nucl. Instrum. Meth. **A294**, 121 (1990).

[73] CLEO, D. Andrews *et al.*, Nucl. Instrum. Meth. **211**, 47 (1983).

[74] SLD Design Report SLAC-R-273 (1994).

[75] L. R. Dalesio *et al.*, Nucl. Instrum. Meth. **A352**, 179 (1994).

[76] High Performance Storage System (HPSS), International Business Machines, Inc., Armonk, NY, USA.

[77] GEANT4, S. Agostinelli *et al.*, Nucl. Instrum. Meth. **A506**, 250 (2003).

[78] W. D. Hulsbergen, Nucl. Instrum. Meth. **A552**, 566 (2005).

[79] A. Drescher *et al.*, Nucl. Instrum. Meth. **A237**, 464 (1985).

[80] `http://www.slac.stanford.edu/BFROOT/www/Physics/Tools/Pid/Hadrons/Description_of_the_LH_selectors.html`.

[81] T. Colberg, (2001), *BABAR* Analysis Document 196.

[82] H. Band, J. Hollar, and A. Mohapatra, (2004), *BABAR* Analysis Document 474.

[83] J. D. Bjorken and S. J. Brodsky, Phys. Rev. **D1**, 1416 (1970).

[84] W. Verkerke and D. Kirkby, (2003), physics/0306116.

[85] R. Brun and F. Rademakers, Nucl. Instrum. Meth. **A389**, 81 (1997).

[86] F. James and M. Roos, Comput. Phys. Commun. **10**, 343 (1975).

[87] CLEO, K. Arms *et al.*, Phys. Rev. **D69**, 071102 (2004).

[88] K. S. Cranmer, Comput. Phys. Commun. **136**, 198 (2001).

[89] `http://www.slac.stanford.edu/BFROOT/www/Physics/Tools/Pid/Selectors/r16a/VeryTightLHKaonMicroSelection_details.html`.

[90] B. Aubert *et al.*, (2006), *BABAR* Analysis Document 1379.

[91] B. Aubert *et al.*, (2006), *BABAR* Analysis Document 1268.

[92] `http://www.slac.stanford.edu/BFROOT/www/Physics/Tools/Pid/PidOnMc/pidonmc.html`.

[93] C. Cheng, (2005), *BABAR* Analysis Document 824.

[94] T. Allmendinger *et al.*, (2004), *BABAR* Analysis Document 867.

[95] M. T. Allen, M. T. Naisbit, and A. Roodman, (2004), *BABAR* Analysis Document 870.

[96] T. E. Coan, AIP Conf. Proc. **698**, 461 (2004).